

論文 / 著書情報  
Article / Book Information

題目(和文)	X線マイクロトモグラフィーを用いた三次元多孔質の空隙スケールにおける化学的原油増進回収に関する研究
Title(English)	Pore-scale Study on Chemical Enhanced Oil Recovery in Three-dimensional Porous Media using X-ray Microtomography
著者(和文)	SHE Yun
Author(English)	Yun She
出典(和文)	学位:博士(工学), 学位授与機関:東京工業大学, 報告番号:甲第12184号, 授与年月日:2022年9月22日, 学位の種別:課程博士, 審査員:末包 哲也,花村 克悟,奥野 喜裕,伏信 一慶,齊藤 卓志
Citation(English)	Degree:Doctor (Engineering), Conferring organization: Tokyo Institute of Technology, Report number:甲第12184号, Conferred date:2022/9/22, Degree Type:Course doctor, Examiner:,,,,
学位種別(和文)	博士論文
Type(English)	Doctoral Thesis



Tokyo Institute of Technology

Doctoral Dissertation

**Pore-scale Study on Chemical Enhanced Oil Recovery in  
Three-dimensional Porous Media using X-ray Microtomography**

Author: Yun SHE

Supervisor: Prof. Tetsuya SUEKANE

Discipline: Mechanical Engineering

Date: July 2022



**Pore-scale Study on Chemical Enhanced Oil Recovery in  
Three-dimensional Porous Media using X-ray Microtomography**

A dissertation submitted to  
Tokyo Institute of Technology  
in partial fulfillment of the requirements  
for the degree of  
Doctor of Engineering

By

Yun SHE

Supervisor: Prof. Tetsuya SUEKANE

Mechanical Engineering

July 2022



## **Doctoral Dissertation Defense Committee**

### **Pore-scale Study on Chemical Enhanced Oil Recovery in Three-dimensional Porous Media using X-ray Microtomography**

Author: Yun SHE

Members of the Defense Committee:

Tokyo Institute of Technology: Tetsuya Suekane (Chief Examiner)

Tokyo Institute of Technology: Katsunori Hanamura (Examiner)

Tokyo Institute of Technology: Yoshihiro Okuno (Examiner)

Tokyo Institute of Technology: Kazuyoshi Fushinobu (Examiner)

Tokyo Institute of Technology: Takushi Saito (Examiner)

Time: 2022-07-06

Place: Zoom (online)



## ABSTRACT

In [Chapter 1](#), the research background and objective were stated. The current world energy is mainly supplied by the crude oils. However, the oil production from oil reservoirs is low and over 50% original oils in place are bypassed after the primary and secondary recovery stages. The oil bypassed mechanisms can attribute to two factors: viscous fingering (VF) and capillary forces. The chemical enhanced oil recovery (CEOR) methods are the most economical and effective techniques to improve the oil recovery because they could suppress the VF and reduce the capillary forces. It has been extensively reported that various CEOR methods were tried to optimize these two factors from a macro-scale application. Unfortunately, the pore-scale oil displacement mechanisms cannot be well understood since the rock reservoirs are opaque. In addition, the effect of acid compositions in crude oils was not systematically considered. Thanks to the advanced X-ray microtomography (micro-CT), we could have a deep insight into these micro-pore spaces from a three-dimensional (3D) visualization. Based on this imaging technique, our objective is to optimize various CEOR methods considering the effect of acid compositions in crude oils from a 3D pore-scale view.

In [Chapter 2](#), the performances and mechanisms of traditional surfactant and alkaline flooding were compared for acid-existing oil recovery. We found that the emulsification ability in alkaline flooding is much stronger than that in surfactant flooding, leading to a significant improvement of oil recovery. The effectiveness of surfactant transport to the water–oil interface is responsible for the performance differences. For surfactant flooding, the surfactant molecules are transported to the interface by convection individually, which is a time-dependent and slow process. By contrast, the alkaline flooding relies on the quick process of chemical-produced surfactant at the interface. In addition, the strong emulsification can, in turn, increase the chemical contact area and strengthen the convection flow, which again promotes the effective transport of surfactant molecules. To optimize the surfactant flooding, we introduced a novel cationic surfactant that could physically adsorb the acid components of oil to form a dual-surfactant system. Consequently, the surfactant transport to the interface became much quicker because of the fast accumulation of surfactant aggregates.

In [Chapter 3](#), the effect of acid concentrations on the performance of alkaline flooding was investigated. As suggested in the results, the oil recovery efficiency increases with increasing oil acid concentrations because of stronger emulsification ability. As the emulsification becomes stronger, the VF is gradually suppressed, and the oil displacement front becomes more stable. The complete emulsification occurs at the high-acid concentration at which the large oil clusters are completely emulsified into tiny-size oil droplets. As a result, an entrained flow happens because these tiny droplets could be entrained in the aqueous phase and easily pass through the pore spaces. Therefore, the strong emulsification has a good control over stable displacement and is characteristic of entrained flow. As an optimal scenario for



engineering, the alkaline flooding was suggested to be applied for the high-acid oil reservoirs. For these low-acid oil reservoirs, the emulsification is not strong enough, and capillary forces still dominate, which hinders the improvement of oil recovery. Hence, it is needed to consider a novel method that maintains the stable displacement control and eliminates the capillary forces at the same time.

In [Chapter 4](#), we created a novel solvent-based microemulsion flooding to improve the oil recovery regardless of the acid concentrations. The emulsion flooding was selected because of its good control for stable displacement. The solvent agent was used to prepare the emulsions due to its role of miscible behavior, which has an ability to eliminate the capillary forces. In addition, the solvent-based emulsion could reduce half percentage of solvent use, thereby significantly decreasing the cost. The performance of this new chemical agent was examined through the pore-scale detection using a micro-CT scanning. As shown in the results, the oil recovery was significantly improved regardless of the oil-acid concentrations. For one reason, the oil displacement by the emulsion flooding is uniform, namely VF is avoided, thereby leading to the increasing areal sweeping efficiency. For another reason, the solvent-based emulsion flooding exhibits a quasi-miscible displacement behavior. The either positive or negative capillary forces can be eliminated because the water–oil interface is not visible, but it presents a compositional gradient. Therefore, the oil recovery mechanism is controlled by the mass transfer that the solvent disperses into oils and oils are gradually dissolved into the solvent at the same time. The dissolved oil could entrain in the emulsion solution and flow out of the oil reservoirs. We concluded that the solvent-based microemulsion flooding has the best performance, which can be applied for any type of reservoirs regardless of oil acids and wettability (negative or positive capillary forces).

In [Chapter 5](#), the key conclusions of each chapter are summarized and some suggestions for future works are provided. The optimal CEOR methods should consider the acid concentrations and cost in an actual oil recovery application. For example, the solvent-based microemulsion flooding is more expensive than that of traditional surfactant and alkaline flooding. Considering the cost, the alkaline flooding is suggested to apply for a high-acid oil reservoir. For a low-acid oil reservoir, the novel cationic surfactant is recommended since it could adsorb the acid components to formulate a dual-surfactant system and work more effectively than an individual surfactant alone. For a non-acid oil reservoir, the solvent-based microemulsion flooding shows the best performance because of the capillary forces elimination. In an energy crisis, the oil production is a main concern instead of cost; the solvent-based microemulsion is highly recommended because it is independent on acid or wettability conditions, which could produce the oil recovery efficiency approaching 100%.

---

## Table of Contents

ABSTRACT.....	I
1 Introduction .....	1
1.1 Current energy situation .....	1
1.2 Oil recovery methods.....	2
1.3 Oil bypassed mechanism.....	4
1.3.1 Viscous fingering .....	5
1.3.2 Capillary forces.....	6
1.4 Chemical enhanced oil recovery .....	11
1.4.1 General mechanisms .....	11
1.4.2 Literature review .....	13
1.5 Miscible flooding .....	15
1.6 X-ray microtomography.....	16
1.7 Current research works .....	17
1.7.1 Problem statement.....	17
1.7.2 Thesis objective and outline.....	18
2 Comparative performance of ready-made and chemical-produced surfactants in acid-existing oil reservoirs.....	20
2.1 Experimental .....	20
2.1.1 Rock and fluids.....	20
2.1.2 Methodology .....	22
2.2 Results and discussion .....	26
2.2.1 Tube test and microscopic visualization .....	26
2.2.2 IFT and wettability measurement .....	27
2.2.3 Miniature core-flooding experiments .....	28
2.2.4 Underlying mechanism.....	36
2.3 Extra study for optimization .....	38

---

2.3.1 Chemicals and fluids .....	38
2.3.2 Experimental method .....	38
2.3.3 Image processing .....	40
2.3.4 Results and discussion.....	40
2.4 Summary.....	45
3 Effect of oil-acid concentration on performance of alkaline flooding application .....	47
3.1 Experimental section .....	47
3.1.1 Materials and fluids.....	47
3.1.2 Experiments and procedures.....	48
3.2 Results and discussion .....	51
3.2.1 Petri dish tests.....	51
3.2.2 Core-flooding tests (3D).....	53
3.2.3 Micromodel tests (2D) .....	57
3.2.4 Proposal for industrial applications .....	62
3.3 Summary.....	63
4 Solvent-based microemulsion flooding with quasi-miscible behavior regardless of oil-acid concentrations.....	64
4.1 Experimental .....	64
4.1.1 Materials .....	64
4.1.2 Test fluids.....	64
4.1.3 Sand-pack preparation.....	66
4.1.4 Experimental apparatus and procedure.....	68
4.1.5 Image processing workflow.....	69
4.2 Results and discussion .....	71
4.2.1 Emulsion characteristics .....	71
4.2.2 Wettability characterization .....	74
4.2.3 Displacement behavior and performance.....	75
4.3 Summary and suggestions.....	85

## Table of Contents

---

5 Conclusions and suggestions .....	87
5.1 Conclusions.....	87
5.2 Suggestions for future works.....	88
Appendix (supplementary material) .....	90
Appendix A.....	90
A.1 Image processing .....	90
A.2 Different flow rates in microchannel .....	92
Appendix B.....	93
Reference .....	97
Acknowledgements.....	110
Academic achievements .....	112



# 1 Introduction

## 1.1 Current energy situation

Fossil fuels (coal, crude oil and natural gas) are hydrocarbon-containing substances, which originates from decomposing plants and animals under complicated chemical and thermal processes for millions of years. A porous media formation called “reservoir” accumulates and traps these organic substances into its permeable layers [1]. The fossil fuels play a significant role in the global energy resources and economic activities [2]. As shown in Fig. 1-1, the fossil fuels account for about 80~90% of world total energy supply (TES) in 1971-2019 years [3,4]. Between 1971 and 2019 world TES increased from  $2.3 \times 10^{10}$  to  $6.1 \times 10^{10}$  J up to 2.6 times in a remarkable rise. Currently, the consumption peak of fossil fuels is decreased and clean energies, such as nuclear, hydrogen, biofuels, etc., are rapidly developed because the national pledge to reduce carbon dioxide (CO<sub>2</sub>) emissions [5,6]. However, the fact is that world economy is not ready to be supported by clean energy resources alone. Therefore, the fossil fuels continue to provide the majority of global energy demand for a foreseeable future [7–9]. Among fossil fuels, oil occupies the largest ratio for global energy resources, reaching 44.3% in 1971 and 30.9% in 2019, respectively (Fig. 1-1). As a conclusion, the oil remains the most important energy supply in the current century.

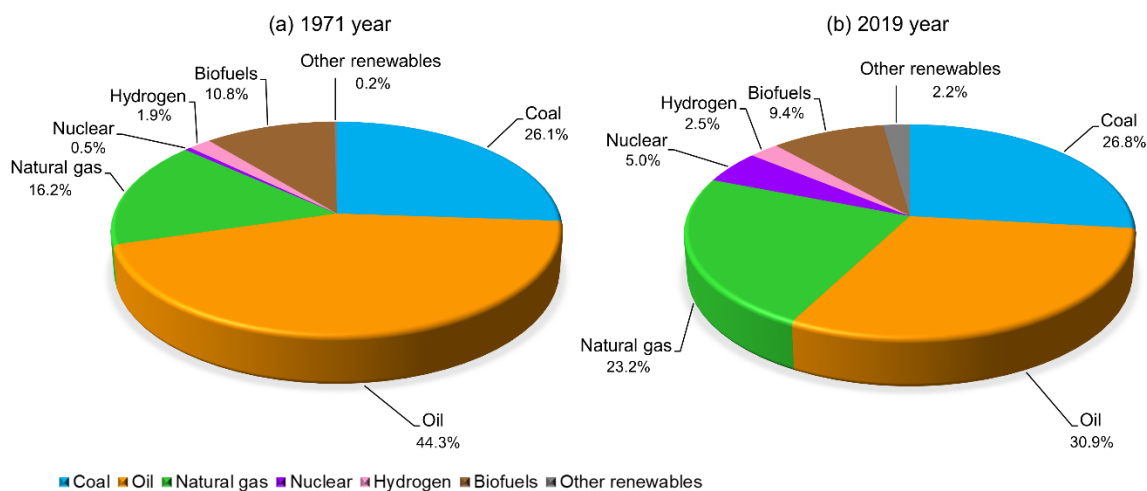


Fig. 1-1. World energy supply during 1971 year and 2019 year (Adapted from [4]).

The oils can be classified into two types of “conventional oil” and “unconventional oil” according to their API gravity and density or API and viscosity [10]. The general oil classification can be found in Table 1-1. For example, all oils with API gravity 20° and viscosity above 100 cP are considered to be conventional oil (light oils and medium oils), whilst the others are unconventional oil (heavy oils, extra-heavy oils and bitumen). According to the International Energy Agency (IEA), unconventional oils are categorized into light tight oil, shale oil and oil sands [7] because these oils exist in extremely low-permeability formations [11]. That means the unconventional oil production required

very difficult and different technologies from those used in the conventional oil reservoirs.

Table 1-1. Classification of oil types according to API and viscosity [10].

Oil type	API gravity (Degree API)	Dynamic viscosity (cP)
Light oils	$> 31.1^\circ$	$< 100$ cP
Medium oils	$22.3^\circ < \text{API} < 31.1^\circ$	$< 100$ cP
Heavy oils	$10.0^\circ < \text{API} < 22.3^\circ$	$> 100$ cP
Extra-heavy oils	$< 10^\circ$	$< 10000$ cP
Natural bitumen (or tar deposits)	$< 10^\circ$	$> 10000$ cP

Note: API gravity (American Petroleum Institute) is a measurement of density oil, within range of  $10^\circ \sim 70^\circ$ . The lower the number, the heavier and the more viscous the oil is.

Fig. 1-2 provide the world oil production from different types of sources. It can be seen that the world oil production and supply mainly come from the conventional oil (crude oil and natural gas liquids) because the traditional oil recovery techniques are mature and cost-effective. Although the unconventional oil resources are also very large (e.g., global shale oils are estimated at 4.8 trillion barrels), they are currently largely undeveloped owing to the immature technologies and high cost [7,12]. Therefore, how to make better use of conventional oil reservoirs is the most important as foresee.

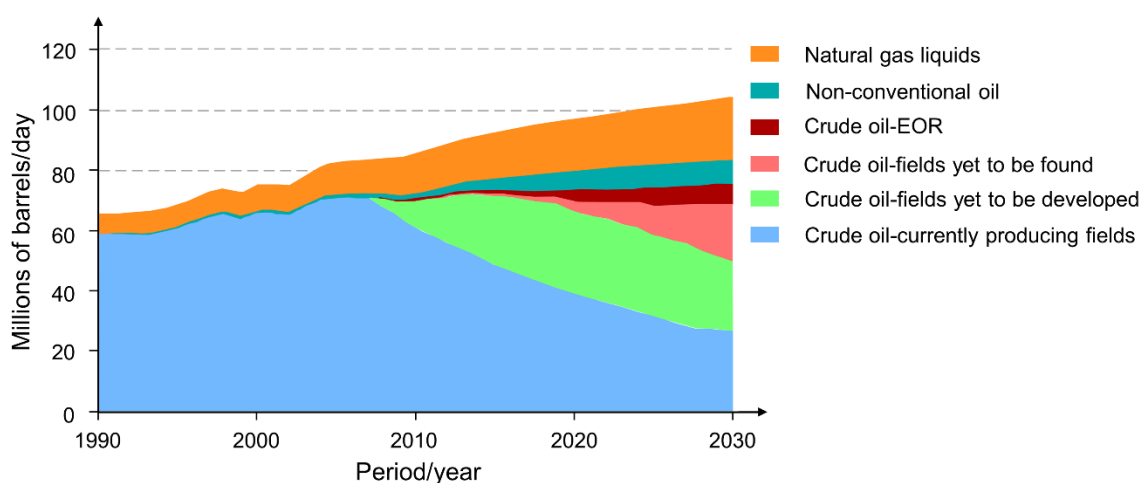


Fig. 1-2. World oil production supplied by different sources in millions of barrels per day [7,10]. EOR means enhanced oil recovery.

## 1.2 Oil recovery methods

The lifecycle of an oil reservoir experiences periods of discovery, exploration, production and abandonment (Fig. 1-3). In the production period, oils are produced from the reservoirs by three stages: primary recovery, secondary recovery and tertiary recovery [13]. As shown in Fig. 1-4, the primary recovery relies on the natural-driven mechanism by which oils are pushed out under the pressure gradient. Meanwhile, an artificial lift (pump-assisted) system is usually installed to increase the pressure difference. This stage usually produces oil recovery accounting for 10~25% original oil in place (OOIP) [13–15]. The secondary

recovery takes place until the primary presents profit limited. To be general, water or immiscible gas ( $\text{CO}_2$ ) is popularly used as a driven fluid to displace the oils out of reservoir. On this stage, additional oils of 15~25% OOIP are recovered [13–15]. After the primary and secondary stages, the new oilfields become mature oil fields, remaining over 50% OOIP unrecovered [16]. It is at the moment that third stage (tertiary recovery) plays a key role in the additional oil production from these mature oilfields.

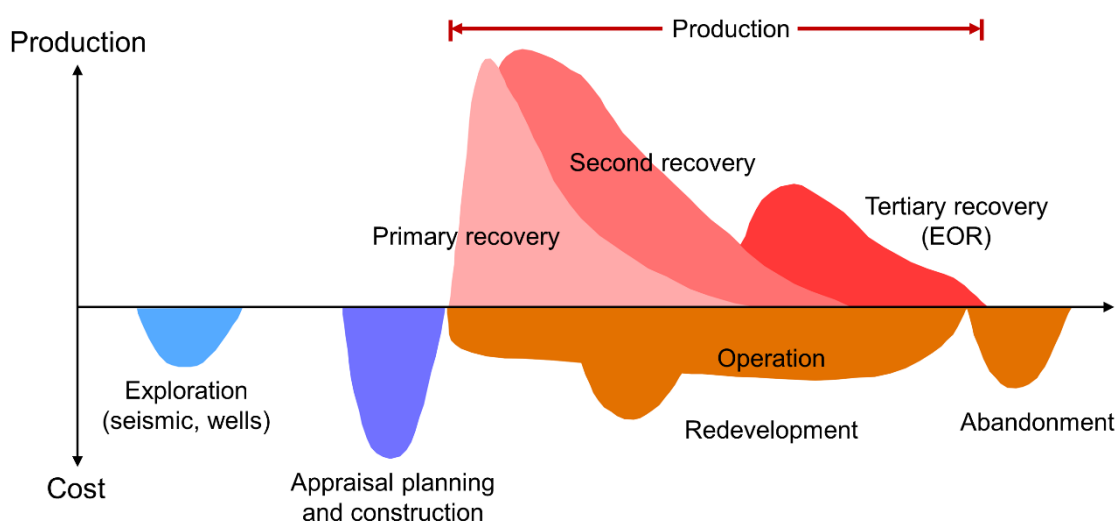


Fig. 1-3. Schematic representation of the lifecycle of an oil reservoir [7].

The tertiary oil recovery is also named enhanced oil recovery (EOR) which produces additional oils after the primary and secondary recovery stages. The EOR methods can be classified into main three branches: chemical, miscible and thermal [10,17]. Fig. 1-4 displays various EOR methods. During the EOR stage, a number of techniques based on different liquid or gaseous fluids is prepared and injected into the oil reservoirs, which modifies the chemical/physical properties of oils, liquids and reservoirs. As a result, the oil recovery can be significantly enhanced. For example, surfactant and alkaline flooding can be used to reduce the interfacial tension (IFT) between the water and oil interface, thereby reducing the capillary forces [18]. Polymer can increase the viscosity of injected fluids, which decrease the viscosity ratio of fluid to oil [19]. Consequently, the viscous fingering can be suppressed, improving the oil mobility [20]. Solvent agent is used to eliminate the capillary forces since the water–oil interface presents compositional gradient [21]. Steam provides a high-temperature gaseous liquid, decreasing the crude oil viscosity as well as the viscosity ratio [19]. To understand why these methods could enhance the oil production, we should first figure out the reason why most of oils (above 50% OOIP) are bypassed during the secondary recovery stage. The oil bypassed mechanism will be introduced in Section 1.3.



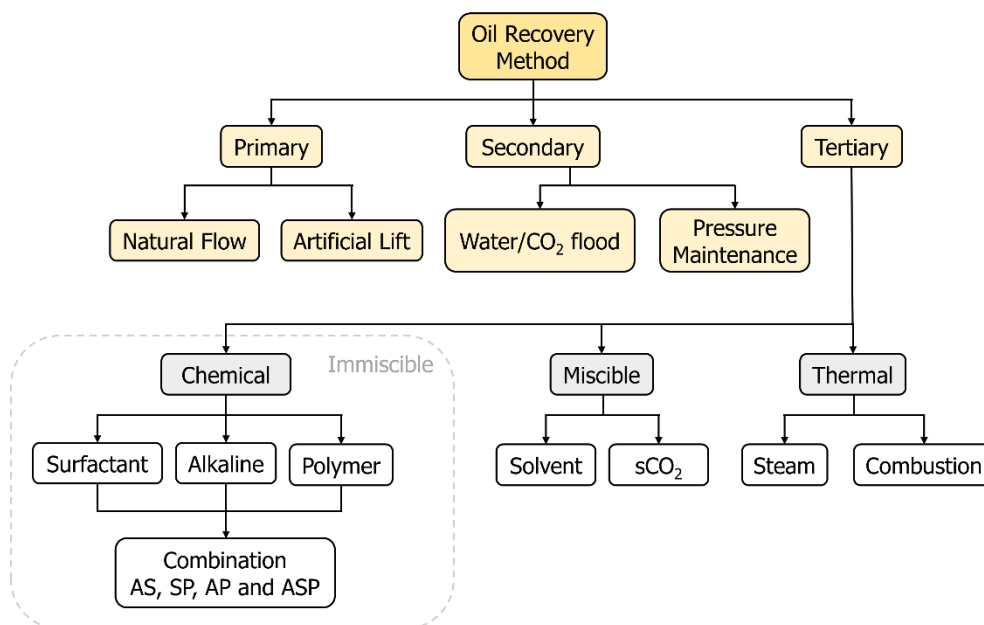


Fig. 1-4. Classification of various oil recovery techniques (adapted from [10,17]). Tertiary oil recovery methods are also called enhanced oil recovery.

### 1.3 Oil bypassed mechanism

Section 1.2 stated that more than 50% OOIP has been left behind in the oil reservoir after the primary and secondary recovery stages. The large fraction of trapped oils can be attributed to the oil bypassed mechanism in both macroscopic and microscopic level. Fig. 1-5 illustrates the schematic of bypassed oils after waterflooding. From a macro-scale perspective, most of oils are bypassed because the viscous fingering (VF) occurs. The viscous fingering is named from its finger-like structure which is a flow instability as a less viscous fluid (water) displaces a high viscous fluid (oil) [22,23]. As show in Fig. 1-5, the fingertip causes an earlier breakthrough to the production wells and most of oils are bypassed in the finger-valley. Consequently, areal sweeping efficiency is low. In addition, the oils are not completely removed even in the water-swept area. From a micro-scale view, we can observe many oil clusters are trapped in the pore spaces, leading to a low microscopic displacement efficiency. The fraction of microscopic bypassed oils can be ascribed to the capillary forces [24]. Therefore, we conclude that viscous fingering and capillary forces are the two main factors preventing higher oil production.

The total oil recovery efficiency ( $E_T$ ) is used to describe how much oil fraction are produced from the reservoirs, including the areal sweeping efficiency ( $E_A$ ) and microscopic displacement efficiency ( $E_D$ ) [25]. Their relationship is shown in Eq. (1-1). From this equation, we can understand that improving  $E_T$  needs to increase  $E_A$  and  $E_D$  simultaneously. Therefore, understanding which factors affect the VF and capillary forces could provide a pivotal guide in improving the total oil recovery efficiency.

$$E_T = E_A \times E_D \quad (1-1)$$

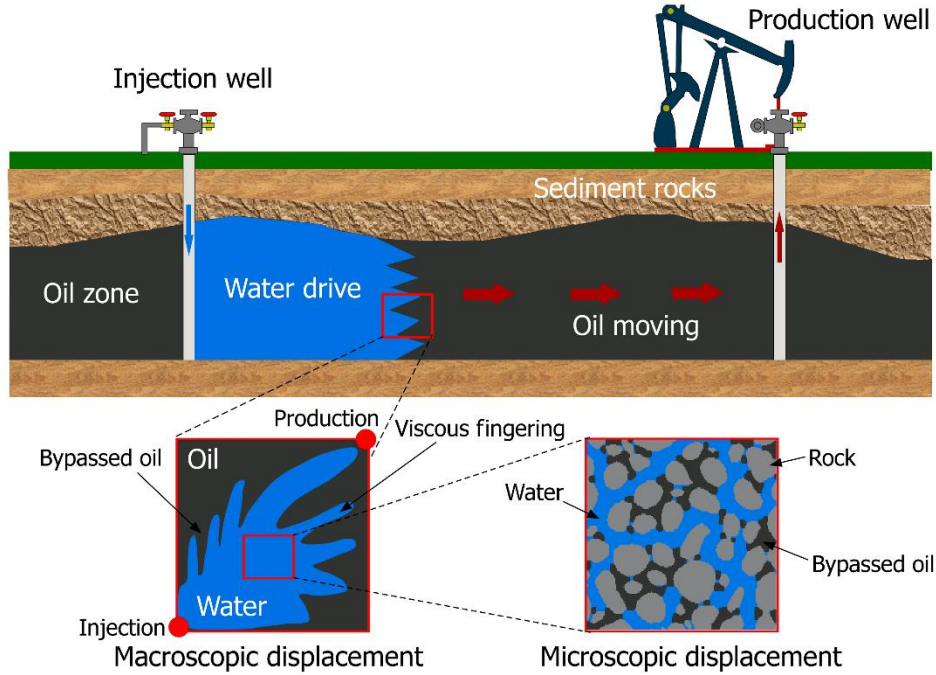


Fig. 1-5. Schematic of bypassed oil after secondary recovery stage

### 1.3.1 Viscous fingering

The (macroscopic) areal sweeping efficiency is significantly restricted by the VF. The VF is induced because of two main factors: viscosity difference and permeability heterogeneity [26,27].

#### 1) Viscosity difference

In natural, the oil phase is more viscous than the water phase. As a rule, the finger-like structure, i.e., VF, is formed when the low viscous water displaces the high viscous oil. Table 1-1 show the viscosity of crude oil varies from 100cP to 10000 cP, indicating the VF may be different for different oil types. The fingering pattern is controlled by the capillary number ( $Ca$ ) and viscosity ratio ( $M$ ) [28–30]. Capillary number is defined as the ratio of viscous force to the capillary force as shown in Eq. (1-2). Viscosity ratio is defined as the viscosity of water phase to that of oil phase (see Eq. (1-3)).

$$Ca = \frac{\mu_w V_w}{\gamma_{ow}} \quad (1-2)$$

$$M = \frac{\mu_w}{\mu_o} \quad (1-3)$$

Where  $\gamma$  is the interfacial tension between the water and oil phases,  $\mu$  is the viscosity of the water phase, and  $V$  is the velocity of waterflooding;  $o$  and  $w$  represent oil and water phases, respectively.

Fig. 1-6 shows fingering patterns are classified into viscous fingering, capillary fingering and stable displacement. Viscous fingering happens under unfavorable viscosity ratios at high injection flow rates while capillary fingering occurs under favorable viscosity ratios at

very low flow rates. The stable displacement means fingering disappears as the viscosity ratios and injection flow rates are both high enough. The ideal areal sweeping efficiency can be obtained in the stable displacement. The three patterns of fingering can be transferred to each other under well-controlled condition [31].

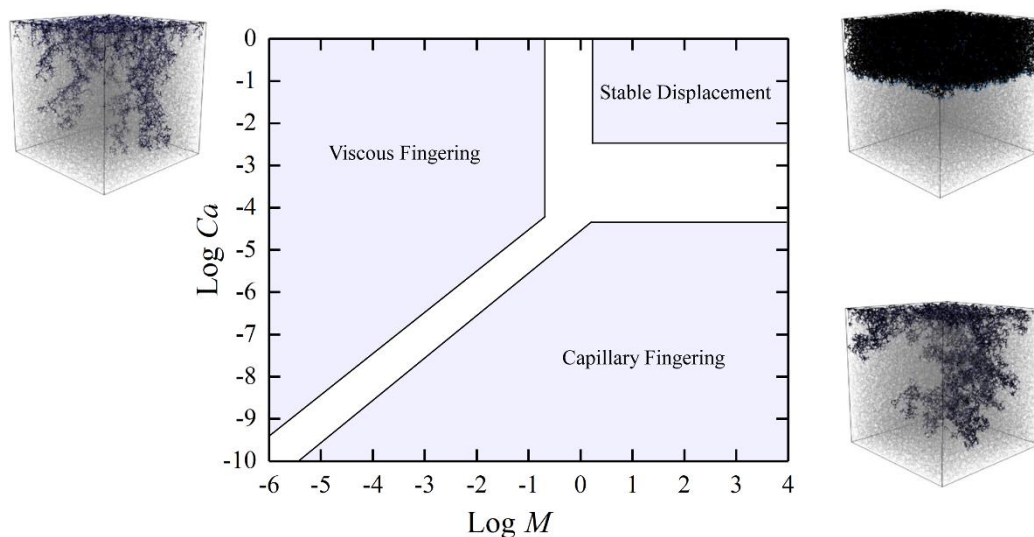


Fig. 1-6. Displacement fingering patterns as a function of capillary number ( $Ca$ ) and viscosity ratio ( $M$ ) (Adapted from [30,31]). Similar diagram can be also found in other reports [28,29].

## 2) Permeability heterogeneity

The permeability heterogeneity also affects the fingering pattern. It is defined as the inherent variation of permeability as a function of space [13]. In the other words, the actual oil reservoirs have different permeable layers ranging from low to high. The low permeable layers are made up of smaller rock pore spaces while the high permeable layers are larger pore spaces. During the waterflooding period, viscous fingering happens when the water flow path transfers from one permeable layer to the other. In general, as the reservoir heterogeneity increases, the bypassed oil will increase, due to the uneven flow path of displacing water [13,32].

Previous researchers reported that the position of fingering patterns in Fig. 1-6 changed when they conducted the displacement in a high heterogenous porous media [33,34]. Through a special design of porous media structure, the viscous fingering can be suppressed without modifying fluid properties [35]. This imply us that the stable displacement can be triggered when applied for some kind of oil reservoirs with special heterogeneity.

### 1.3.2 Capillary forces

The capillary forces, known as capillary pressure, is defined as the pressure difference between two immiscible fluids (e.g., oil and water) in contact with rock solid. The capillary forces are given in Young-Laplace equation as shown in Eq. (1-4) [13,27,36].

$$P_c = P_o - P_w = \gamma \left( \frac{1}{r_1} + \frac{1}{r_2} \right) \quad (1-4)$$

Where  $P_c$  is the capillary pressure,  $\gamma$  is the interfacial tension between water and oil phases,  $P_o$  and  $P_w$  are the pressure in oil and water phases,  $r_1$  and  $r_2$  are the principal radii of the curvature of the water–oil interface.

Fig. 1-7(a) shows the oils are trapped in the pore spaces from a micro-scale view. The oil cluster contacting water phase always presents concave meniscus under control of an interfacial energy balance [36]. Once the balance is stable, the capillary pressure is large enough that trap oil clusters effectively. The capillary rise phenomenon is a simple example that is analogous to the trapped oil in the pore spaces. The size of capillary tubing shares similar magnitude of order with that of pore spaces, reaching micrometer. As a common sense, the water phase will automatically rise up when a capillary tubing sinks into the water phase. The capillary pressure is given as Eq. (1-5) considering  $r_1 = r_2 = r/\cos\theta$  in Eq. (1-4).

$$P_c = \frac{2\gamma\cos\theta}{r} \quad (1-5)$$

Where  $\theta$  is the contact angle between the water and solid phases.

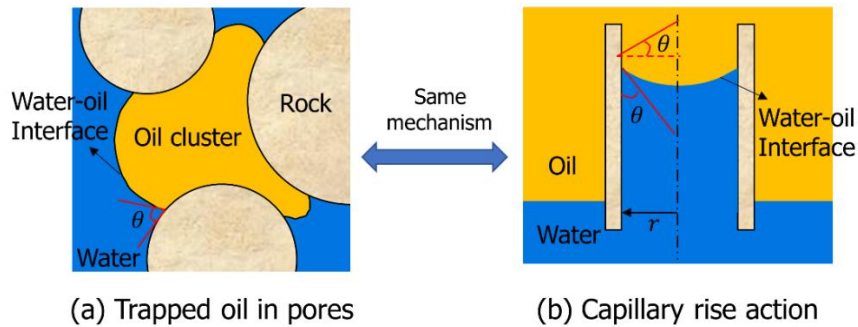


Fig. 1-7. (a) Oil trapped by capillary forces is analogous to (b) capillary rise action.

From Eq. (1-5), we understand the interfacial tension, contact angle and pore size are three important factors that influence the strength of capillary forces. For oil recovery improvement, the capillary forces need to be reduced considering the three factors.

### 1) Interfacial tension

Interfacial tension is defined as the energy per unit area of surface between the phases or the energy difference at the unit area of phase interface between two immiscible fluids, which is expressed as a basic formula (Eq. (1-6)) [36]. In laboratory, the interfacial tension can be measured by pendant drop technique [37].

$$\gamma = \frac{dF}{dS} \quad (1-6)$$

Where  $F$  is the free energy at the fluid interface and  $S$  is the area of interface.

The forces of pendant droplet are balanced between the hydrostatic pressure, capillary pressure and gravitational force [38]. The schematic of pendant drop is shown in Fig. 1-8. The capillary pressure is governed by the Young-Laplace equation (Eq. (1-4)). For an arbitrary point A, the capillary pressure can be described as Eq. (1-7). For the apex O, the capillary pressure can be written as Eq. (1-8).

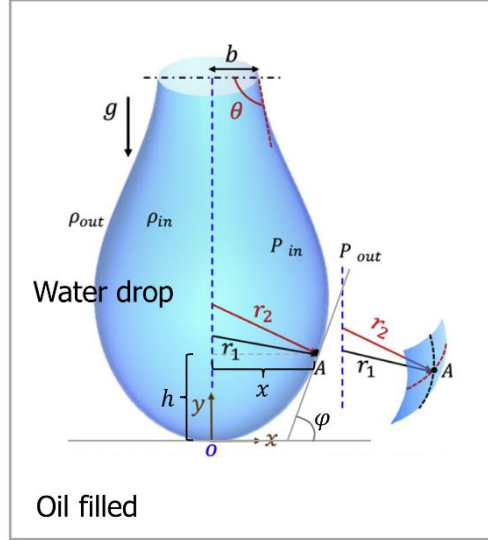


Fig. 1-8. Schematic of a symmetric pendant droplet (adapted from [39]).  $P_{in}$  and  $P_{out}$  are the pressures water and oil, respectively,  $\rho_{in}$  and  $\rho_{out}$  are the water densities of water and oil, respectively,  $r_1$  and  $r_2$  are the principal radii of curvature at any point A, and point O is the apex of droplet.

$$\Delta P_A = P_{in,A} - P_{out,A} = \gamma \left( \frac{1}{r_{1,A}} + \frac{1}{r_{2,A}} \right) \quad (1-7)$$

$$\Delta P_O = P_{in,O} - P_{out,O} = \gamma \left( \frac{1}{r_{1,O}} + \frac{1}{r_{2,O}} \right) = \gamma \frac{2}{r_O} \quad (1-8)$$

The hydrostatic pressure difference between the point A and point O becomes significant with the increasing height  $h$ . Therefore, the hydrostatic pressure difference can be described as Eq. (1-9).

$$\Delta P_A = \Delta P_O - \Delta \rho g h \quad (1-9)$$

Combining Eq. (1-7), Eq. (1-8) and Eq. (1-9), the interfacial tension can be calculated from the pendant droplet, which is governed by Eq. (1-10).

$$\frac{1}{r_{1,A}} + \frac{\sin \varphi}{x} = \frac{2}{r_O} - \frac{\Delta \rho g h}{\gamma} \quad (1-10)$$

Where  $r_{1,A}$  is the radius of curvature at the point A,  $r_O$  is the radius of curvature at the apex O,  $g$  is the gravitational constant,  $\rho$  is the density difference between the water and oil phases,  $\gamma$  is the interfacial tension,  $h$  is the height between point A and O,  $\varphi$  is the tangent angle made by the point A and  $x$  axis.

## 2) Rock wettability

Wettability is used to describe one fluid has a tendency to spread on or adhere to a solid surface in the presence of the other immiscible fluid [13,36]. The wettability can be expressed by measuring the angle of contact through the liquid to the solid surface; this angle is more familiarly known as the contact angle ( $\theta$ ). A sessile drop technique is popularly employed to measure the contact angle [40] by means of one liquid droplet placed on the flat solid surface with other surrounding fluid. Fig. 1-9 illustrates the different rock wettability in water–oil fluid system using the sessile drop method. The contact angle ranges from  $0^\circ$  to  $180^\circ$  corresponding to strong water-wet and oil-wet, respectively. If the contact angle is  $< 90^\circ$ , the water phase is the most wetting phase that preferentially adhere to the rock surface. On the contrary, the oil phase is the most wetting phase if the contact angle is  $> 90^\circ$ . In natural formations, Berea sandstone and carbonate rock are the typical representatives of water-wet and oil-wet rock, respectively. The wettability is an important factor that affects the distribution of water and oil phases in the porous media [41], which determines the oil displacement efficiency.

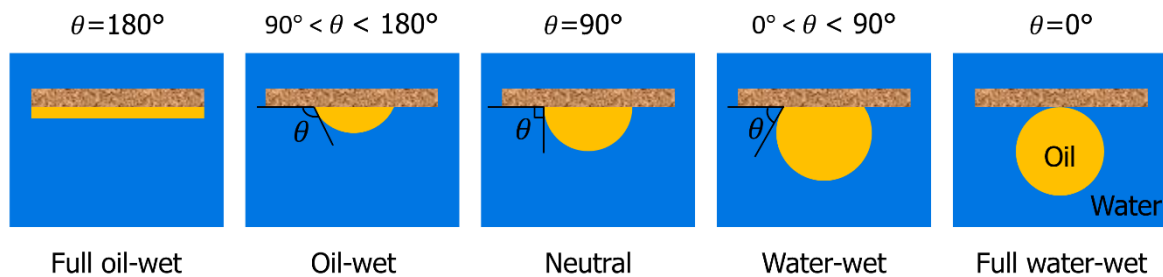


Fig. 1-9. Wettability of oil phase on the flat rock surface with surrounding water phase (adapted from [36]).

In second oil recovery, the wettability order controls the fluid configurations in the pore space; that is, the most wetting phase tends to preferentially occupy small pores and throats, as well as the wetting films attached to the surface, whereas the most nonwetting phase tends to occupy the center of larger pores [36,41]. Fig. 1-10 shows examples of different wettability and oil occupancies in water-wet and oil-wet rock sample, respectively. In principle, the different occupying behavior attributes to the capillary pressure difference (see Eq. (1-5)). If the rock surface is more water-wet, the contact angle ( $< 90^\circ$ ) decreases and capillary pressure for water phase increases. From Eq. (1-5), the pore radius of water occupying should be decreased, and oil phase resides in the larger pore center. Reversely, the more oil-wet (contact angle  $> 90^\circ$ ) will make capillary pressure more negative ( $< 0$  Pa). The negative pressure will push the oil to occupy the small size of pores and throats, leaving water phase stay in larger pore center. Fig. 1-10(a)-(iii–v) and (b)-(iii–v) shows 3D examples of oil occupying the pore space. In a water-wet system, oil as the most nonwetting phase preferentially occupies the center of large pores, whereas in an oil-wet system, oil as the most wetting phase tends to occupy small pores and throats. In oil recovery application, a positive capillary pressure means that water will almost always have sufficient pressure to

mobilize oil out of the pore space. In contrast, if the capillary pressure is negative, a higher water pressure is required to achieve the same oil saturation [41]. Therefore, it is detrimental to oil displacement efficiency for the type of oil-wet reservoirs.

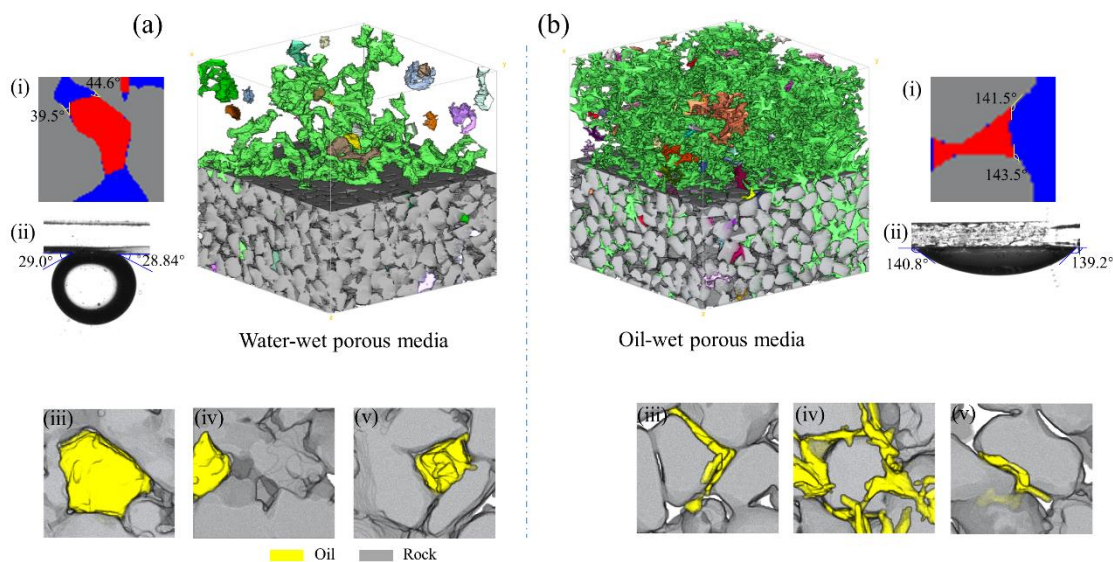


Fig. 1-10. Examples of different wettability (i-ii) and oil occupancies (iii-v) in (a) water-wet and (b) oil-wet rock sample (From Chapter 4, Fig. 4-6).

### 3) Pore-throat size

A porous media contains most of solid material with void spaces inside it. The porosity (Eq. (1-11)) is generally used to characterize the porous media property, which depend on the number and size of void spaces. The void spaces consist of larger pores and smaller throats, and one pore is connected by multiple throats. They play a vital role in determining the permeability and capillary pressure. As shown in Eq. (1-5), the capillary pressure increases as the pore-throat size decreases, which will affect the distribution of water and oil phases in porous media. For an oil-wet reservoir, the smaller size of pores will make the capillary pressure more negative, which hinders the oil movement, significantly. As previously reported, the pore-throat size distribution of rocks can range from nanoscale (e.g., shale) [42] to microscale (e.g., Berea sandstone) [43]. Therefore, the oil displacement efficiency is different as we apply the waterflooding for these reservoirs.

$$\Phi = \frac{V_V}{V_T} \quad (1-11)$$

Where  $V_V$  is the volume of void spaces and  $V_T$  is the total volume of porous media, including the solid and void volumes.

The size of pores and throat can be obtained by the pore-network modelling. The maximum ball algorithm is one of the methods to model the pore-throat structure [36,44], which produces a stick-ball network as shown in Fig. 1-11. In this method, a pore body is inscribed by a maximal sphere (called “ball”) and a throat is inscribed by a series of similarly maximal spheres (called “stick”).

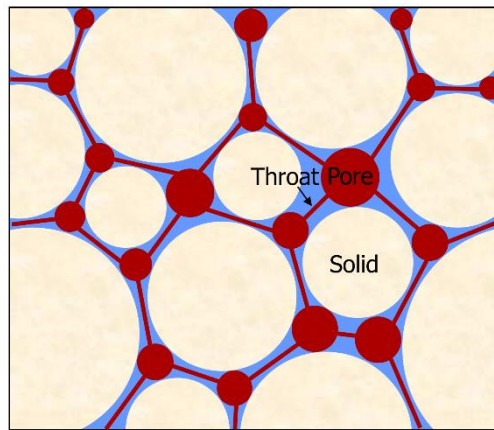


Fig. 1-11. Schematic of pore and throat spaces in porous media and simplified into pore-network model with balls (i.e., pore bodies) and sticks (i.e., pore throats) (adapted from [42]).

## 1.4 Chemical enhanced oil recovery

This study focuses on the chemical EOR (C-EOR), which is one of popular technique among the EOR methods (see Fig. 1-4) owing to its high efficiency and low cost. The C-EOR agents generally include alkaline (A), surfactant (S), polymer (P) and any combination of these processes (AS, AP, SP and ASP) [45]. In a field-scale oil exploitation, the scenario for C-EOR application is shown in Fig. 1-12. The water flooding is followed by a series of chemical flooding sequences. As aforementioned, over 50% OOIP is trapped in the pore spaces after waterflooding. When the chemical agents are injected, the oil recovery is improved because original trapped oils remobilize. The EOR mechanisms of these chemicals are introduced in Section 1.4.1.

### 1.4.1 General mechanisms

Section 1.3 states the oil recovery is less than 50% OOIP after waterflooding because of the viscous fingering and capillary forces. The C-EOR methods can aid for suppressing the VF or reducing the capillary forces.

#### 1) Polymer flooding

The polymer flooding is used to suppress the VF by means of increasing displacing fluid viscosity [15,45]. As show in Fig. 1-6, a stable displacement tends to occur when the viscosity ratio is increased. As a result, oil mobility is significantly improved, thereby increasing the areal sweeping efficiency. Oil mobility is defined as the relative permeability divided by the viscosity of fluid as shown in Eq. (1-12). We often use the term mobility ratio ( $R_M$ ), the ratio of aqueous phase mobility to oil phase mobility, to describe the comparison of aqueous and oil mobilities (Eq. (1-13)) [45]. The polymer flooding can maintain the mobility ratio  $< 1$ , which is considered a favorable mobility ratio.

$$\lambda = \frac{k_{ro}}{\mu_o} \quad (1-12)$$



$$R_M = \frac{k_{rw}/\mu_w}{k_{ro}/\mu_o} \quad (1-13)$$

Where  $k_{ro}$  is the relative permeability to oil and  $\mu_o$  is the viscosity of oil phase,  $k_{rw}$  is the relative permeability to aqueous phase and  $\mu_w$  is the viscosity of aqueous phase.

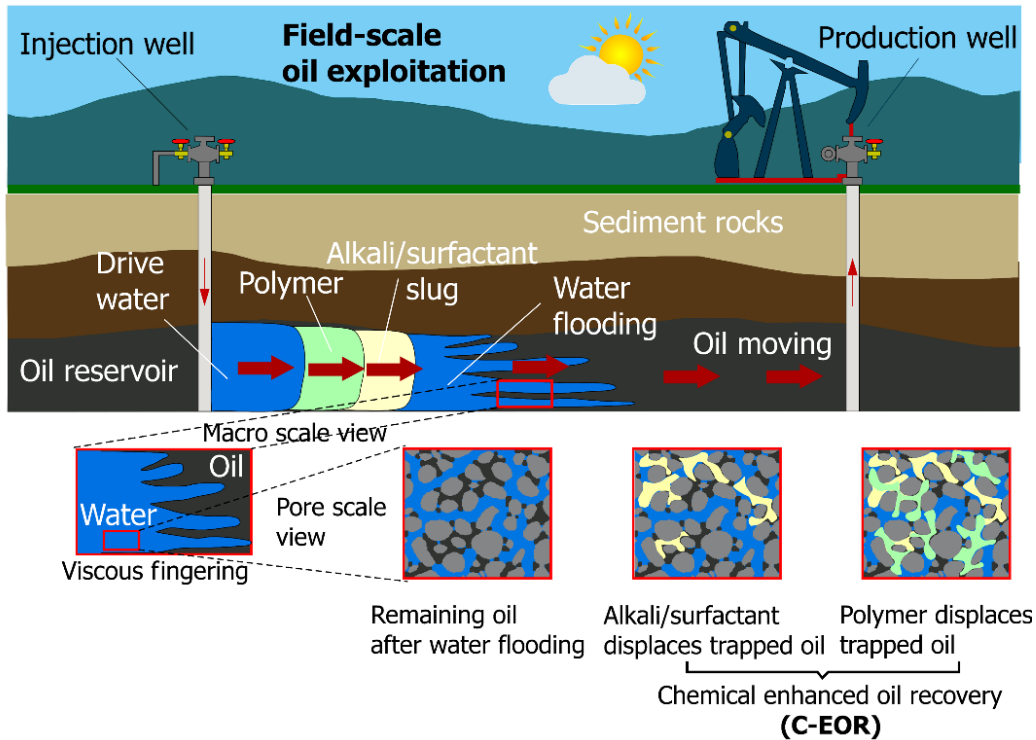


Fig. 1-12. Schematic view of oil recovery by the most popular C-EOR techniques (adapted from [10]).

## 2) Surfactant flooding

The surfactant flooding (SF) represents the direct injection of ready-made surfactant solution for EOR application. The key mechanism of SF is to reduce the interfacial tension and alter the wettability of rock surface [45]. Eq. (1-5) shows that the capillary forces can be reduced when the IFT decreases. In other words, the viscous forces dominate over the capillary forces ( $Ca$  number increases), leading to the oil remobilization (Fig. 1-13(a)) [15]. If the IFT is reduced to ultralow ( $< 10^{-2}$  mN/m), the in-situ emulsification is induced, namely large oil clusters split into many tiny oil droplets in a spontaneous condition [46]. The tiny oil droplets are easy to pass through the pore-throat spaces as shown in Fig. 1-13(b). The surfactant also can alter the rock wettability from oil-wet to water-wet [47], resulting in the aqueous phase change from non-wetting phase to wetting phase. In the other words, the displacement process is transferred from drainage (a non-wetting phase displaces a wetting phase) to imbibition (a wetting phase displaces a non-wetting phase). The capillary pressure changes from negative to positive (see Eq. (1-5)). Therefore, the microscopic displacement efficiency is also improved by the wettability alteration.

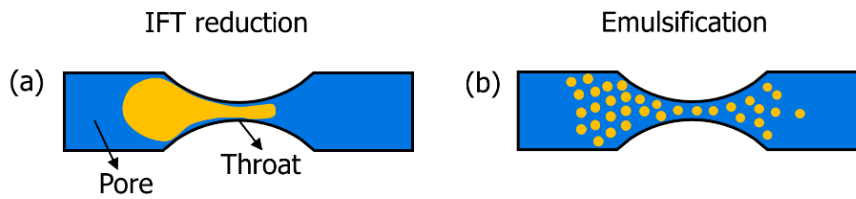
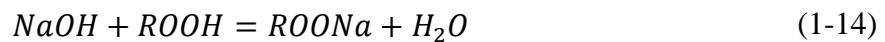


Fig. 1-13. Pore-scale oil movements after surfactant flooding: (a) oil remobilization after IFT reduction and (b) emulsification occurrence when IFT became ultra-low.

### 3) Alkaline flooding

Alkaline flooding (AF), e.g., sodium hydroxide (NaOH) and calcium hydroxide ( $\text{Ca}(\text{OH})_2$ ), relies on the chemical-produced surfactant to remobilize the trapped oil phase. The surfactant is produced in situ by the chemical reaction between the alkali agents and organic acid components in crude oil. That is, the AF shares similar mechanism with the direct SF, including IFT reduction, wettability and emulsification [10,45]. Take NaOH as an example, the chemical reaction formula can be written as Eq. (1-14). Therefore, the alkalis are sensitive to acid components and can be only applied for acidic crude oils.



Wherein NaOH is sodium hydroxide; ROOH is linoleic acid; ROONa is the salt of linoleic acid (sodium linoleate);  $\text{H}_2\text{O}$  is the produced water.

In nature, the crude oils contain a certain number of organic acids, including major naphthenic acid (85%) and organic sulfur compounds. The acids originate from in-reservoir biodegradation. For example, aerobic bacteria can produce organic acids from organic nutrients and generate hydrogen sulfide, which, in turn, can be converted to sulfuric acid (by bacterial action) [48]. The various acid components are described as the total acid number (TAN). The TAN is defined as the mass of potassium hydroxide (KOH) in milligrams that is required to neutralize one gram of acidic oil sample. From measurement, the TAN varies from very low to very high values that ranges 0 ~ 16.2 mg KOH/g depending on different territorial oil reservoirs [49]. Table 1.8 from Ref. [48] shows the highly different TAN values in crude oils from different countries. Therefore, considering different TAN property, the engineering application of AF should be carefully designed for different acid oil reservoirs.

### 1.4.2 Literature review

In this study, our main work is regarding the SF and AF, therefore, the polymer flooding is not reviewed currently.

#### 1) Surfactant flooding

Most common surfactants used in EOR consist of nonionic, anionic, cationic, and zwitterionic types [47,50]. Recently, SF applied for oil recovery has been investigated extensively. IFT reduction [51], wettability alteration [51–53] and emulsification [54–56] have been considered the three dominant mechanisms for EOR. However, different types of

surfactants show different performance depending on the characteristics of rock formation, crude oil, brine and other internal factors, such as pressure and temperature [10]. Therefore, choosing an appropriate surfactant is still a challenging task. For example, anionic surfactants are widely used for sandstone formations owing to their low adsorption. The shortcoming is that they cannot tolerate the harsh conditions of high salinity [57] and temperature [57]. The carbonate reservoirs contain high contents of clay which results in high adsorption of surfactant. In this case, the cationic surfactants are the best choice because of low adsorption [58]. The nonionic surfactants have a good adaption to the high-salinity reservoirs because they have a strong hydrogen bonding (no ionization) and have no charge interactions with brine ions [59]. It has been proven that some dual surfactants, i.e., mixtures of two surfactant types, are more effective than individual surfactant alone [60]. Adding a co-surfactant (alcohol) can improve oil recovery owing to synergistic effects [61]. Undoubtedly, the use of multitype surfactants will increase costs and foster the development of alternatives.

From previous research, the SF is applied for oil reservoirs without considering the effect of oil acidity on its performance. In fact, the oil acid components in crude oil could act as weak anionic surfactants and exist as monomers in the organic phase [62,63]. Sumino et al. found that these monomers can be adsorbed by introducing a novel cationic surfactant in a Petri dish test in which a tetradecane drop with palmitic acid (PA, formula:  $C_{16}H_{32}O_2$ ) was placed on an aqueous phase with stearyltrimethylammonium chloride (STAC, formula:  $C_{21}H_{46}ClN$ ) [64]. They observed that intensive surfactant aggregates accumulated near the water–oil interface [63–65]. The petri dish tests imply us that a dual surfactant formation can combine one type of the new cationic surfactant and in-situ oil acids. In this sense, the cost can be reduced significantly to form a dual surfactant system and apply for the acid oil reservoirs, which needs more investigations.

## 2) Alkaline flooding

In the laboratory, the fatty acids (linoleic acid, lauric acid, palmitic acid, and oleic acid) are added into the oil phase to mimic the acid components in crude oil [23,66,67]. After that, AF has been extensively studied for EOR on a laboratory scale. The mechanisms include the IFT reduction [68,69], wettability alterations [70], emulsification [71,72], and viscoelastic gel blockage [73,74]. Among these mechanisms, the emulsification is the most prominent one, which has been extensively reported. Two kinds of emulsions are mainly observed based on the transparent micromodel experiments, that is, water-in-oil (W/O) and oil-in-water (O/W) emulsions [75]. W/O emulsions are characterized by the connected water emulsified into tiny water droplets inside the oil phase [76]. The viscosity can be significantly increased and even be higher than the oil phase [77]. Consequently, the water mobility is reduced owing to the viscous fingering suppression. Dong et al. pointed out that W/O emulsions could plug the pores and divert the preferential water flow path to the un-swept area [72]. In addition, O/W emulsions are found to coexist with W/O emulsions. The size of O/W emulsions is small enough that enable oil droplets to entrain in the water

phase and flow out of the oil reservoir [71,72]. High oil recovery can be achieved with the proper size of oil emulsions that do not exceed size of pores and throats. In some big pores, it is found that uncounted O/W emulsions accumulates and also block the pores effectively, leading to the flow path change [78]. Therefore, the emulsification by the AF plays a key role in the seepage characteristics as well as the oil recovery.

Emulsification ability is influenced by many factors, such as pore geometry, rock wettability and crude oil properties [75]. For the oil properties, most of researchers focus on the alkaline flooding applied for the low acid oil reservoirs [79–81]. However, the extent of IFT reduction is affected by different acidic fractions in crude oil [82], indicating the emulsification ability may varies from the different acid concentrations in oil reservoirs. This point implies that the alkaline flooding scenario should be optimized when it is designed for different acid oil reservoirs. Unfortunately, there is no current report in this field, which needs more investigations.

## 1.5 Miscible flooding

Miscible flooding implies that the displacing fluid has a good miscibility or mixing zone with the oils in reservoirs [17]. The typical characteristic is that there is no clear interface between the displacing fluid and oils, but it presents a compositional gradient (see Fig. 1-14). Compared with the immiscible flooding, the interface is clearly observed. As stated in the Section 1.3.2, the capillary forces are calculated based on the clear interface. Therefore, the capillary forces in the miscible flooding can be eliminated since the interface is invisible (Young-Laplace equation (Eq. (1-5)) is not applied for this case). As a result, the oil recovery can be significantly improved.

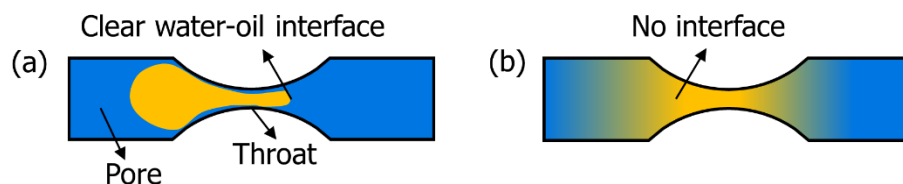


Fig. 1-14. (a) Clear water–oil interface in immiscible flooding and (b) invisible water–oil interface in miscible flooding.

The high oil recovery by the miscible flooding is controlled by the mass transfer instead of the capillary forces [21]. The interface in immiscible fluid system becomes a compositional gradient at which the displacing fluid can disperse into the oil phase (dispersion dominated [83]) and reduce the oil viscosity, which enhances the mobility of the oil phase [21]. The oils could dissolve into the displacing fluid and flow out of oil reservoirs. The miscible-based agents for EOR consist of solvent [21,84] and supercritical gases, e.g., CO<sub>2</sub> [85–87].

However, the miscible flooding usually produced the viscous fingering [22]. Consequently, a large quantity of oils is bypassed, leading to reduction of areal sweeping

efficiency. In addition, direct injecting miscible fluid (e.g., solvent) is very expensive that limits its extensive utilization. Therefore, how to suppress the viscous fingering and lower the cost during the miscible flooding receives many concerns.

## 1.6 X-ray microtomography

The X-ray microtomography (micro-CT) is a powerful non-invasive imaging technique that enables us to visualize the fluid flow behavior in the opaque porous media [41,88,89]. Fig. 1-15 shows a schematic diagram of image acquisition and post-processing by X-ray micro-CT. Initially, the rock sample is fixed in a stage and rotates  $360^\circ$  by itself. Meanwhile, X-ray energies are emitted from a source and get through the rock sample (Fig. 1-15(b)). After that, the tomographic images are obtained based on the different attenuation of materials (fluids and solid) differentiated by a detector. Afterwards, an in-house compatible software is used to reconstruct these tomographic images into stacking image slices (Fig. 1-15(c)). One can refer to previous research for the principle of X-ray imaging in detail [90]. In the final step, a workflow of post image processing is conducted to obtain the fluid-fluid configuration from a direct pore-scale view (Fig. 1-15(d)).

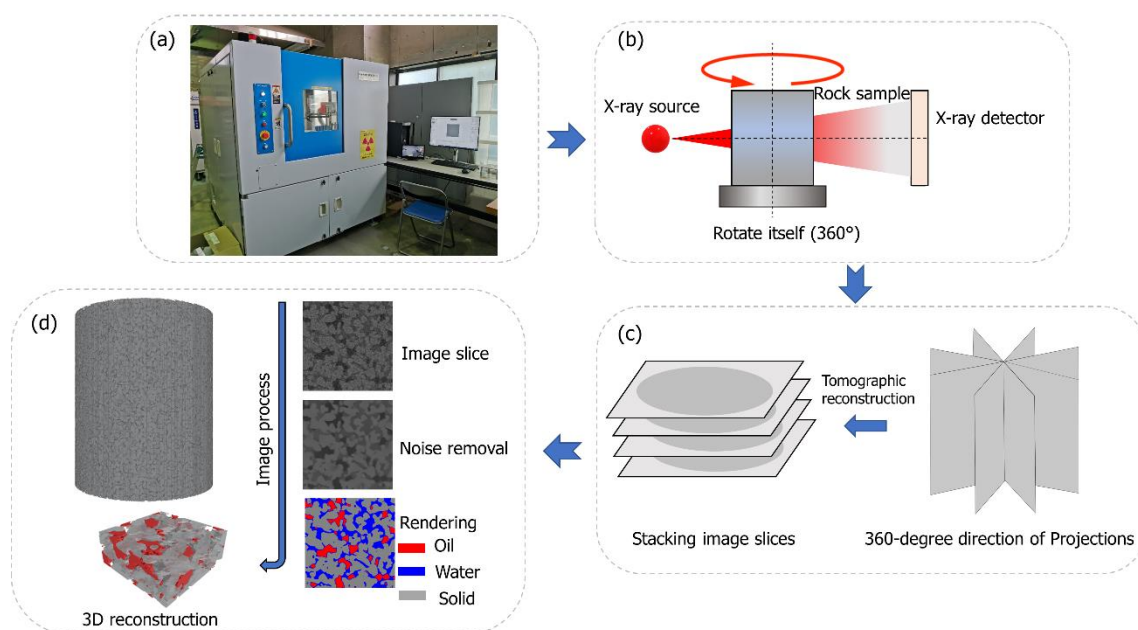


Fig. 1-15. Schematic diagram of image acquisition and post-processing by X-ray microtomography: (a) photo of X-ray workstation, (b) work principle of X-ray device, (c) image tomographic reconstruction and (d) image post-processing sequence.

The fluid flow behavior in actual rock formations has been extensively investigated using this technique [43,59,91,92], such as snap-off, piston-like displacement, and pore-body filling [59,93,94]. The emulsification phenomenon using C-EOR methods has also been captured from a pore-scale view [55,95,96]. The quantitative information (e.g., oil cluster size, surface area, and Euler characteristics) provide an important support for analyzing these pore-scale flow behavior [36].

Thanks to the advanced imaging technique, in this study, we are able to directly observe the oil movement from a pore-scale visualization in the three-dimensional rock sample. As such, we could understand the microscopic displacement mechanism and find an appropriate way to optimize various C-EOR methods.

## 1.7 Current research works

### 1.7.1 Problem statement

(a) The crude oil contains organic acids in nature. In C-EOR engineering, alkaline flooding is applied for reservoirs with acid oils because of chemical-produced surfactants. Surfactant flooding relies on the ready-made surfactant that directly injects for this kind of oils. Previous research mentioned both methods are conducive to EOR. However, the superiority of one type over the other is not clearly classified and the underlying displacement mechanism from a pore-scale view has rarely been reported, which determines the optimal selection of surfactant and alkaline flooding for the acid crude oils.

(b) Previous reports stated that dual surfactants are more effective than a single surfactant alone. If the dual-surfactant system can be formed combining an appropriate surfactant injection and the in-situ oil acids, the surfactant performance may be significantly optimized, and, meanwhile, the cost can be reduced to a large degree. Therefore, this field needs more investigation.

(c) The total acid number in actual oil reservoir ranges from 0~16.2 mg KOH/g. The effect of different oil-acid concentrations on the performance of alkaline flooding is never reported. In petroleum engineering, the scenarios of alkaline flooding application for different acid oil reservoirs should be optimized.

(d) The disadvantage alkaline floodings is that it is strongly dependent on the acid concentrations. Furthermore, although the capillary forces are significantly reduced, it cannot be eliminated. In this case, some oils may be trapped in the pore spaces. Considering this, a miscible flooding is a good choice to eliminate the capillary forces. However, the miscible flooding usually produced intensive viscous fingering and the cost is very high. Therefore, a new modified miscible flooding needs to be created which could eliminate the capillary forces, suppress the viscous fingering and reduce the cost at the same time. If so, the oil recovery can be significantly and cost-effectively improved.

Based on above-mentioned existing circumstances, four major questions need to be addressed in this study:

- (1) Which is more effective and what is the underlying mechanism for acid oil reservoirs between the surfactant and alkaline floodings?
- (2) How to create an in-situ dual-surfactant system relying on only one type of surfactant injection and oil acid components?
- (3) How is the effect of oil-acid concentrations on the performance of alkaline flooding?

(4) How to create a cost-effective miscible flooding that eliminates the capillary forces and suppress the viscous fingering at the same time?

Thanks to the X-ray micro-CT, we are able to address these questions from a direct visualization into the micro pore spaces. The pore-scale oil movements provide direct evidence that the microscopic displacement efficiency is optimized step by step using the various C-EOR methods. A logical structure of four questions is stated in [Section 1.7.2](#).

### 1.7.2 Thesis objective and outline

The objective of this study is to improve the acidic oil recovery by optimizing the various C-EOR methods considering two factors of viscous fingering suppression and capillary forces reduction. By using an X-ray micro-CT, the water–oil configurations from a pore-scale view can be visualized in the pore spaces of opaque rock formations. Consequently, the microscopic displacement mechanisms can be analyzed to examine the oil recovery enhancement when using these various C-EOR techniques. Most importantly, the different chemical methods are optimized step by step and finally the most favorable C-EOR method is proposed for petroleum engineering applications. The thesis structure of this study is illustrated in [Fig. 1-16](#).

In [Chapter 1](#), we provided a background and objective about our study. The current world energy is mainly provided by the crude oils. However, the oil production from oil reservoirs is low and over 50% oils are bypassed during the secondary recovery stage. The oil bypassed mechanisms attributes to the two factors: viscous fingering and capillary forces. It has been extensively reported that various C-EOR methods were tried to adjust these two factors. Although the oil recovery can be improved to a certain degree, some methods need to be optimized considering its efficiency and applied conditions. Therefore, we stated the existing problems and our objective at the end.

In [Chapter 2](#), the performances of surfactant and alkaline flooding for acid oil recovery were compared by the evaluation of interfacial properties and residual oil occupying configuration in the pore spaces. It was found that the alkaline flooding for acid oil reservoirs is more superior than that of surfactant flooding and their underlying mechanisms were provided. Finally, we introduced a novel cationic surfactant to optimize the performance of surfactant flooding. However, the effect of oil-acid concentrations on the performance of alkaline flooding is unknown, which determines the optimization for different acid oil reservoirs. To address this, we go to the next chapter.

In [Chapter 3](#), the effect of oil acid concentrations on the performance of alkaline flooding was investigated. From the pore-scale view, we found the oil recovery efficiency increases with increasing oil acid concentrations because of stronger emulsification ability. A good emulsification has a good control of stable displacement (viscous fingering suppression) and entrainment flow (tiny oil droplets entrain in the aqueous phase and flow out). However, the alkaline flooding for low acid oil reservoirs is not good, namely it depends strongly on the acid concentrations. To solve this problem, we created a new fluid agent in next chapter.

In [Chapter 4](#), we created a solvent-based microemulsion flooding for low acid oil recovery. The emulsion flooding was selected because of its good control of stable displacement. The solvent was added to make the emulsion agent due to its miscible behavior that eliminates the capillary forces. In addition, the solvent-based emulsion could reduce half percentage of solvent use, thereby decreasing the cost. The performance and miscible mechanism of this new agent was investigated from a pore-scale view using X-ray micro-CT. We concluded the solvent-based emulsion flooding has the best performance and can be applied for any type of acid oil reservoirs.

In [Chapter 5](#), we summarized the key conclusions in each chapter and provided the suggestions for future works.

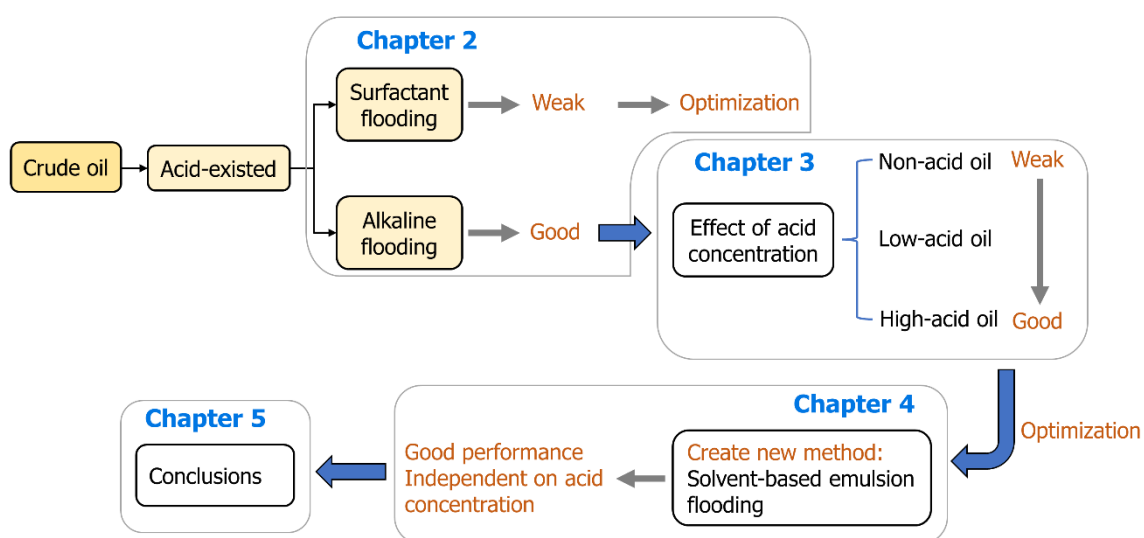


Fig. 1-16. Flowchart of current thesis structure



## 2 Comparative performance of ready-made and chemical-produced surfactants in acid-existing oil reservoirs

**Objective:** In this chapter, the performances of ready-made surfactant and chemical-produced surfactant flooding for acid-existing oil recovery will be compared by the evaluation of interfacial tension, wettability alteration, and emulsification ability as well as the oil recovery efficiency. The superiority of one method over the other will be classified and their underlying mechanisms will be provided. Finally, one of method that has weaker performance will be optimized.

### 2.1 Experimental

#### 2.1.1 Rock and fluids

A miniature (6 mm in diameter and 15 mm in height) fabricated with sintered glass beads (SGB) was used to imitate an actual sandstone in subsurface. We selected SiO<sub>2</sub>-based SGB material as the artificial sandstone because most sandstones are composed of about 60–80% quartz. The quartz material is made up of SiO<sub>2</sub> composition [92,97,98].

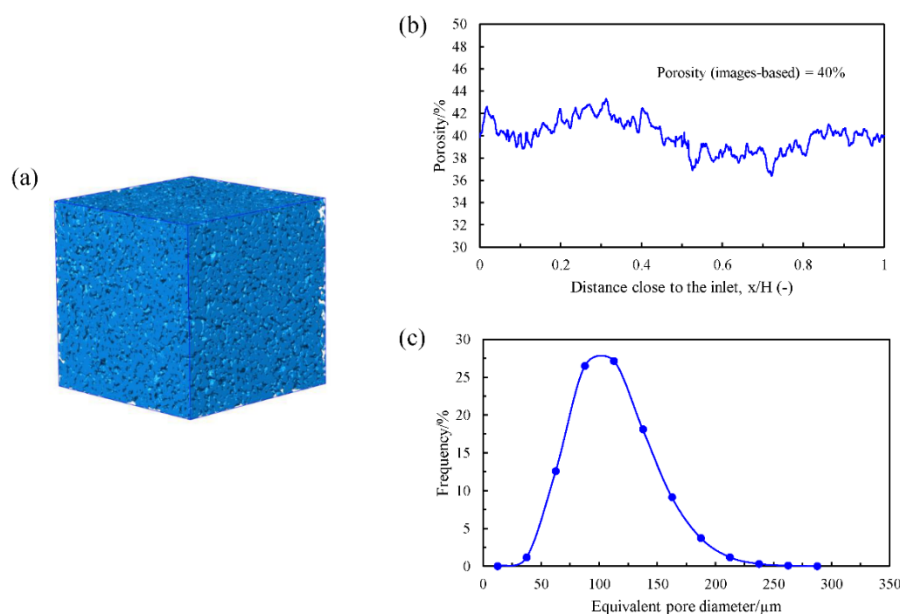


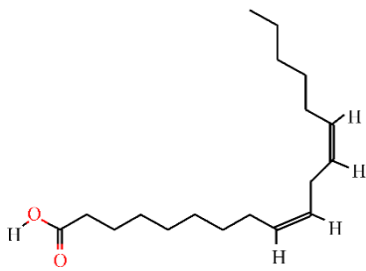
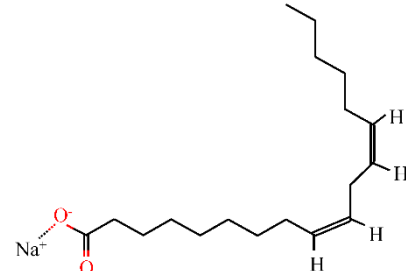

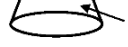
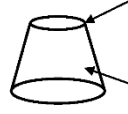
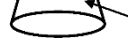
Fig. 2-1. (a) Three-dimensional pore structure, (b) image-based porosity, and (c) pore size distribution of rock sample.

Fig. 2-1 shows the properties of rock sample. The 3D pore structure was exemplified in Fig. 2-1(a), which was reconstructed using an open-source software (UCSF Chimera, University of California). In this region, the porosity was calculated to be 40% using an X-ray CT image scanning (Fig. 2-1(b)). Based on the images, the pore size distribution was extracted using a 3D watershed-segmentation algorithm [99,100] as shown in Fig. 2-1(c). The pore size ranges 10–300 μm with a peak of 100 μm, which agrees well with a broad

range of pore sizes in Berea sandstone [101,102]. The absolute permeability was measured ~11 Darcy by a set of different rates of waterflooding.

Liquid paraffin oil, sodium hydroxide solution (NaOH, 100 mmol/L), and linoleic acid were purchased from FUJIFILM Wako Pure Chemical Corporation (Osaka, Japan). Sodium linoleate was obtained from the Tokyo Chemical Industry Co., Ltd, (Tokyo, Japan). All chemicals were used directly with no further filtration or purification. The linoleic acid was doped into the paraffin oil to mimic the organic acid components in the crude oil. It is noted that linoleic acid, a type of fatty acid, can act as a weak surfactant to reduce the IFT and alter the wettability. However, the effect of this acid on the IFT and wettability is much lower than that of its sodium salt, i.e., sodium linoleate [62]. Sodium linoleate is a strong anionic surfactant that can effectively reduce the IFT and thereby induce an emulsification process. Table 2-1 compares the properties of linoleic acid and sodium linoleate. The hydrophilic–lipophilic balance of linoleic acid and sodium linoleate were estimated to be 1 and 18, respectively, according to the method of Davies [103], indicating that linoleic acid is preferentially oil soluble and that sodium linoleate is strongly water soluble. The critical micellar concentration (CMC) of linoleic acid and sodium linoleate are 0.15 mM and 4–5 mM, respectively [104].

Table 2-1. Properties of linoleic acid and sodium linoleate.

Name	Linoleic acid	Sodium linoleate
Molecular formula	$C_{18}H_{32}O_2$	$C_{18}H_{31}NaO_2$
Structure		
Molecular weight (g/mol)	 Molecular Weight: 45.02 g/mol (Head group)  Molecular Weight: 235.42 g/mol (Tail group)	 Molecular Weight: 67.00 g/mol (Head group)  Molecular Weight: 235.42 g/mol (Tail group)
HLB	1 (oil soluble)	18 (water soluble)
CMC (mM)	0.15	4–5

The core flooding experiments includes three systems of water flooding (WF), surfactant flooding (SF), and alkaline flooding (AF). Throughout all the experiments, the defending fluids were prepared with paraffin oil doped with 100 mM linoleic acid, which imitated natural crude oil with a total acid number of 6.4 mg KOH/g. In the WF system, the invading fluids were prepared only with de-ionized (DI) water. For the SF system, 100 mM sodium linoleate used as an anionic surfactant was dissolved into the DI water. For the AF system, 100 mM NaOH solution was used as received from the company. It is noted that 4 wt.% NaI

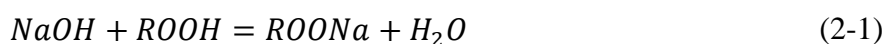
was added into each invading fluid to enhance the discernment of the water and oil phases during the X-ray CT scanning. Each fluid was stirred overnight to ensure uniform solute dissolution using a magnetic homogenizer. The anionic surfactant powder was well dissolved with an aid of ultrasonic homogenizer (ASU-6M, As One, Japan) for 60 min [105–107]. The fluid viscosity was measured by using a viscometer (Sine-wave Vibro Viscometer-SV 10, A&D Co., Ltd., Japan). The viscosities of defending and invading fluids were 89 and 1.25 mPa·s, respectively. The densities of defending and invading fluids were 0.837 and 1.02 g/mL, respectively. The fluid pairs used in the core-flooding systems are shown in Table 2-2.

Table 2-2. Fluid pairs used in the miniature core-flooding experiments. The invading liquid was doped with 4 wt.% NaI to enhance the image contrast among the solid, oil, and water phases.

System	Invading liquid	Defending liquid
WF	Deionized water + 4 wt.% NaI	
SF	Deionized water + 100 mM sodium linoleate + 4 wt.% NaI	Paraffin oil + 100 mM linoleic acid (total acid number = 6.4 mg KOH/g)
AF	Deionized water + 100 mM sodium hydroxide + 4 wt.% NaI	

Note: WF, SF and AF represent water flooding, surfactant flooding and alkali flooding, respectively.

In this study, the ex-situ surfactant flooding (SF) denotes that the core sample was flooded using a ready-made surfactant solution, whereas the in-situ surfactant flooding indicates that the core sample was flooded with alkaline solution by which the surfactant was produced in situ under a chemical reaction. In the AF system, chemical-produced surfactant is governed by the chemical reaction equation given in Eq. (2-1). It should be noted that chemical-produced and ready-made surfactants share the same material and concentration in the core-flooding system. The oil displaced by WF provided a good reference for SF and AF systems.



Wherein NaOH is sodium hydroxide; ROOH is linoleic acid; ROONa is the salt of linoleic acid (sodium linoleate); H<sub>2</sub>O is the produced water.

## 2.1.2 Methodology

### 1) Preliminary test

A tube test was used to observe the stability of emulsions during 0, 1, and 24 h of aging for the surfactant and alkali systems. Prior to being poured into a graduated cylinder, 10 mL specimens of chemical solution and oil phase were mixed and stirred in a beaker at 700 rpm for 60 min. Then, the photographs of the mixtures were captured using a digital camera (R6, Canon, Japan). In the meanwhile, the fresh mixtures were transformed into a Petri dish and examined under a microscope (YDU-3S, Yashima Optical Co., Japan). The diameter distribution of emulsion droplets was extracted by the ImageJ program. Note all tests were implemented at a room condition.

The pendant-drop method was employed to measure the IFTs between the oleic phase and the water phase using a drop shape analyzer (DSA 25, Krüss Scientific, Germany). This device was also configured for contact angle (CA) measurement through the sessile-drop technique. Flat glass substrates composed of the same  $\text{SiO}_2$  material as that of the SGB were used to enable the invading fluid to form droplets gravitationally on the surface with the surrounding oil [108]. During each IFT and contact angle (CA) measurement, the data were acquired until reaching the equilibrium condition; this process was repeated at least twice to ensure data reliability. All measurements were conducted under a condition of room temperature and pressure.

## 2) Experimental setup and procedures

As shown in Fig. 2-2(a), the miniature core-flooding system was composed of three main parts: miniature sandstone, a fluid flooding system, and an X-ray micro-CT scanner. The sandstone (6-mm diameter and 15-mm length) was covered by an acrylic sleeve with 8 mm in outer diameter and 15 mm in length, as received from the company. The acrylic sleeve was sealed with heat shrink tubing (Teflon material, 8.03-mm inner diameter) by heating to shrink at 150 °C using a heat gun (Bosch, Germany). A syringe pump (KDS 200, KD Scientific, United States) was used to inject the aqueous phase downward to displace the oil phase in the sandstone. The core-flooding system was configured with a high-resolution X-ray micro-CT scanner (ScanXmate-CF110TSS300, Comscantecno Co., Ltd., Japan), which was used for visualization of oil movement in porous media. In this study, the resolution was determined to be 3.6  $\mu\text{m}/\text{pixel}$  by adjusting the core sample position close to the X-ray source. During each CT scanning, the sample was rotated 360° to complete one image dataset acquisition within 20 min (two frames/s). To remove the noise and beam hardening, a voltage of 70 kV and current of 120  $\mu\text{A}$  were confirmed as optimal setting. One scanned image stack contained 1300 slices in height (distance between two neighboring slices was 1 pixel) and  $2304 \times 2304$  pixels in width and length, respectively. The sketch of image stacks is shown in Fig. 2-2(b). The field of view (FOV) covering the entire area for each scanning was  $8.3 \times 8.3 \times 4.7 \text{ mm}^3$  in a cuboid volume.

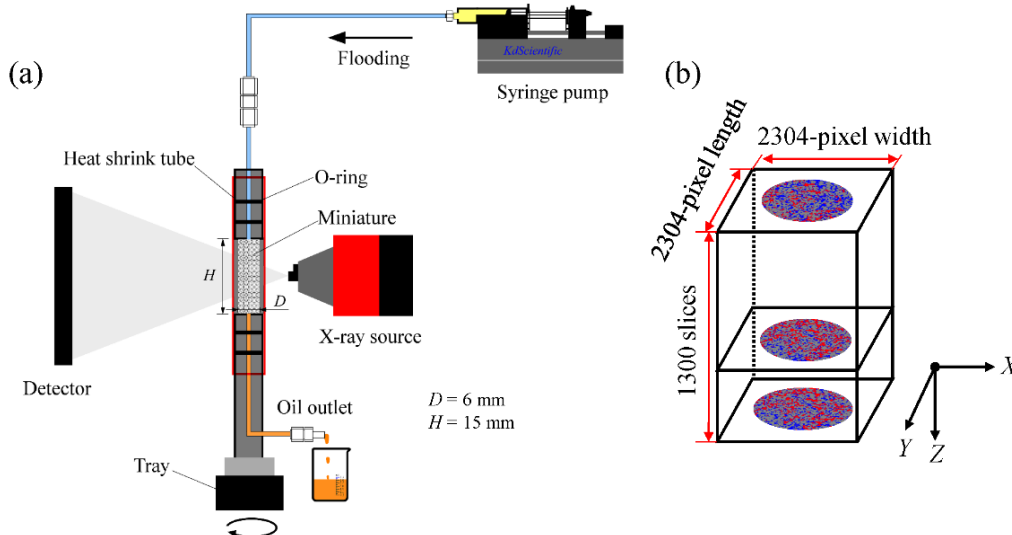


Fig. 2-2. (a) Schematic diagram of miniature core-flooding system and (b) sketch of X-ray CT scanning for image stack.

To verify whether the FOV was able to represent the entire core sample, representative elementary volumes (REV) of porosity and residual oil saturation in the sub-cubical volumes [59,109] were calculated as shown in Fig. 2-3. The REV is the smallest volume that can be used to describe the general oil occupancies in porous media. As shown in this figure, the REV was calculated as  $10 \text{ mm}^3$  which is 13 times smaller than the FOV of sandstone. To conserve image processing time and computer memory,  $3.5 \text{ mm} \times 3.5 \text{ mm} \times 4 \text{ mm}$  of the cuboid volume was selected for the subsequent image analysis. This selected sub-volume was five times larger than that of the REV and was therefore able to represent the oil displacement phenomenon for the entire sample.

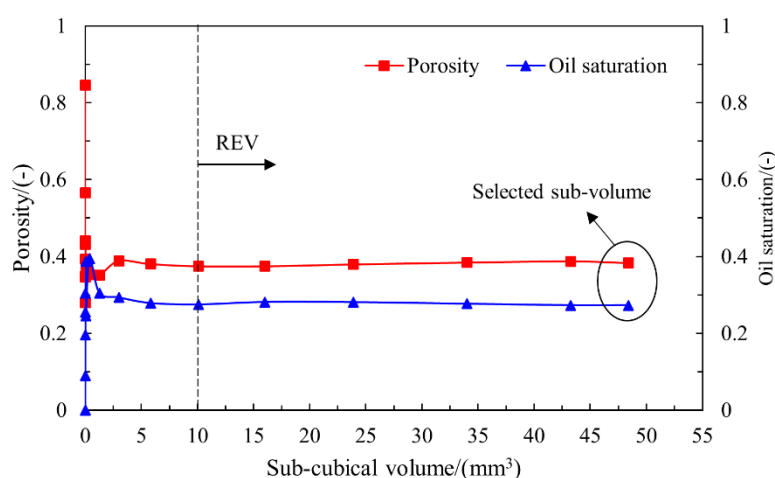


Fig. 2-3. Representative elementary volumes (REV) of porosity after dry scan and oil saturation after surfactant flooding with 15 pore volume (PV) injection.

The miniature core-flooding scenarios outlined in Table 2-2 were implemented according to the following procedures. The miniature sandstone was mounted vertically between the X-ray source and detector and adjusted the resolution to be  $3.6 \mu\text{m}/\text{pixel}$ . Initially, a dry miniature was scanned to obtain the properties of rock sample (see Fig. 2-1). Then, the core sample was flushed with  $\text{CO}_2$  for 30 min to remove the air and transferred into a vacuum chamber. In this step, the sample was fully saturated with DI water. This step guaranteed that there was no air or  $\text{CO}_2$  remained in the pore spaces. An additional CT scanning was conducted to confirm that water saturation reached 100%. Afterward, a drainage process [non-wetting phase (oil) displaces wetting phase (water)] was performed upward at a flow rate of  $100 \mu\text{L}/\text{min}$  until the residual water was irreducible. This process was to obtain an initial connate water condition. The connate water saturation was confirmed to be 24% by another CT scanning. Finally, an imbibition [wetting phase (water) displaces non-wetting phase (oil)] process was carried out that the aqueous phase was injected downward to displace the oil phase at a flow rate of  $250 \mu\text{L}/\text{min}$ . The injection pore volumes (PVs) of aqueous phase were 1, 5, 10, 15, and 20 PV in a continuous mode. During each injection, the oil phase occupying in pore spaces were recorded by the X-ray CT scanning.

All experiments were done using the same miniature, which indicated the identical properties of porous media. This enabled us to study the effects of ex-situ and in-situ surfactant flooding on the residual oil occupancies with similar pore structures. To this end, the sandstone was rigorously rinsed at the end of each core-flooding experiment. The cleansing of miniature was alternatively followed by injection of 100 PV ethanol (60 v/v%) and 100 PV DI water. This step was repeated for twice to ensure complete cleaning. The cleaning procedure had a negligible effect on the phase configurations in pore spaces because all the connate water saturations were similar.

### 3) Image processing

Fig. 2-4 shows the image processing workflow for the core-flooding experiments. The raw images were captured by X-ray CT scanning (Fig. 2-4(a)), and the noise was removed using a non-local means filter (Fig. 2-4(b)). The non-local filter can preserve the edges of the three phases in the raw image. Detailed information can be found in previous publications [110–113]. As shown in Fig. 2-4(d), the gray values fluctuated along the downward yellow line before noise removal, which was hard to segment the phases. After noise removal, the gray values became smooth (Fig. 2-4(e)) and it was favorable to segment the solid, oil and water phases using a histogram threshold method [113]. Subsequently, three phases were combined into a clear and aesthetic-pleasing 3D image as shown in Fig. 2-4(c). After the oil phase was solely obtained, the 3D Object Counter and MorphoLibJ plugins were employed to label and digitize the trapped oil phase in the 3D pore spaces. As a result, the quantitative information of oil volume, interfacial area and Euler characteristics was extracted from the CT images. All images were processed by an open-source ImageJ software (National Institutes of Health, USA).

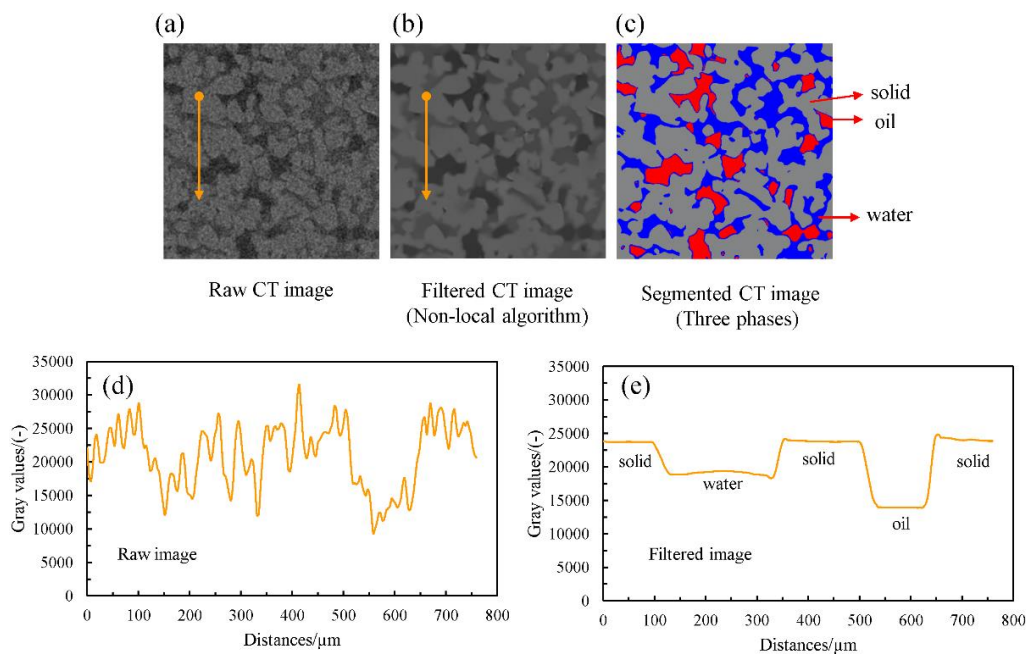


Fig. 2-4. Image processing workflow after core flooding. (a) Raw CT images. (b) Filtered CT images. (c) Segmented three-phase CT images (rock, oil, and water phases are marked with gray, red, and blue colors,

respectively. (d) Gray values fluctuating along the downward yellow line before noise removal. (e) Smoothed gray values along the downward yellow line after noise removal.

## 2.2 Results and discussion

### 2.2.1 Tube test and microscopic visualization

Tube testing was conducted to examine the emulsion stability of the surfactant and alkali systems. As shown in Fig. 2-5(a), the emulsion formation in the surfactant system was less stable than that of alkali system. Specifically, the emulsion volume in surfactant system was 20 mL at the initial time (0 h). After aging for 1 h and 24 h, the value changed from 12 to 10 mL, respectively. Moreover, the emulsion phase was observed to be milky white, which indicates precipitation of the surfactant. This implies that the effect of ex-situ surfactant flooding on IFT, wettability, and oil recovery is weaker in the porous media. In contrast, the emulsion phase in the alkali system appeared to be transparent and more stable at the aging time since the volume was maintained 10 mL. To evaluate the emulsification ability of ex-situ and in-situ surfactants, the size distribution of the emulsion droplets was examined using a microscope. As shown in Fig. 2-5(b), both the ex-situ and in-situ surfactants produced O/W emulsions. However, the oil globules in the ex-situ cases were larger and more regular than those in the in-situ cases. The irregularity of oil droplets in the alkali system indicates the presence of surfactant films produced at the oil–water interface that are easily ruptured by volume forces [114]. In addition, this film substance could also be a steric barrier toward coalescence [96].

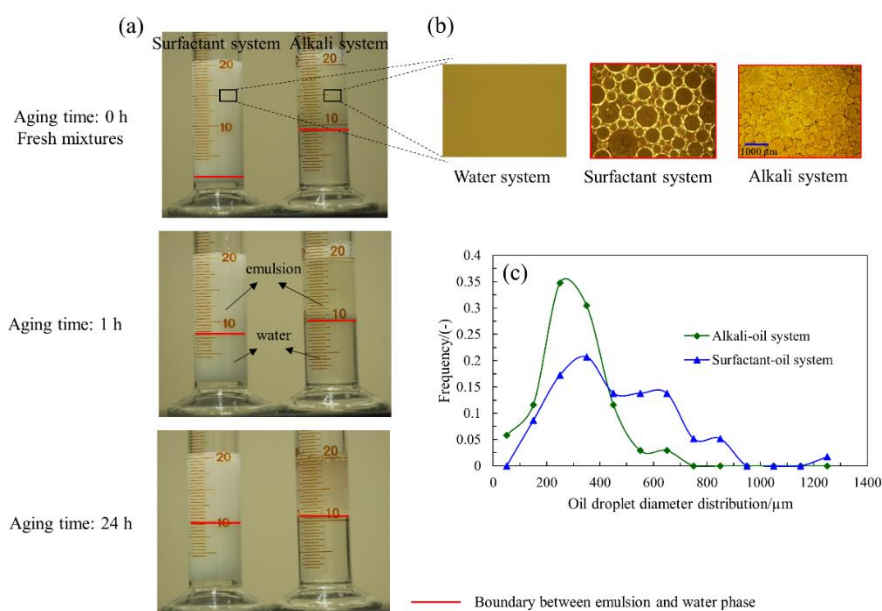


Fig. 2-5. Tube test and microscopic observation of oil–water mixtures in surfactant and alkali systems. (a) Emulsion stability with different aging times (from top to bottom, aging for 0, 1, and 24 h; red bold line denotes the boundary between emulsion and water phase). (b) Microscopic visualization of emulsions in water, surfactant, and alkali systems ( $\times 50$  magnification). (c) The distributions of emulsion droplet diameters based on the microscopic visualization in which more than 50 droplets were evaluated using

ImageJ software.

The quantitative size distribution of oil droplets is described in Fig. 2-5(c). The distribution of oil globule diameters presented two peaks of 350  $\mu\text{m}$  and 250  $\mu\text{m}$  in the ex-situ and in-situ systems, respectively. Furthermore, many large sizes of droplets ranged from 600  $\mu\text{m}$  to 1200  $\mu\text{m}$  in the ex-situ system, whereas most of globules distributed were less than 600  $\mu\text{m}$  in the in-situ system. Therefore, the emulsification ability is much stronger than that of ex-situ system, which implies its better solubilization and mobilization in the pore spaces of sandstone.

### 2.2.2 IFT and wettability measurement

Fig. 2-6 illustrates the results of IFT and CA measurement for the water, surfactant, and alkali flooding systems in an equilibrium condition. The IFT value in water system was 12.6 mN/m, and pendant drop was largest at  $\sim 6 \mu\text{l}$  in volume. In the surfactant system, the IFTs were reduced significantly to 3 mN/m, and pendant drop formed was much smaller than that of water system, at a volume of  $\sim 0.9 \mu\text{l}$ . However, the pendant drop could not form in the alkali system because the IFT was less than 1 mN/m and beyond the measurement range. This result agrees well with that in previous research [74]. Nevertheless, it was supposed that the IFT was in range of 0.01–0.1 mN/m according to a previous test [115]. Therefore, the IFT was largely reduced by two orders of magnitude compared with that in the surfactant system. It implies that the chemical-produced surfactant may be more effectively formed at the oil–water interface [116], whereas the ex-situ surfactant relied on a slow transport to the interface [117].

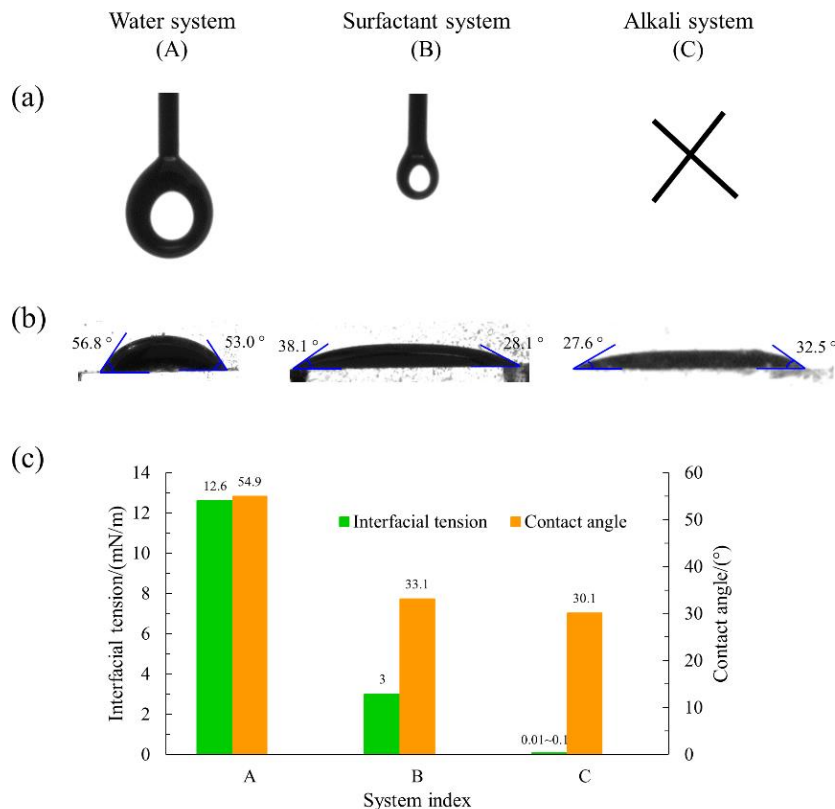




Fig. 2-6. (a) Interfacial tension measurement by the pendant-drop method. (b) Wettability measurement of the contact angle by the sessile-drop technique. (c) Quantitative information of interfacial tension and contact angle in the water, surfactant, and alkali systems.

The wettability is slightly altered by the alkali and surfactant flooding. In the water system, the average CA was  $54.9^\circ$ , which revealed that the sandstone was initially water wet. In the surfactant system, the wettability became strongly water-wet with a CA of  $\sim 33.1^\circ$ . Similarly, the wettability was also strongly water-wet in the alkali system, in which the CA, at  $\sim 30.1^\circ$ , showed a slight reduction compared with that in the surfactant system. The wettability alteration of the ex-situ surfactant can be attributed to the “ion pair” formation mechanism [118] via interaction between the carboxylic acid group and the surfactant; that of the in-situ surfactant can be explained by electrostatic or hydrogen bond interactions [70].

### 2.2.3 Miniature core-flooding experiments

#### 1) Oil recovery performance

Fig. 2-7 displays the oil recovery performance at the end of various flooding experiments in the FOV. In Fig. 2-7(a), the X-ray CT images show 3D configuration of the residual oil phase at the end of 20 PV injection. In the WF system, the oil phase was well connected throughout the sample, which was marked with red color. This indicates that the oil recovery was very low because a large amount of oil was trapped in the pore spaces. During the SF, the volume of well-connected oil phase decreased, and many disconnected oil clusters appeared. In contrast, the well-connected oil phase in the AF system disappeared and were completely split into many separate oil ganglia and singlets owing to the strong emulsification process. Fig. 2-7(b) shows the variation of total oil volume and oil cluster number. The total oil volume decreased from  $8.6 \text{ mm}^3$  to  $2.5 \text{ mm}^3$ , and the oil cluster number increased steadily from 21538 to 62280 in the water, surfactant, and alkali systems. That is, the emulsification ability from the in-situ surfactant was much stronger than that of the ex-situ surfactant, which agrees well with the microscopic observations (Fig. 2-5(c)). The quantitative oil recoveries are illustrated in Fig. 2-7(c). At 20 PV injection, the final oil recovery in the AF and SF were highest and intermediate, corresponding to efficiencies of 86.9% and 69.6%, respectively. The lowest oil recovery occurred in WF with 55.4% efficiency. In the AF system, the highest developed emulsification produced a large quantity of small oil droplets, thereby leading to an effective “emulsion–entrainment” flow, in which small oil globules are entrained in the main flowing stream and easily pass through the pore spaces [119]. This result also agrees very well with “smooth flow mode” in the high-efficiency emulsification zone [120].

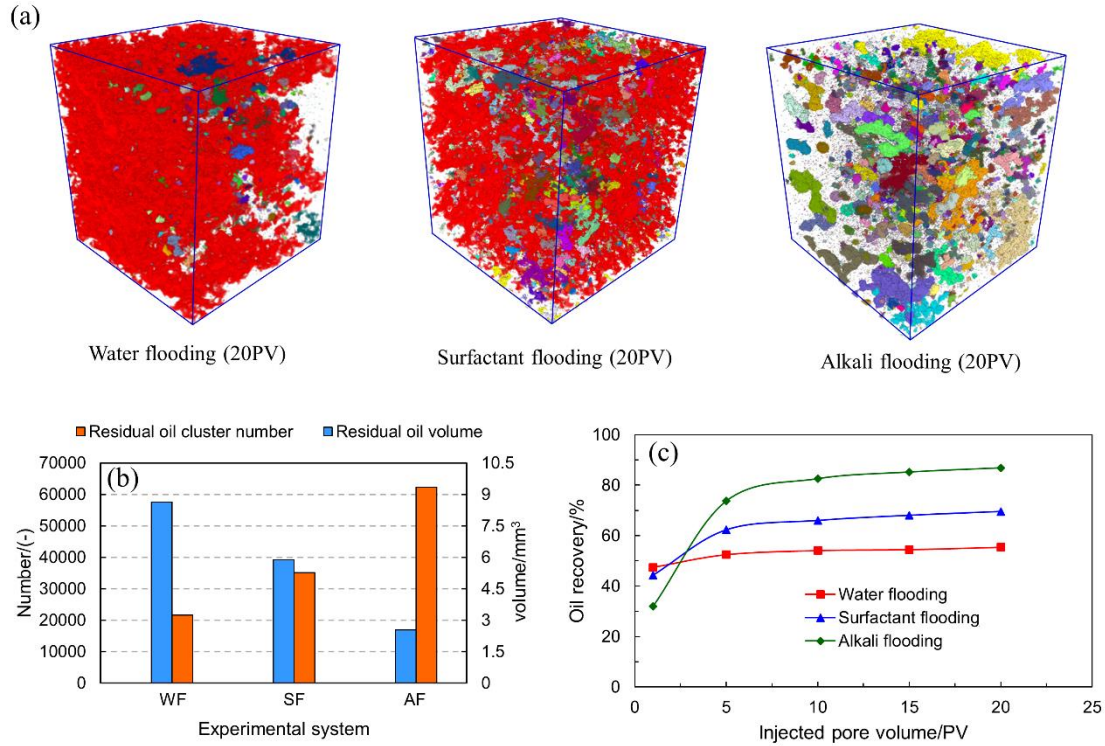


Fig. 2-7. Residual oil configuration at the end of 20 PV injection in the water, surfactant, and alkali flooding systems. (a) 3D images of trapped oil clusters (different colors denote disconnected oil clusters). (b) Statistical residual oil volumes and cluster numbers for WF, SF and AF systems, respectively. (c) Oil recovery efficiency as a function of injection PV.

## 2) Microscopic oil displacement

The capillary number ( $Ca$ ) is a key parameter defined as the capillary–viscous force ratio (Eq. (2-2)) that controls the oil cluster trapping and mobilization of invading fluid in porous media. In this study, the  $Ca$  values were calculated to be  $Ca = 2.6 \times 10^{-5}$ ,  $7.3 \times 10^{-5}$ , and  $2.1 \times 10^{-3}$ – $2.1 \times 10^{-2}$  for the WF, SF, and AF systems, respectively. Therefore, both the WF and SF systems belong to the capillary–viscous flow regime, whereas that for the AF is a dominant viscous-flow regime [20,94].

$$Ca = \frac{\mu u}{\gamma \cos \theta} \quad (2-2)$$

Wherein  $u$  is the cross-sectional velocity of the invading fluid,  $\mu$  is the dynamic viscosity of invading fluid, and  $\gamma$  is the interfacial tension at the oil–water interface.

Fig. 2-8 shows a 2D cross-sectional image of the dynamic oil displacement by invading fluid at a series of 1, 5, and 20 PV injections. More than half of the oil phase was left behind after WF. The oil recovery performance was not effective because the capillary forces trapped the oil clusters in the pores. That is, the displacement forces were unable to overcome the threshold capillary pressure during the dynamic processes. The threshold pressure can be estimated by Young–Laplace equation in Eq. (2-3) [121]. Fig. 2-1(c) and Fig. 2-6(c) show that the average pore radius was found to be 56  $\mu\text{m}$ , and the IFT and CA were

12.6 mN/m and 54.9°, respectively. Therefore, the threshold pressure was approximately 258.75 Pa. In addition, the close-ups indicate that the pore dynamic displacing events were dominated by two main mechanisms: piston-like displacement and pore-body filling, generally occur in the water-wet porous media [59]. The piston-like events occurred in the main terminal meniscus, where the oil phase was displaced by the water phase through an advanced piston movement [93]. The pore-body filling events means one or more pore body initially occupied by the oil phase has been filled by the water phase [122]. Note that there is no emulsification occurred without the participation of surfactants in the pore events.

$$p_c = \frac{2\gamma\cos\theta}{R} \quad (2-3)$$

Wherein  $p_c$  is the threshold capillary pressure,  $R$  is the pore or throat radius, and  $\theta$  is the CA.

In the SF system, oil clusters in the originally uninvaded pore sites of WF system were mobilized and solubilized by participation of surfactants, which resulted in 14.2% additional oil recovery compared with that by WF. This phenomenon can attribute to the aspects of IFT reduction, wettability alteration, and weak emulsification. The surfactant additive reduced the IFT from 12.6 mN/m to 3 mN/m, thereby resulting in a maximum fourfold increase in the  $Ca$ . This means that the viscous force was significantly increased compared with the capillary force. Furthermore, the wettability was altered from weakly water-wet to strongly water-wet. Therefore, the threshold pressure was reduced significantly with the combined IFT and wettability changes. As shown in Eq. (2-3), the threshold pressure was estimated to be 89.76 Pa in the SF system. The reduction in threshold pressure enables a lower displacement force can improve the oil remobilization. As shown in close-ups of Fig. 2-8, the weak emulsification process was observed through the partially small oil droplet formations in the pores. Therefore, a large fraction of oil was mobilized in the form of oil droplets that were smaller than the pore size. Moreover, both piston-like and pore-body filling mechanisms were also observed in the dynamics. This result provides direct evidence that the emulsification process in the ex-situ SF is less effective. Comparably, a strong emulsification process was induced in the AF system that dominated the dynamic displacement. Close-ups of Fig. 2-8 in AF system show the numerous small oil globules formed in the pores and entrained in the main flow stream that easily passed through the pore-throat structure. In addition, the in-situ surfactant was more effectively produced at the oil–water interface, thereby promoting additional reduction in the IFT and wettability alteration and a significant increase in the  $Ca$  number. The high  $Ca$  number suggests a dominant viscous-flow regime where the viscous forces were more pronounced. The threshold capillary pressure was further decreased to 0.31–3.1 Pa, which led to substantial enhancement in oil mobilization, particularly in very small pores or corners. During the continuous injection, small oil blobs were re-entrained in the flow stream until equilibrium was reached. An additional final oil recovery of 17.3% was promoted compared with that produced by SF.

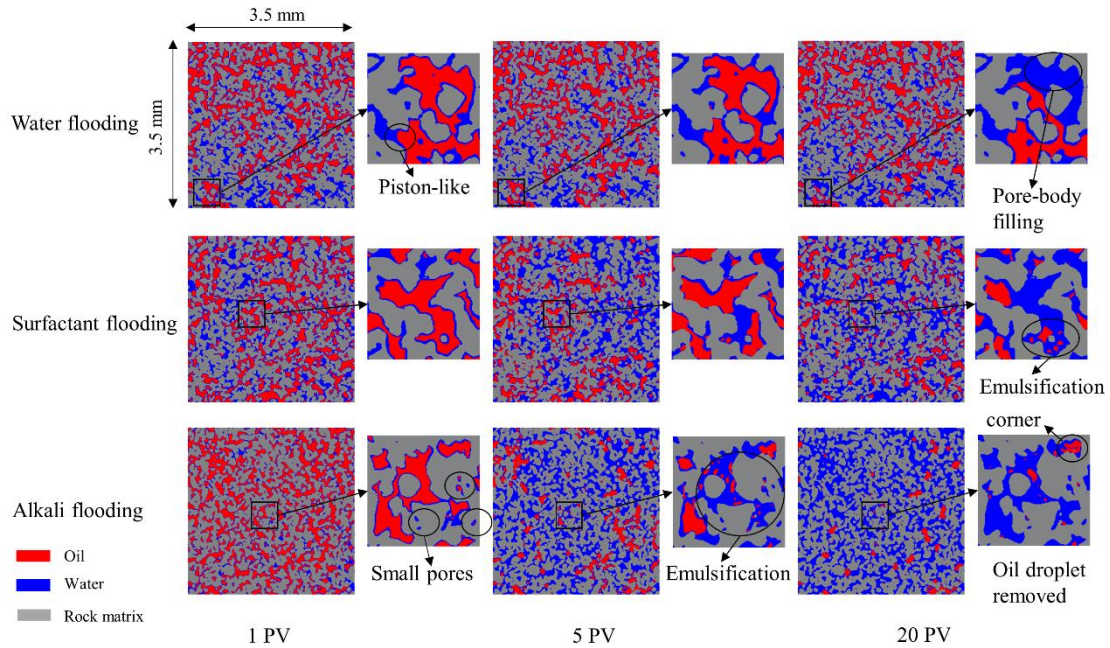


Fig. 2-8. Oil occupancies from 2D cross-sectional view at various injection PV values for WF, SF and AF systems. The  $550 \mu\text{m} \times 550 \mu\text{m}$  magnifications show close-ups of typical oil displacement behavior in pore spaces.

Fig. 2-9 shows 3D visualization of emulsification process from the close-ups of Fig. 2-8 for the SF and AF systems (WF as a reference). Without surfactant participation, no emulsification occurred in the pores, and the oils were removed through piston-like and pore-body filling mechanisms. With ex-situ SF, the emulsification was slight until the injection was increased to 5 PV. Prior to this stage, the oil removal relied on the piston-like and pore-body filling mechanisms; after 5 PV injection of invading fluid, many small oil droplets were formed and were entrained in the main flow stream. However, many oil clusters that were larger than the pore diameter remained in the pores owing to the weak emulsification ability. In contrast, a large fraction of the oil phase area was effectively emulsified into many smaller oil droplets, indicating that the emulsification process during AF was spontaneous and very strong through all injection stages. The quantitative analysis of the oil droplet diameter distributions is presented in Fig. 2-10 and Fig. 2-11. Direct observation of the emulsification phenomenon proves that the in-situ surfactant is more effective than the ex-situ surfactant for emulsion formation and oil recovery performance. A reasonable explanation for the performance differences will be discussed in Section 2.2.4.

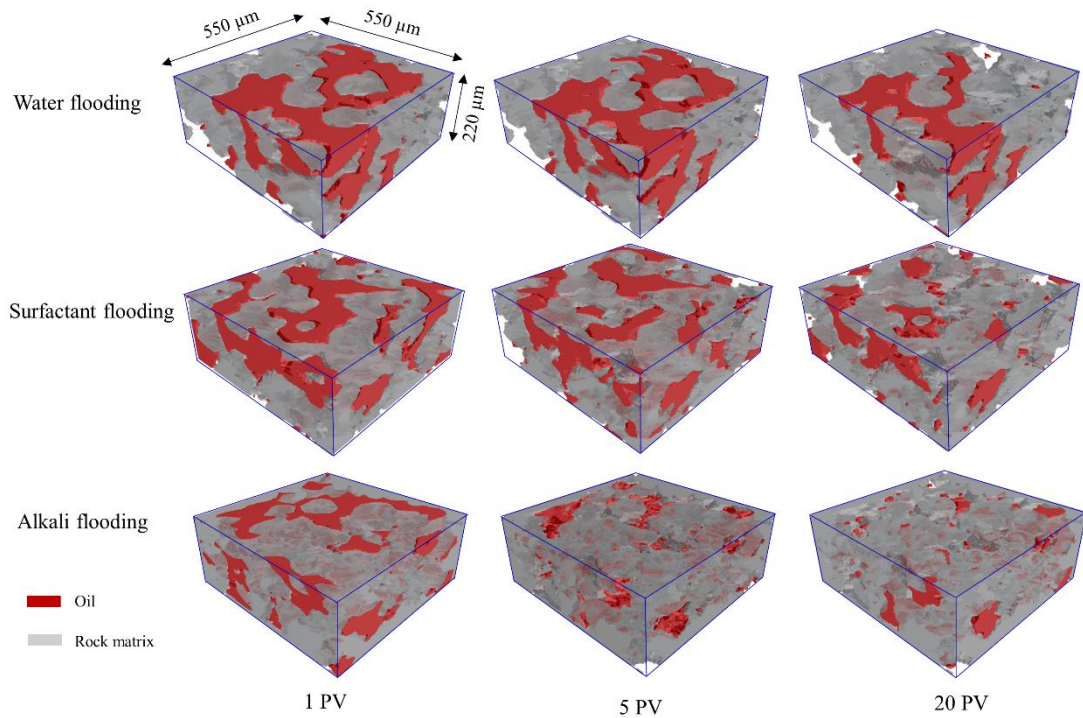


Fig. 2-9. Exemplary three-dimensional (3D) visualization of dynamic oil phase removal in pores at various injection pore volume (PV) values for water, surfactant, and alkali flooding systems. The image group of three systems was reconstructed using the VG Studio Max 2.1 volume rendering software.

### 3) Morphology and topology

As mentioned previously, the size distribution of residual oil clusters is strongly affected by ready-made and chemical-produced surfactants. To quantify the emulsification ability, the count number and volume fraction of oil clusters as a function of equivalent diameter were extracted at the final stage of 20 PV injection, as presented in Fig. 2-10(a)–(b). The equivalent diameter was calculated by Eq. (2-4) [107]. After WF, 19163 small oil clusters were distributed in the equivalent diameter range of 10–50  $\mu\text{m}$ , although only one well-connected cluster was present as a network pattern within 2000–2500  $\mu\text{m}$ . This largest long-chain network accounted for 97.2% of the entire oil cluster volume, which indicates very low oil recovery performance, as shown in Fig. 2-10(c). The highly non-uniform distribution of oil cluster size is attributed to the high-threshold capillary pressure. As a result, once the invading path was established, preferential main flow stream was maintained without invading new pores.

$$D = \sqrt[3]{\frac{6V}{\pi}} \quad (2-4)$$

Where  $D$  is the equivalent diameter,  $V$  is the volume of oil cluster.

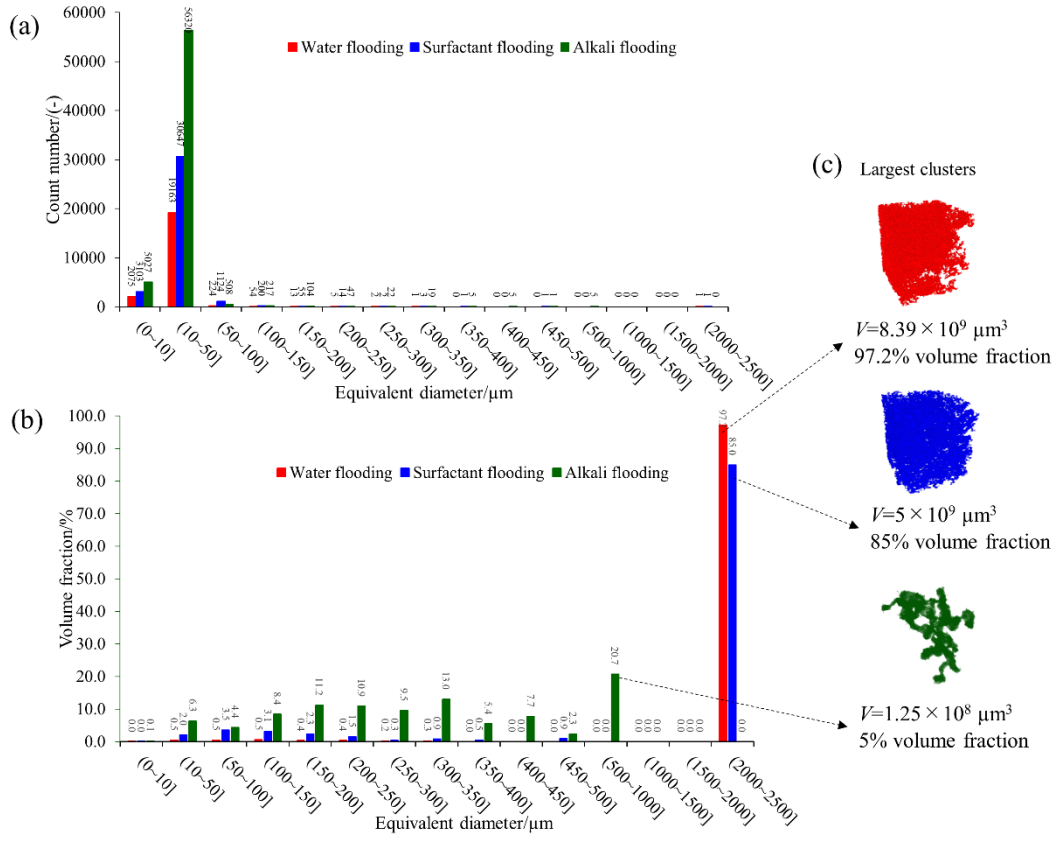


Fig. 2-10. (a) Count number and (b) volume fraction distribution of oil clusters as a function of equivalent diameter. (c) Examples of the largest oil clusters.

With the SF, the number of 10–50  $\mu\text{m}$  counts increased to 30647, which indicates that more small oil droplets were produced from the largest network. Fig. 2-10(c) shows a decrease in the largest cluster size, which accounted for 85% of the entire volume of oil clusters. This implied gradual solubilization of largest oil network leading to emulsification in the pore spaces. The oil recovery was also enhanced by the emulsion entrainment flow. However, a strong emulsification was produced when the core sample was subjected to the AF. Oil size distribution indicates that 10–50  $\mu\text{m}$  oil cluster counts increased to 56320, which is almost twice than that in the ex-situ SF. Furthermore, the volume fraction of the oil cluster presented uniform distribution, as shown in Fig. 2-10(b). That is, the largest network in the WF and SF systems disappeared and emulsified into small oil droplets which spanned pore size from very small to intermediate. The largest cluster accounted for only 5% of the volume fraction to the total oil cluster volume. Fig. 2-11 presents the average equivalent diameter of a single oil droplet extracted randomly from pores in the WF, SF and AF systems. The diameters of the individual oil globules decreased steadily in all systems at values of 93.5  $\mu\text{m}$ , 57.6  $\mu\text{m}$ , and 31.4  $\mu\text{m}$ , in WF, SF, and AF systems, respectively. The smallest diameter of oil droplets in AF system supports again the entrainment flow that the droplets can easily pass through the tortuous pore-throat structure in a smooth-flow mode. Therefore, using the chemical-produced surfactant resulted in the most favorable oil recovery efficiency.

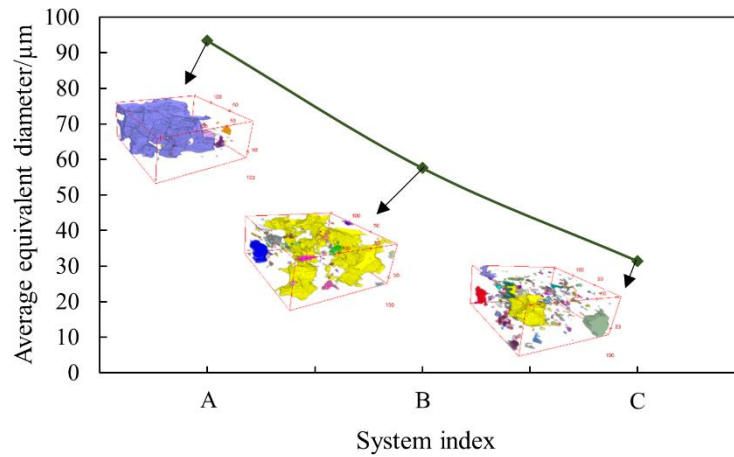


Fig. 2-11. Average equivalent diameters of oil clusters in pore spaces from different systems. The inset images show representative 3D reconstructed oil clusters in pore spaces, where the different colors denote single oil clusters. A, B and C represent water, surfactant and alkali flooding systems, respectively.

The oil clusters were classified into different patterns according to the sphericity ( $G$ ) and Euler characteristics ( $Eu$ ) as expressed in Eq. (2-5) and Eq. (2-6), respectively [123]. As shown in Table 2-3, four main patterns of networks, branches, ganglia, and singlets were classified. Networks are characterized by well-connected shapes spanning vast pores with the largest volume through the porous media. The structure is highly complicated and includes many loop-like structures. Networks generally have very low sphericity owing to the large surface area and negative  $Eu$  characteristics ( $Eu < 0$ ). Branches are small network patterns that occupy several pores with one or more loops. The volumes are relative larger, and  $Eu$  values are negative. Ganglia patterns usually span several pore spaces without loops, and singlets usually occur in the form of sphere-like structures existing within single pores. The volume of singlets is lowest, and the  $G$  approaches 1. The  $Eu$  characteristics of both ganglia and singlet are positive, i.e.,  $Eu > 0$ .

$$G = \frac{\pi^{1/3}(6V)^{2/3}}{A} \quad (2-5)$$

$$Eu = N - L + O \quad (2-6)$$

Wherein  $V$  and  $A$  are the volume and surface area of individual oil clusters, respectively;  $N$  is the number of isolate objects;  $L$  is the number of redundant loops; and  $O$  is the number of cavities [124].

Table 2-3. Classification of oil cluster patterns combining sphericity and Euler characteristics.

Classified patterns	Sphericity ( $G$ )	Euler characteristic ( $Eu$ )
Network	$0 < G \leq 0.1$	$Eu < 0$
Branch	$0.1 < G \leq 0.3$	$Eu < 0$

Ganglia	$0.3 < G \leq 0.5$	$Eu > 0$
Singlet	$0.5 < G \leq 1.0$	$Eu > 0$

The volume fraction of oil cluster patterns against various flooding stages for WF, SF and AF systems is shown in Fig. 2-12. At the early flooding stage of 1 PV, the network pattern was dominant in all systems and contributed 99% of the volume fraction, which indicates good connectivity in the oil phase. When the flooding increased to 5 PV, the network pattern showed a slight decrease of about 10% volume fraction but still dominated in this condition. However, the branches, ganglia, and singlets increased a few percentage points in volume fraction. During this stage, no distinct difference was noted in the volume fraction of oil cluster patterns among these three systems. However, the volume fraction of the different patterns changed significantly when subjected to flooding stage of 10 PV in the AF system. In particular, the network with 78.5% volume fraction disappeared and emulsified into patterns of branches, ganglia, and singlets. Fig. 2-12 clearly shows that the branch patterns increased to 61% of the volume fraction and were the dominant pattern, whereas both the ganglia and singlets increased to 35%. During the flooding stage of 20 PV, ganglia and singlets were formed by branch solubilization. As shown in the figure, the volume fraction of the branches decreased 23%, whereas that of both ganglia and singlets increased almost 10%.

As previously mentioned, this distinctive transformation is attributed to the strong emulsification occurring in the AF.

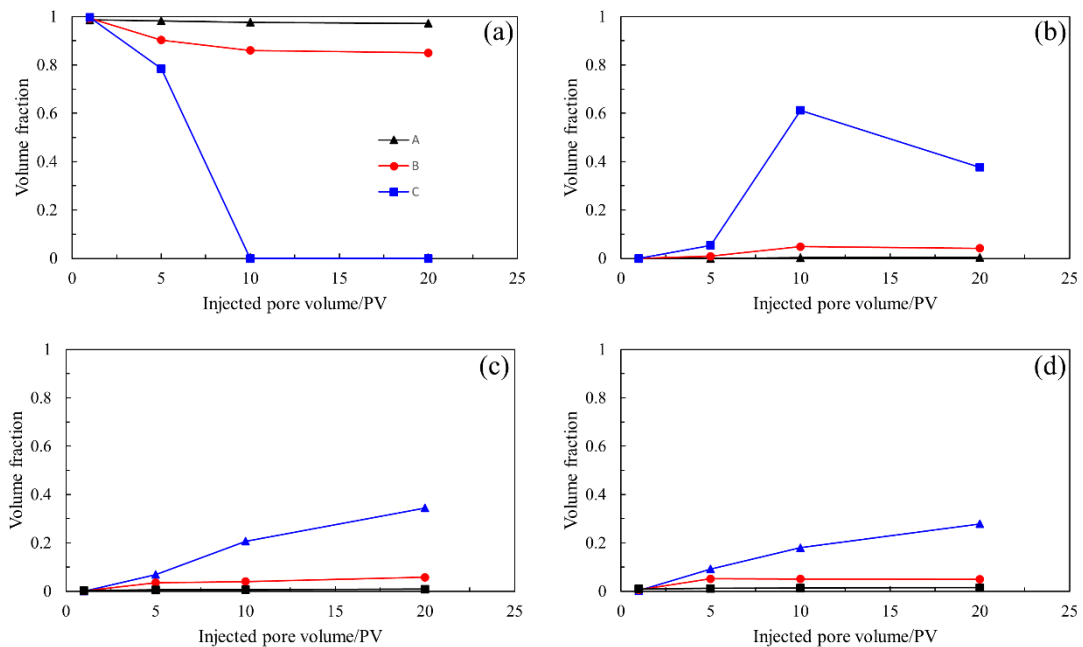


Fig. 2-12. Volume fraction of oil clusters in morphologies of (a) network, (b) branches, (c) ganglia, and (d) singlets as a function of various pore volume (PV) injections for WF (A), SF (B), and AF (C) systems.

A similar variation trend in cluster patterns when the sample was subjected to the SF. However, this change was slight due to the weak emulsification process. For example, the



volume fraction of the network decreased by 4%, whereas a reduction of 78.5% was noted in the AF system. The other patterns of branches, ganglia, and singlets also increased slightly. Nevertheless, the results are still comparable to that of WF system in which once the network was established, only 1% variation was changed for all patterns. The network was the dominant pattern and accounted for 98% of the volume fraction, indicating very low oil recovery efficiency.

#### 2.2.4 Underlying mechanism

As analyzed previously, it can be known that emulsification ability is stronger in the chemical-produced (i.e., in-situ) surfactant than that of in the ready-made (i.e., ex-situ) surfactant. Fig. 2-13 shows the Petri dish tests agrees well with the micro-CT observation. The time-series images indicate no obvious change in the oil phase after 80 s in the ex-situ system. After shaking, many small oil droplets were produced under the mechanical forces. In contrast, spontaneous oil deformation was observed at the oil–water interface after 80 s in the in-situ surfactant system. During the development of oil blebbing over time, some blebs grew large enough to break into smaller droplets. The occurrence of the blebbing phenomenon agrees well with previous research [64,125]. After shaking, most of the oil droplets were very small size. This phenomenon implies that emulsification induced by chemical-produced surfactant was effective and spontaneous, whereas that by ready-made surfactant was weak and required strong shearing force in the porous media.

In the Petri dish test of chemical-produced surfactant system (see Fig. 2-13), the easy fission of oil droplets can be attributed to the a large quantity of surfactant aggregates that is produced effectively at the oil–water interface by chemical reaction [125]. Sumino et al. [64] revealed that these surfactants aggregates has a gel-like structure, which is a type of soft matter. The oil cluster deformed because of inhomogeneous surfactant distribution that resulted in uneven distribution of IFT [63,65] That is, a strong interfacial instability is induced related with IFT gradient and internal pressure inside oil droplets [125]. A similar phenomenon was observed previously in a calcium hydroxide–fatty acid system in which a film of unstable matter formed at the water and oil interface. Within a short time of a few seconds, the film ruptured to enable water entry, which caused the oil droplet to break into smaller droplets [114]. However, the Petri dish test shows there was no oil deformation after aging 80 s, indicating the ready-made surfactant is not effective to reduce the IFT. This reason is that the transport of surfactant molecules to the oil–water interface is a slow process only relying on the diffusion mechanism (no convection).

Fig. 2-14 shows transport mechanisms of ready-made and chemical-produced surfactants in porous-media-flow condition. In the ready-made surfactant system (Fig. 2-14(a)), convection flow is responsible for the surfactant transport to the oil–water interface. In this study, the Péclet number (ratio of convection to diffusion) is estimated within 5~300, indicating the convection dominates over the diffusion [126]. In the other words, the surfactant transport is a slow process because it requires time to deliver the surfactant molecules to interface by convection flow [96,127]. However, in the chemical-produced

surfactant system (Fig. 2-14(b)), the surfactant transport to the interface strongly depends on the quick and precise surfactant production by the chemical reaction. As the large oil clusters are emulsified into many tiny droplets, it increases the contact interfacial area, which results in stronger chemical reaction and the convection flow is also strengthened because of disturbances around the multi-droplets. Consequently, the surfactant transport is much more effective than that of ready-made surfactant injection. Therefore, the surfactant transport mechanisms are very different between the SF and AF systems, which supports that fact that emulsification ability is much stronger in the AF system than that in the SF system.

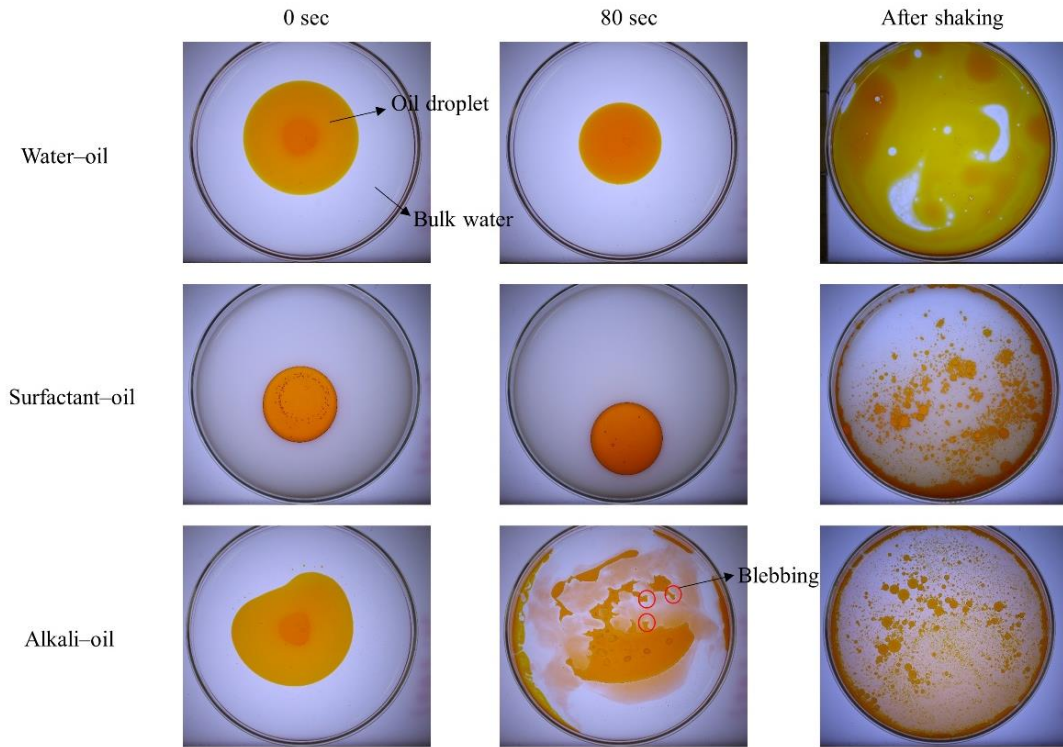


Fig. 2-13. Petri dish experiments of oil drops in the bulk water phase for water, surfactant, and alkali systems.

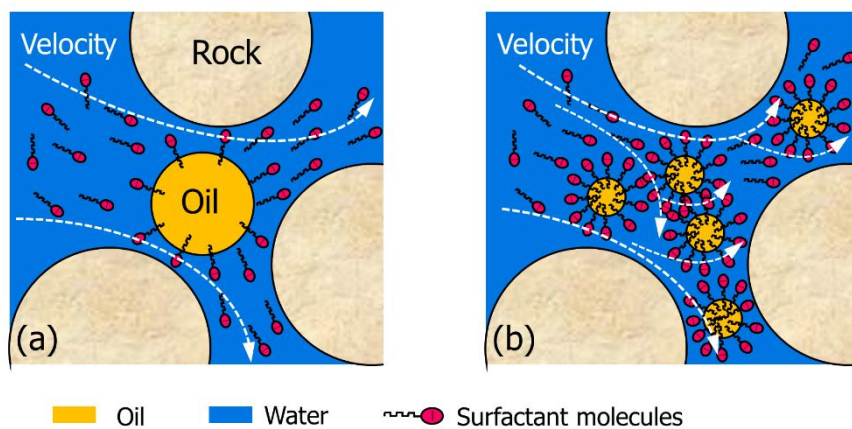


Fig. 2-14. Surfactant molecules transport to the water-oil interface: (a) Ready-made surfactant transport and (b) Chemical-produced surfactant transport.

## 2.3 Extra study for optimization

Section 2.2 revealed that the ready-made surfactant transport to the water–oil interface tends to be slow relying on the convection mechanism (Fig. 2-14(a)). On the contrary, the surfactant produced at the interface by chemical reaction presents comparative rapidity and effectiveness (Fig. 2-14(b)). Therefore, this section will introduce a novel surfactant to optimize the performance of ready-made surfactant which is analogous to the AF. In other words, the new introduced surfactant can adsorb the acid components of oil to form the surfactant aggregates and accumulate quickly near the interface. As a result, the oil deformation was spontaneously induced which shows similar behavior with that AF (see Fig. 2-13). In this sense, the performance of SF can be significantly optimized which approaches that of AF. Note that the adsorption is a physical process instead of a chemical reaction.

### 2.3.1 Chemicals and fluids

The oil phase was prepared by mixing 25% v/v tetradecane (FUJIFILM Wako Chemicals Co., Ltd) and 75% v/v JS 1000 standard oil (Nippon Grease Co. Ltd.). The standard oil was used to increase the viscosity of the oil mixture due to its high viscosity of ~1000 mPa·s (20°C). We dissolved 20 mmol/L palmitic acid (PA) (FUJIFILM Wako Chemicals Co., Ltd) into the oil sample to imitate the natural acidic heavy oil, which corresponds to a total acid number of 1.35 mg KOH/g. The chemical aqueous phase was prepared by dissolving 20 mmol/L stearyltrimethylammonium chloride (STAC, a type of cationic surfactant) (Tokyo Chemical Industry Co., Ltd) into the de-ionized water (TRUSCO Nakayama Corporation). The experiments included water flooding (WF) and chemical flooding (SF) systems, which indicates oil phase was displaced by the pure water phase and STAC aqueous phase, respectively. Note that pure WF was only a reference to compare with the performance of SF. The test fluids and physical properties are listed in Table 2-4. To aid visualization, a certain concentration of Sudan red or iododecane was doped during camera snapshotting and X-ray micro-CT scanning, respectively.

Table 2-4. Test fluids and properties in the WF and CF systems.

System	Oil phase	Aqueous phase
Water flooding (WF)	Oil + PA 20 mmol/L	De-ionized water
	Viscosity: 85.1 mPa·s	Viscosity: 0.890 mPa·s
	Density: 0.830 g/mL	Density: 0.997 g/mL
Surfactant flooding (SF)	Oil + PA 20 mmol/L	Water + STAC 20 mmol/L
	Viscosity: 85.1 mPa·s	Viscosity: 1.18 mPa·s
	Density: 0.830 g/mL	Density: 0.975 g/mL

Note: PA represents palmitic acid, and STAC is stearyltrimethylammonium chloride.

### 2.3.2 Experimental method

The spontaneous oil deformation was first observed in a static mode using a Petri dish test.

Afterwards, the performance and displacement mechanism were evaluated by two tests of 2D microchannel and 3D porous media. The schematic diagrams of two tests are shown in Fig. 2-15.

1) Petri dish test

In this test, an oil droplet containing PA was statically placed in the aqueous phase with the STAC surfactant. As the time progressed, the shape of oil droplet was monitored using a digital camera (EOS R6; Canon, Japan).

2) Microchannel test (2D)

A microchannel (45 mm × 10 mm) was fabricated using a stereolithography three-dimensional (3D) printer (Form 3+, Formlabs Inc., USA), as shown in Fig. 2-15(a). A large channel and a constricted channel were printed inside the microchip. The accuracy of the 3D printer has been evaluated in our previous study [128]. The radius of the large channel was 1500 μm. The length and radius of the constricted channel were 5 mm and 150 μm, respectively. The large and constricted channels were used to imitate a group of pore-throat structures in an actual rock sample, thereby allowing oil displacement to be observed directly from a pore-scale view. First, the microchannel was saturated with pure water. Next, oil was injected to remove water. Subsequently, an aqueous phase was injected to displace the oil in the channel. A syringe pump (KDS 200, KD Scientific Inc., USA) was used to control the flow rate to 1, 10, and 50 μL/min. The dynamic displacement process was captured using a digital camera (EOS R6; Canon, Japan).

3) Porous media test (3D)

A pore-scale test (see Fig. 2-15(b)) was performed to observe oil deformation phenomenon in the 3D porous media. The pore space was more tortuous and complicated than that in a single pore-throat structure (Fig. 2-15(a)). Glass beads with a diameter of 1000 μm were used as the porous media. This particle size yielded large pore-throat spaces, which allowed us to observe the oil deformation more clearly. First, the glass beads were packed densely into an acrylic container with a 10-mm inner diameter and 30-mm height. In this step, the image-based porosity was measured to be ~0.41 via X-ray CT scanning (ScanXmate-RB090SS, Comscantechno Co., Ltd., Japan). Afterwards, the sample was transferred to a vacuum chamber, where it was fully saturated with DI water. Subsequently, the oil phase was injected to create connate water conditions. Finally, 0.5 pore volume (PV) of STAC solution was injected to displace the oil phase at a flow rate of 500 μL/min. In this step, the injection was stopped, and oil deformation automatically occurred in the pore spaces. Residual oil deformation was monitored via X-ray CT scanning at different periods (0–60 min, 5 min intervals). The resolution of the X-ray CT was set to 16.553 μm/pixel, which implies that the FOV encompassed the entire sample with a diameter of 10 mm and a height of 15 mm. More details regarding the X-ray CT performed are available in our previous publication [113].

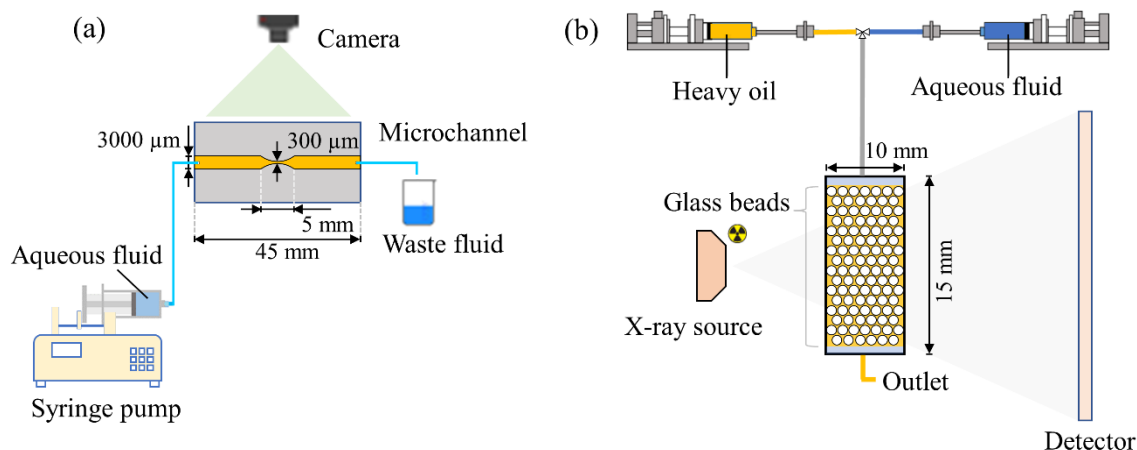


Fig. 2-15. Schematic diagram of experiments: (a) 2D microchannel and (b) 3D porous media.

### 2.3.3 Image processing

In this study, all image-based data were obtained via camera snapshotting and X-ray CT scanning. Therefore, all quantitative information (including area, perimeter, volume, and saturation) was extracted from the images using the ImageJ software platform (National Institutes of Health). Details regarding the image-processing workflow are presented in [Appendix A-A.1 Image processing](#).

### 2.3.4 Results and discussion

The oil droplet deformation in the chemical aqueous phase has been observed in the Petri dish. Three stages of shrinking, spreading, and blebbing were also confirmed in the previous research [64,129]. In this study, we successfully reproduced their experiments, and some novel phenomena were revealed as shown in Fig. 2-16. In Fig. 2-16(a), there were three distinct stages of deformation when the oil droplet was placed on the water phase. The oil droplet first shrank and then spread to a larger diameter within a few seconds. Subsequently, the oil droplet shape became deformed, undergoing a blebbing stage. The shrinking–spreading–blebbing stages were consistent with that reported by Sumino et al. [64]. When we dropped a smaller oil globule in the water phase, oil blebbing occurred and, at the same time, splitting along the deformed surface started spontaneously (see in Fig. 2-16(b)). We found that if increased the oil droplet size to four times larger than that in Fig. 2-16(b), the droplet spread to critical size and then activated a drastic crushing to pieces (Fig. 2-16(c)). This phenomenon is also called an amoeboid movement in alignment with previous observation [129]. Apart from the droplet size, the depth of water in the Petri dish also played a significant role in the deformation phenomenon. Fig. 2-16(d) shows the oil droplet first spread and then shrank to a smaller size instead of crushing stage. In Fig. 2-16, we can see that the oil deformations show similar behavior with that of AF in Fig. 2-13.

Fig. 2-16(e) illustrates the schematics of molecular aspects of aggregate formation. Initially, STAC in the aqueous phase forms spherical micelles, whereas PA in the oil phase exists as monomers (stage 1). The PA cannot penetrate the aqueous phase without the

presence of STAC. When the aqueous phase contacts with the oil phase, the PA molecules will penetrate the aqueous phase and adsorb into the STAC micelles (stage 2). Once the PA molecular aggregate is enough, the STAC micelles elongate to form several bilayers close to the water-oil interface (stage 3). This bilayer was also called lamellar structure with a thickness of about 40 nm, proved by Sumino et al. [63]. The intensive deformations of oil droplets were attributed to the heterogeneous distribution of surfactant aggregates, leading to an inhomogeneous IFT distribution [64]. In turn, a convective flow in the aqueous phase was induced due to the Marangoni effect [129]. Furthermore, the oil droplet size and depth of the aqueous phase affected the intensity of convective flow. Therefore, the oil deformations presented different stage behaviors (see Fig. 2-16(a)–(d)). Given that the crude oil contains the PA molecules, the oil cluster will also deform and split in the porous media when subjected to the STAC flooding. In other words, the Petri dish experiments imply that the new STAC surfactant is analogous to the AF, which can also accelerate the surfactant aggregates to the water–oil interface in a method of physical adsorption.

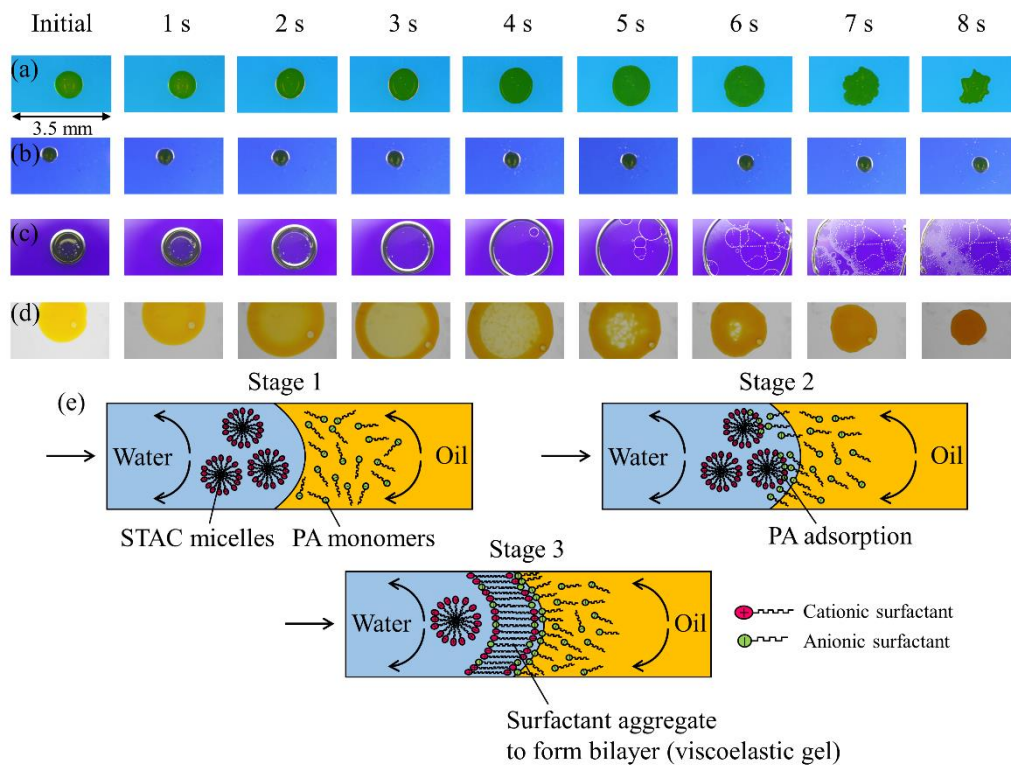


Fig. 2-16. Time-series snapshots of an oil droplet on the aqueous solution in a Petri dish test. Four main types of deformation were observed: (a) shrinking–spreading–blebbing, (b) blebbing–splitting (c) spreading–crushing and (d) spreading–shrinking.

The microchannel test simulated the oil displacement process in a single pore-throat structure. Fig. 2-17 shows the oil blebbing phenomenon in the static mode and its effect on the frequent change of flow path direction in the dynamic mode. As shown in Fig. 2-17(a), the oil shape is monitored immediately after the injection is terminated. The oil shape changed repeatedly, indicating that the oil clusters underwent continuous interfacial blebbing. This result is consistent with a previous report pertaining to Petri dish experiments by

Sumino et al. [64,125]. They reported that oil blebbing is ascribed to an unstable internal oil pressure resulting from the inhomogeneous distribution of surfactant aggregates. In the dynamic mode (Fig. 2-17(b)), the flow path direction is diverted by the frequent change in the oil shape, which implies that the STAC solution can contact more oil phase in pore spaces, especially in the dead pores and corners. Fig. 2-17(c) shows quantitative information based on the deformation number (see Eq. (A-A1) in Appendix A-A.1) for comparing the changed oil shapes in the static and dynamic modes. Initially, the deformation numbers are similar, which indicates that the oil shapes are similar. As time progresses, the difference between the static and dynamic modes increases. The oil shape in the dynamic mode is elongated during the shearing force, whereas that is reduces to a clump in the static mode. This implies that the perimeter in the dynamic mode should exceed that in the static mode. Finally, the deformation number indicates a significant difference. The deformation number again supports that flow path was changed frequently which could displace more oil in pore spaces. Additionally, Fig. 2-17(b) shows oil splitting was produced under the shearing forces in the dynamic displacement process, indicating emulsification occurred spontaneously even without interactions with porous media. Fig. A-A3 shows that flow patterns were also affected by the flow rates (see Appendix A-A.2). With increasing flow rate, the emulsification became more intensive which enable the tiny oil droplets easily pass through the pore spaces. Therefore, it is supposed that emulsification ability of STAC surfactant is improved which is better than the previous sodium linoleate surfactant. As a reference to Fig. A-A3, the pure water flooding in Fig. A-A4 shows there is no oil deformation in the microchannel flow.

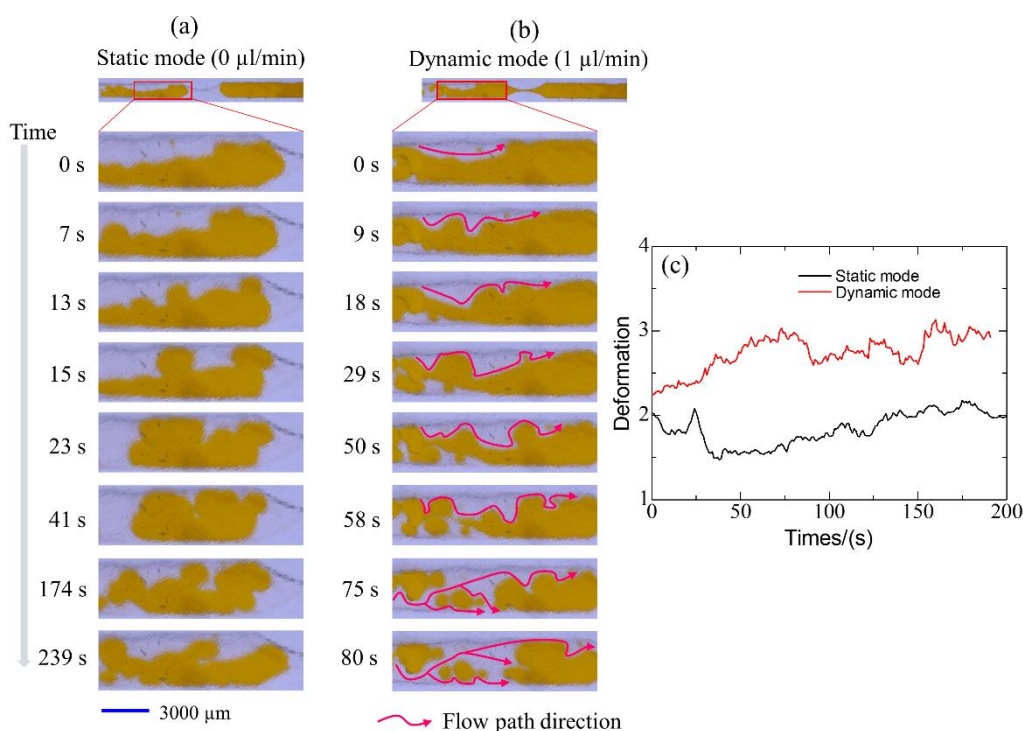


Fig. 2-17. Comparison of oil deformations between static mode (a) and dynamic mode (b) in

microchannel. Deformation number (c) is quantitatively extracted from time-series images. Near water–oil interface, STAC micelles adsorb PA monomers, generating bilayers (d) that exhibit viscoelastic and fragile properties.

Fig. 2-18 shows the oil deformation phenomenon in the multi-pore-throat structures in the 3D porous media. As shown in this figure, oil deformation is strong in the well-connected pore spaces, and some novel phenomena are discovered through this test. Fig. 2-18(a) shows the oil deformations in the 2D cross-sectional area. Numbers 2 and 5 represent the shrinking stage of the oil cluster, and number 6 indicates the spreading stage. This finding is consistent with those from Petri dish tests [64,125,129] and that from the single pore-throat test (see Fig. 2-17(a)). In the multi-pore-throat structures, the oil film attached to the solid particle surface and connected the adjacent particles as bridges. Once oil deformation occurred, the oil film detached from the surface and appeared in the main oil clusters, as shown in number 3. This implies that film detachment can strengthen oil remobilization and improve oil recovery. In addition, many bridges were disconnected, as indicated by numbers 1 and 4. As shown in Fig. 2-18(a), small new oil droplets appeared in the pore space, which implies the occurrence of spontaneous emulsification due to splitting. Fig. 2-18(b) shows 3D close-up images of oil deformation from numbers 2, 4, and 6. As shown in this figure, oil shrinkage reduced the oil cluster volume (number 2). In number 4, the bridge was disconnected, and some oil clusters snapped off automatically, even without the participation of shearing forces. At number 6, oil shrinking widened the oil cluster, which was ascribed to the pull-back self-movement. Meanwhile, the appearance of new oil droplets indicated the occurrence of spontaneous emulsification.

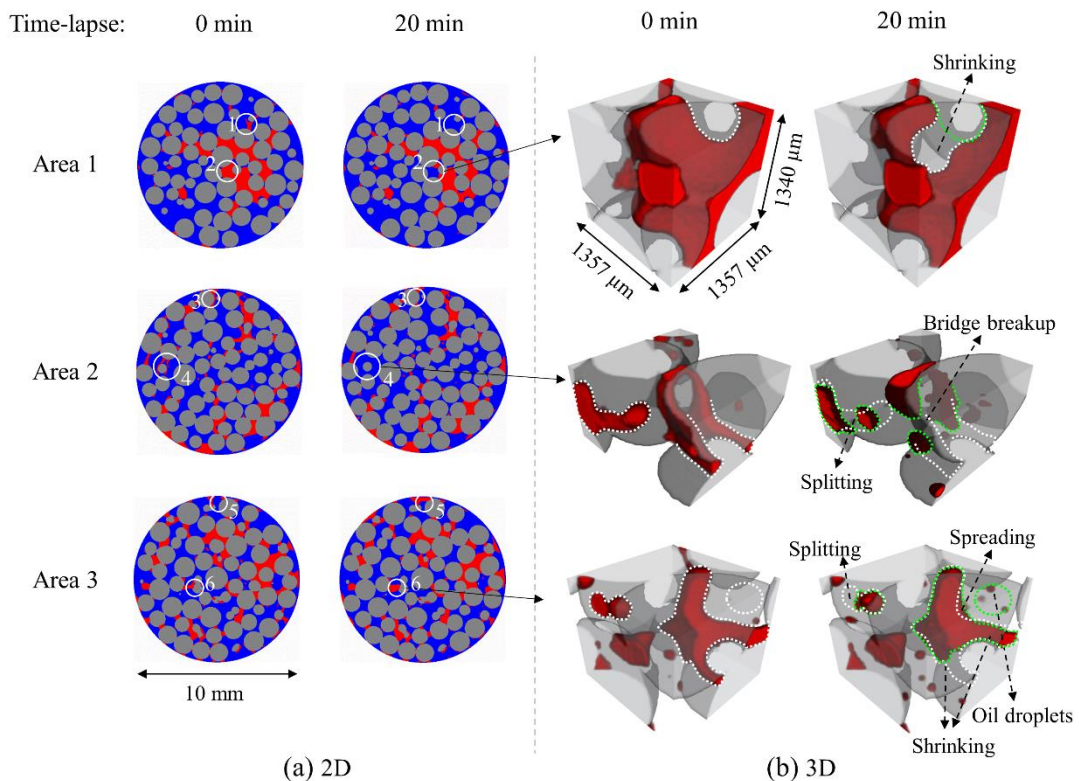




Fig. 2-18. Examples of oil deformation phenomenon captured via X-ray CT scanning in pore-scale flooding experiment. Left images (a) show oil deformations in three groups of cross-sectional area after aging for 20 min (numbers 1–6 indicate oil shape changes between 0 and 20 min). Right images (b) show 3D close-up views of oil deformation from numbers 2, 4, and 6.

The oil deformations were summarized as disappeared and newly appeared oil phases. Disappeared oil implies the disappearance of some oil, which consequently reduced the oil cluster volume. Some examples include oil shrinking, film detachment, and bridge disconnection. Newly appeared oil implies the reappearance of some oil, e.g., oil spreading, which results in a larger volume and emulsification.

The qualitative and quantitative information of the disappeared and newly appearing oil is shown in Fig. 2-19. As shown, both the disappeared (Fig. 2-19(a)) and newly appeared (Fig. 2-19(b)) oils were intensive in the pore space. As time progressed (0–60 min), the volumes of both oils increased. Fig. 2-19(c) shows the volume ratio of the disappeared or newly appearing oil volume to the initial oil-trapped volume. This figure shows that the oil deformation is the most intense prior to 10 min and weakens thereafter. Therefore, the status of the most intense oil deformation at 10 min was selected for the subsequent morphology analysis. Sphericity and the Euler number were used to classify the oil shapes into different patterns. The details are available in our previous publications [18,113]. Based on the different patterns, we discovered that only ganglia and singlets coexisted in the deformed oil shape, as shown in Fig. 2-19(d). The ganglia show that the deformed oil occupied several pores and throats, which resulted in a more complicated structure. Meanwhile, the singlets show the simplest configuration and represented the deformed oil within a single pore and throat. As presented in Fig. 2-19(d), the volume fractions of the ganglia and singlets were almost equal in the disappeared oil, whereas those of the singlets was more than five times larger than those of ganglia in the newly appeared oil. In other words, the singlets dominated the newly appearing oil, which implies that spontaneous emulsification dominated over spreading. The equal fractions of ganglia and singlets in the disappeared oil indicate that bridge disconnection and shrinking contributed equally to the volume change.

In summary, microchannel tests show the flow path of the aqueous phase was frequently diverted because of the constant oil shape change, which enabled the STAC solution to be in contact with more oil in the pore spaces, particularly in the stagnant region. In addition, spontaneous emulsification was induced under shearing forces. Porous media test shows the oil deformations, i.e., oil spreading, shrinking, film detachment, and bridge disconnection, were the strongest after 10 min of aging. Combined the results of microchannel and porous media tests, we recommend a new injection–alternate–stop scenario for oil recovery applications. The flow rate should be controlled as low as possible, ensuring the domination of diverted flow path. The stop interval was set to 10 min, considering the most intense oil deformation. Therefore, it is supposed that the new scenario can significantly enhance the oil recovery. The new introduced STAC surfactant shows better performance than previous sodium linoleate surfactant.

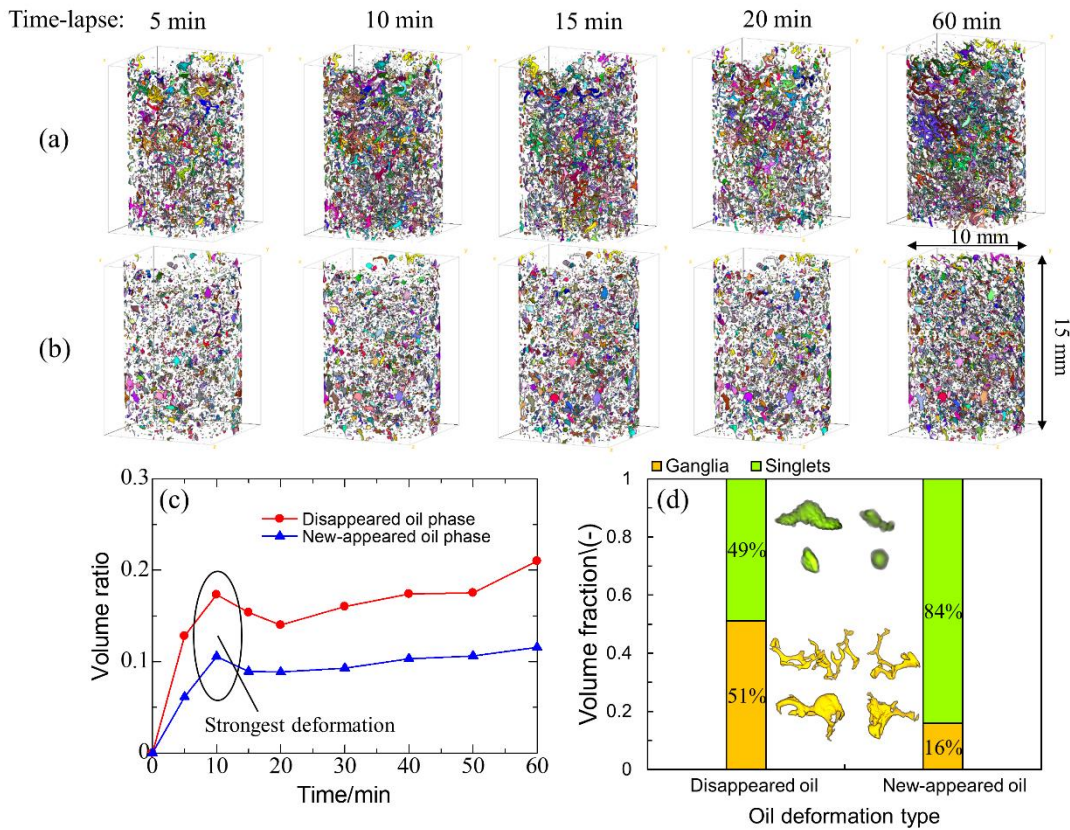


Fig. 2-19. Three-dimensional visualization of disappeared oil (a) and newly appeared oil (b) as a function of time (0–60 min) in pore spaces of entire sample and their quantitative information, i.e., volume ratio (c) and volume fraction (d). Field of view is 10 mm in diameter and 15 mm in height. Volume ratio represents ratio of deformed oil volume (disappeared/newly appeared oil volume) to initial oil-trapped volume. Volume fraction in (d) is calculated based on time at which deformation is the most intense (i.e., 10 min) in (c), which represents ratio of ganglia/singlet volume to deformed oil volume. Inset shows several examples of ganglia and singlets from the most intense oil deformation.

## 2.4 Summary

In this chapter, the surfactants prepared in ready-made and chemical-produced manners for oil recovery were examined through a series of miniature core-flooding tests. The noninvasive technique, X-ray CT, enabled us to investigate the oil configuration in 3D pore spaces from a pore-scale view. The surfactant efficiency was evaluated by the factors of the IFT, wettability, emulsion stability, emulsion sizes and oil cluster patterns in porous media. Possible mechanisms were proposed for the different surfactant systems. In the extra study, we introduced a novel STAC surfactant to optimize the performance of ready-made surfactant and revealed its novel mechanism. Several important conclusions were drawn as follows:

(1) The final oil recovery was highest in the AF system, whereas that of SF was intermediate, corresponding to the efficiencies of 86.9% and 69.6%, respectively. The performances of surfactants prepared by ready-made and chemical-produced manners are

different. The chemical-produced surfactant in AF is more effective than that of ready-made surfactant in the IFT, wettability alteration and emulsification. Strong emulsification dominated in the oil displacement that produced tiny oil droplets when subjected to the AF. The average equivalent diameter of the oil droplets changed from 57.6  $\mu\text{m}$  to 31.4  $\mu\text{m}$  in the ex-situ and in-situ cases, respectively, which led to effective emulsion-entrainment flow in the mainstream. Additionally, the threshold capillary pressure was decreased from 87.6 Pa to 0.31–3.1 Pa because of IFT reduction and wettability alteration, which enhanced the mobilization of oil clusters from the pore spaces.

(2) The morphology analysis shows that the residual oil of AF system included only separate small oil ganglia and singlets, whereas that of SF system was dominated by the large well-connected networks (accounting for 85% of total volume). This indicated a transformation occurred that the networks and branches in the SF system were gradually emulsified into ganglia and singlets in the AF system.

(3) The surfactant transport mechanisms are different between the SF and AF systems. For the ready-made surfactant system, surfactant molecules transport to the oil–water interface is triggered by the convection, which requires time and is a slow process. By contrast, for the chemical-produced surfactant system, the surfactant transport to the interface depends strongly on the quick and precise surfactant production by the chemical reaction. The large oil clusters are emulsified into many tiny droplets, which increase more contact interfacial area and trigger stronger chemical reaction. Furthermore, the convection flow is also strengthened because of disturbances around the multi-droplets. Consequently, the surfactant transport is much more effective than that of ready-made surfactant injection. Therefore, the surfactant transport mechanisms are very different between the SF and AF systems, which supports that fact that emulsification ability is much stronger in the AF system than that in the SF system.

(4) The novel introduced surfactant could accelerate the surfactant aggregates to the water–oil interface by a method of physical adsorption, which is quicker than that of convective transport. The oil deformation and emulsification are spontaneous and intensive which is analogous to that of AF. Therefore, the performance of ex-situ surfactant is optimized using a novel surfactant, which provides an important reference to the industrial-scale design of acid oil recovery.

### 3 Effect of oil-acid concentration on performance of alkaline flooding application

**Objective:** Chapter 2 proves the alkaline flooding is the best choice for the acid oil recovery. But the performances of alkaline flooding applied for different acid oil reservoirs are still unknown. In this chapter, the effect of oil acid concentrations on the performance of alkaline flooding will be investigated. The performances will be evaluated from aspects of interfacial tension, oil displacement front, emulsification ability, and oil recovery efficiency. From a pore-scale view, the oil movement behavior will be visualized to reveal the underlying mechanisms. The industrial application scenario will be optimized when alkaline flooding is used as the chemical agent for various acid oil reservoirs.

#### 3.1 Experimental section

##### 3.1.1 Materials and fluids

The paraffin oil (Wako 1st grade, FUJIFILM, Japan) was used to simulate the actual heavy oil phase in subsurface. The different concentrations (0, 2 and 200 mM) of linoleic acid (Wako 1st grade, FUJIFILM, Japan) were added into the oil phase, which represent different amounts of acid components that contain in natural heavy oil. In this experiment, we made three types of acidic oil with total acid number (TAN) of 0, 0.135, and 13.5 mg KOH/g, which corresponds to non-acid system (NAS), low-acid system (LAS), and high-acid system (HAS). The aqueous phase was injected to displace the heavy oil phase and oil recovery can be obtained from the outlet. The aqueous phase was prepared by dissolving 100 mM sodium hydroxide (NaOH) into the deionized (DI) water (Trusco Nakayama Corporation) to imitate the alkaline flooding solution. The pure DI water injection was a reference to examine the performance of alkaline flooding. For a visualization purpose, 10% wt. sodium iodide (NaI) (Kanto Chemical Co., Inc., Japan) was doped in the aqueous phase. As a result, the oil and water phases can be differentiated using an X-ray CT scanning. The fluid viscosity was measured using a viscometer (Sine-wave Vibro Viscometer-SV 10, Japan), and the interfacial tension (IFT) was acquired using a tensiometer (Drop Shape Analyzer-DSA 25, Germany). The fluids and their properties are listed in [Table 3-1](#).

Table 3-1. The properties of injected and displaced fluids in core-flooding experiments under room conditions.

Labels	Heavy oil phase	Aqueous phase
Non-acid system (NAS)	Pure paraffin oil (TAN = 0 mg KOH/g)	DI water + 10 %wt. NaI
Low-acid system (LAS)	Paraffin oil + 2 mM linoleic acid (TAN= 0.135 mg KOH/g)	DI water + 100 mM NaOH + 10 %wt. NaI
High-acid system (HAS)	Paraffin oil + 200 mM linoleic acid (TAN = 13.5 mg KOH/g)	DI water + 100 mM NaOH + 10 %wt. NaI

$\rho$ (kg/m <sup>3</sup> )	837	1070
$\mu$ (mPa·s)	89	1.25
$\gamma_{wo}$ (mN/m) in NAS	42.5	—
$\gamma_{wo}$ (mN/m) in LAS	2.0	—
$\gamma_{ow}$ (mN/m) in HAS	< 1	—

\* $\rho$  and  $\mu$  represent the density and viscosity of fluids.

\* $\gamma_{wo}$  represents the interfacial tension between the water and oil phases.

### 3.1.2 Experiments and procedures

In this work, two main experiments including 3D core flooding and 2D micromodel and a preliminary test in Petri dish were conducted. Initially, the chemical water-oil mixtures were observed using a microscope in a Petri dish. The core flooding aimed to obtain the oil recovery performance by alkaline flooding from a macro-scale view. After that, the displacement mechanisms were obtained in the micromodel tests from a pores-scale view. All tests were conducted in ambient pressure and temperature condition.

#### 1) Petri dish tests

In Petri dish tests, the aqueous and heavy oil phases (water-oil ratio = 1:1) are firstly mixed and stirred in a beaker using a homogenizer. The stirred speed and duration were controlled at 1000 rpm and 60 min, respectively. After that, the mixture was transferred in a Peri dish and observed under a microscope ((YDU-3S, Japan)).

#### 2) Core-flooding tests (3D)

The experimental diagram of core-flooding tests in 3D porous media are shown in [Fig. 3-1\(a\)](#). The oil reservoir was imitated by unconsolidated plastic particles (250–425  $\mu\text{m}$ , XH series, Ube Sand Engineering Co., Ltd.) as the porous media in a column container with an inner diameter of a 32 mm and a height of 90 mm. The porosity and permeability of porous media were measured to be  $\sim 0.53$  and  $\sim 1.60 \times 10^{-11} \text{ m}^2$ , respectively. The average pore and throat diameters were 127.53  $\mu\text{m}$  and 39.40  $\mu\text{m}$ , respectively [130]. A glass filter was mounted near the outlet to maintain the uniform flow and prevent particles blocking the outlet. A syringe pump (KDS200, KD Scientific Inc., USA) was used to control the flow rate of aqueous phase injection. The displaced heavy oil was collected from the outlet and oil recovery efficiency was obtained through the analysis of effluent composition. During each injection, the oil displacement processes were visualized using an X-ray CT scanner (Comscantechno, ScanXmate-RB090SS). The imagery data was obtained based on the X-ray tomograms, which contains total of 992 slices; each slice covers the area of  $992 \times 992 \text{ pixel}^2$  ([Fig. 3-1\(b\)](#)).

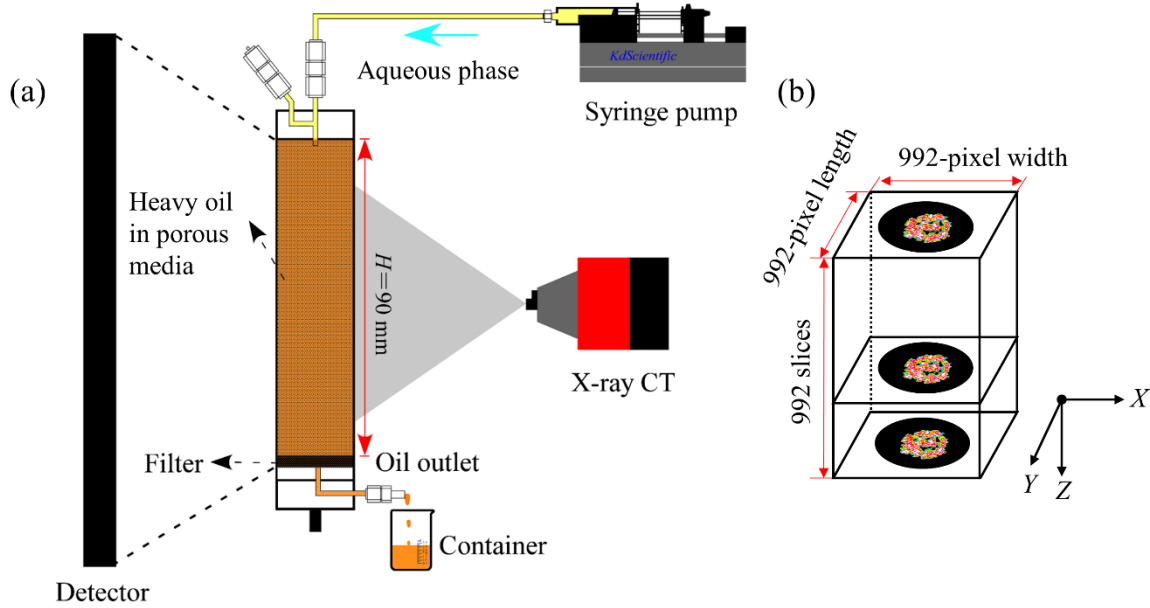


Fig. 3-1. Sketch of the (a) core-flooding experiment and the (b) scanned X-ray CT image structure. The porous media was initially saturated with 100% heavy oil; thus, the oil phase was displaced by the aqueous phase. The displaced oil was collected from the outlet. The X-ray CT was used to capture the displacement patterns during the flooding processes. The scanned CT images contained  $992 \times 992 \times 992$  voxels along the axial directions of X, Y, and Z, respectively.

The experiments were mainly conducted by employing four consecutive processes. First, we filled the constant weight (63.4 mg) of the plastic particle in the column container. The same weight can keep equivalent porosity and permeability in each test. Subsequently, the porous media was fully saturated with heavy oil phase using a vacuum chamber. The pore volume (PV) was obtained to be 37~39 mL according to the mass change before and after full saturation. Next, the core sample was vertically placed on a horizontal tray between the X-ray resource and the detector (Varian, PaxScan 1313DX). After that, the aqueous phase was injected downward to displace the oil phase at a flow rate of  $q = 24\text{--}480$  mL/h. Meanwhile, the oil production was collected by a mini container from the outlet. The total injected volume reached 2 PV with an interval of 0.1 PV. After each interval injection, the oil displacement pattern was captured by one-time X-ray CT scanning. The resolution was set to be  $103 \mu\text{m}/\text{pixel}$  by adjusting the distance to the X-ray source, which is enough to obtain the high-resolution images. The voltage 80 kV and current of  $80 \mu\text{A}$  was set to control X-ray emission intensity. During each scan, the core sample rotated itself clockwise by  $360^\circ$  within almost 124 s (i.e., 8 frames/s) and 992 image slices were acquired from the XY, XZ, and YZ planes (i.e.,  $992 \times 992 \times 992$  voxels).

The open-source ImageJ software (National Institutes of Health, USA) was used to process the X-ray CT raw images. The workflow of image processing mainly includes five steps. (1) Rough crop: only circular area of porous media was retained by crop function which removed other unnecessary image parts; (2) Brightness adjustment: the gray value of each image slice was adjusted by referring to that of surrounding air, which was considered

unchanged during each scanning; (3) Image subtraction: only aqueous phase was obtained using the images of aqueous flooding subtracting that of full oil saturation. By this step, the displacement patterns can be extracted; (4) Noise removal: the noise in step (3) was removed by user-defined codes; (5) Calibration: the aqueous saturation was correlated with gray values by the calibration function (see Ref. [131] for details).

### 3) Micromodel tests (2D)

Micromodel tests were conducted to verify the mechanism of alkaline flooding for improving oil recovery. The microfluidic chip (Micronit Microtechnologies, Netherlands) is a good simulator for real pore-throat structure in sandstone, which was made of two thin glass plates with an etched channel in one of the plates. The micromodel diagram is shown in Fig. 3-2. The porosity of this chip was 0.57 and the average size of pore spaces was 130  $\mu\text{m}$ , which both resemble that of the 3D core sample. The detailed information about the micromodel is provided in Table 3-2. During the tests, the micromodel was horizontally laid under a color camera (Canon 60D, Japan), and the dynamic oil displacement process was videotaped. The injection flow rate was controlled using a syringe pump (KDS200, KD Scientific Inc., USA). The oil displacement mechanisms were analyzed based on image processing using the ImageJ software.

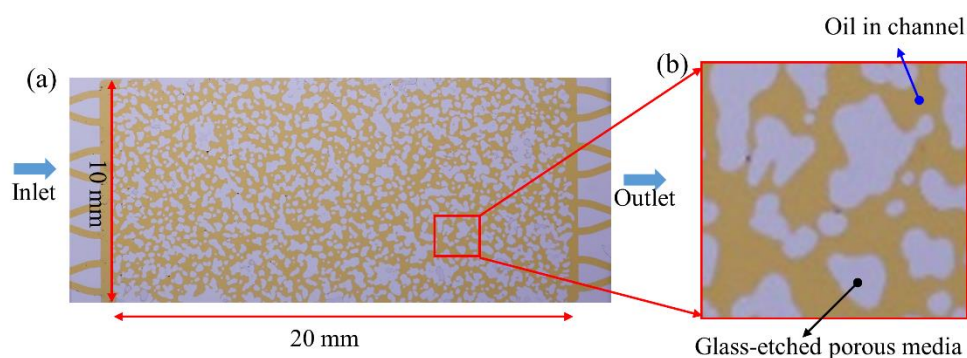


Fig. 3-2. Micromodel diagram: (a) Pore spaces saturated with heavy oil dyed with Sudan red and (b) Magnification of the pore spaces in local area.

Table 3-2. Properties of the glass-etched porous media in the micromodel

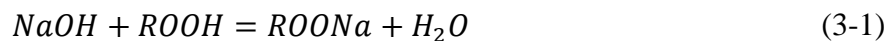
Micromodel properties	Values
Chip size	20 mm $\times$ 10 mm
Porosity	0.57
Permeability	$2.47 \times 10^{-12} \text{ m}^2$
Pore volume	2.3 $\mu\text{L}$
Channel depth	20 $\mu\text{m}$
Average pore size	130 $\mu\text{m}$

The fluids used in the micromodel tests were prepared in a similar manner to that in the 3D experiments. For visualization purpose, the heavy oil was colored using 0.5 % wt. concentration of Sudan red to differentiate the oil and aqueous phases. The micromodel tests were carried out as the following steps: (1) The micromodel was evacuated using pure carbon dioxide (CO<sub>2</sub>); (2) De-gas water was injected to displace CO<sub>2</sub> at a flow rate of 100 μL/min for an hour (CO<sub>2</sub> gas was completely dissolved in this step); (3) Heavy oil was injected to remove the water and fully saturate the pore spaces at a flow rate of 100 μL/min; (4) The oil phase was displaced by the aqueous phase at flow rate of 1 μL/min, 10 μL/min, and 50 μL/min; (5) The dynamic oil displacement process was recorded using a digital camera (Canon 60D, Japan).

## 3.2 Results and discussion

### 3.2.1 Petri dish tests

Fig. 3-3 illustrates the microscopic images of the aqueous-oil mixtures in different acid oil systems. Different emulsification behaviors were observed with the increasing amount of acid components in heavy oil. As shown in Fig. 3-3(a), the oil phase was well connected, indicating that there was no emulsification observed in the NAS system. After introducing the alkaline solution, the surfactant was produced in situ by a chemical action between the alkali and linoleic acid. The reaction formula is expressed in Eq. (1-1). As the surfactant produced, the IFT between oil and water was significantly reduced. When the IFT became ultralow value ( $< 10^{-3}$  mN/m), the emulsification can be induced, namely many tiny oil droplets were formed as shown in Fig. 3-3(b)–(c). We can see that these emulsions were type of oil-in-water (O/W). The oil emulsification ability was influenced by acid concentration. As shown in Fig. 3-3(d), a partial emulsification in LAS was produced, which meant that un-emulsified and emulsified regions were simultaneously observed. The un-emulsified region exhibited centimeter-sized oil blobs, while the emulsified region depicted oil droplets measuring several micrometers. A full emulsification behavior was observed at the high concentration HAS (Fig. 3-3(c)). We confirmed that the oil phase was completely formed into the micrometers of droplets, indicating a strong emulsified ability. Furthermore, we measured the viscosity of the full emulsions to be ~143 mPa·s, which is even higher than pure oil phase (89 mPa·s). This suggests that a stable displacement pattern may occur when a high viscous fluid displaces a low viscous fluid in porous media [20].



Wherein NaOH is sodium hydroxide; ROOH is linoleic acid; ROONa is the salt of linoleic acid (sodium linoleate); H<sub>2</sub>O is the produced water.



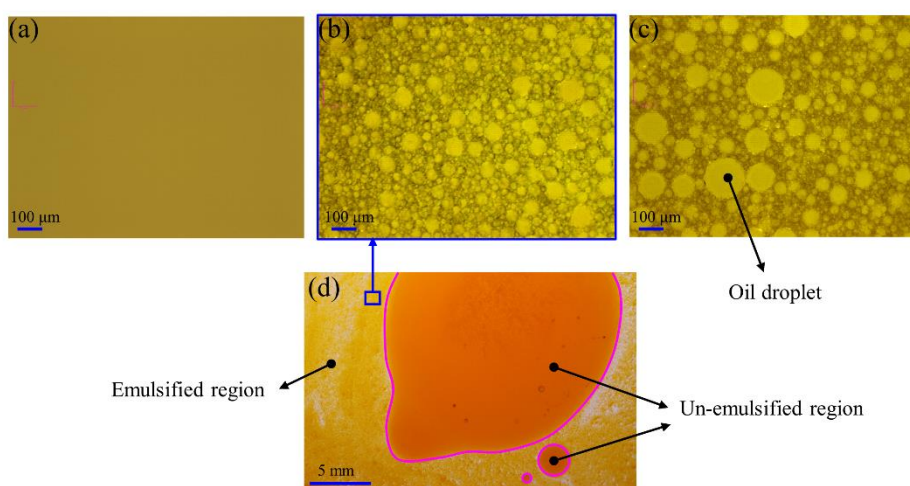


Fig. 3-3. Microscopic images ( $\times 400$  magnification) of aqueous-oil mixture after stirring for 60min in the (a) non-acid system, (b) low acid system, and (c) high-acid system in which different emulsification behaviors (i.e., none, partial and full emulsified ability) were observed, respectively. The low acid system presented (d) a partial emulsified ability; (b) close-up shows the emulsification in the emulsified region.

The oil droplet size is vital factor for improving oil recovery since it determines whether oil phase can pass through the pore spaces in porous media. The size distribution of oil droplets was analyzed with respect to the Petri dish tests, as shown in Fig. 3-4. For partial emulsification in LAS, the oil droplet size in the emulsified region was mainly distributed in 0.5–35  $\mu\text{m}$ , accounting for 93.3%. In comparison, the oil droplet size reached a centimeter order of magnitude in the un-emulsified region, indicating that large oil patches were very hard to pass through pore spaces in porous media. As an assumption, the partial emulsification may lead to a lower oil recovery performance in 3D core-flooding processes. In the full emulsification of HAS, 90% fraction of oil droplet size distributed ranging 0.5–35  $\mu\text{m}$  and the average size of all droplets was 15.9  $\mu\text{m}$ , which approaches that size of pore spaces in 3D porous media. In this sense, oil recovery could be significantly improved due to a well-matched size between oil globules and pore spaces.

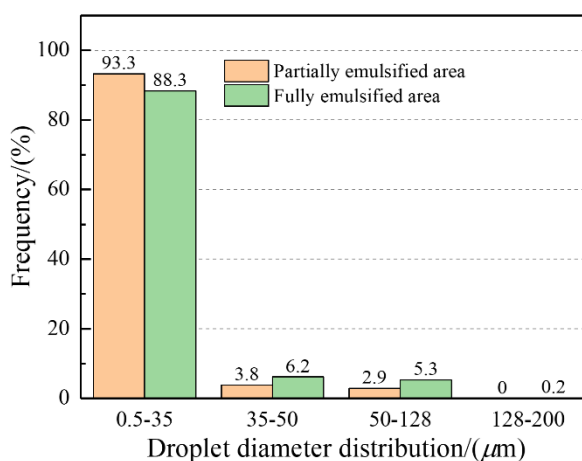


Fig. 3-4. Size distribution of emulsion droplets in partially and fully emulsified areas.

### 3.2.2 Core-flooding tests (3D)

#### 1) Oil displacement patterns

Fig. 3-5 depicts the evolution oil displacement patterns for different acid oil systems (i.e., NAS, LAS and HAS). All visualized surfaces were iso-contour surfaces corresponding to a saturation ratio of 0.27 (i.e.,  $f = S/S_0 = 0.27$ ), where  $S$  is the local oil saturation, and  $S_0$  is the initial oil saturation. Fig. 3-6 shows the images from a view of cross-sectional area in Fig. 3-5, respectively. As shown in Fig. 3-6(a), the oil displacement by pure waterflooding is very unstable, leading to an intensive VF occurrence. The VF pattern comprised a major large finger with various small branches, which showed a highly symmetric behavioral structure. Similar fingering pattern can be found in previous results of 2D porous media experiments [132]. With the continuous injection of water, the most advanced fingertip reached the bottom of the core sample, that is, a breakthrough happened at 0.13 PV. After the breakthrough, more additional oil was produced when the injection continued. Nonetheless, most of oil phase was bypassed because many viscous fingers were produced. Therefore, the water swept area was restricted to a large extent, leading to a low oil recovery (Fig. 3-5(a)). Fig. 3-5(b) and Fig. 3-6(b) displays the oil displacement pattern of LAS by alkaline flooding. In this acid system, the finger number was increased, and finger size presented thinner compared with that of non-acid system before breakthrough. Therefore, the swept area was initially smaller. However, the fingering was suppressed after breakthrough. The enlarged swept area was produced from the coalescences of thinner fingers. Hence, the oil recovery was improved at the end of 2 PV injection. The oil displacement pattern in HAS was shown in Fig. 3-5(c) and Fig. 3-6(c). As we can observe, the swept area was significantly expanded when subjected the alkaline flooding. The red mark in Fig. 3-6(c) indicates the displacement presented stable at 2 PV of the final injection. The displacement pattern shows that VF extended in all directions, and the fingers almost disappeared, indicating the highest sweeping area and oil recovery. The improved oil recovery in acid oil systems may attribute to the oil emulsification as shown in the results of Petri dish tests (Fig. 3-3). The emulsified ability in HAS was stronger than that of LAS, that is, full emulsification enables tiny oil droplets can easily pass through the pore spaces. Furthermore, the viscosity of O/W emulsions increased with the decreasing droplet size [75]. We measured the viscosity of the full emulsions to be ~143 mPa·s, which was even higher than that of heavy oil (89 mPa·s). A stable displacement should be produced when a high viscous fluid displaces a low viscous fluid [30].

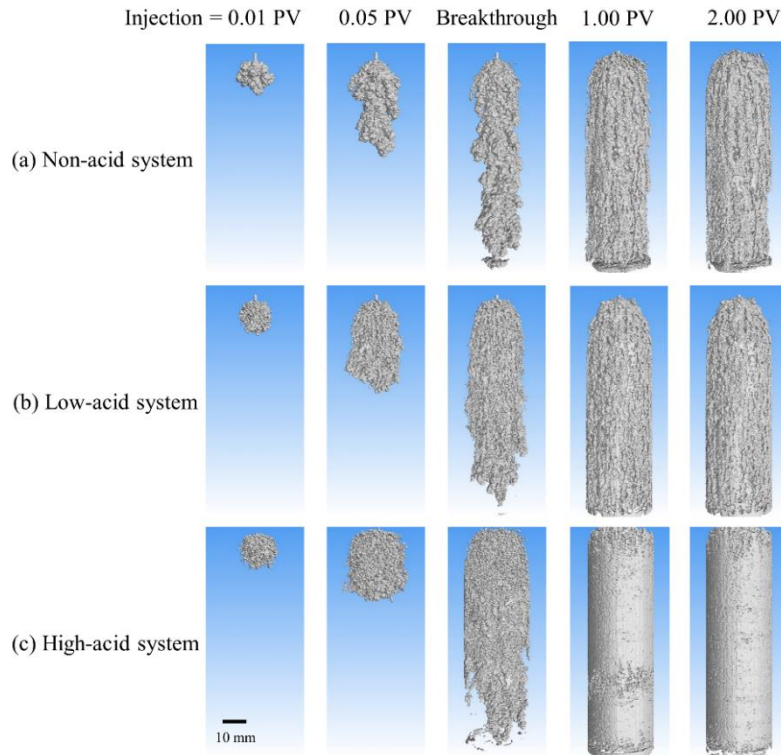


Fig. 3-5. Evolution of oil displacement patterns in 3D porous media for (a) non-acid, (b) low-acid, and (c) high-acid systems at a constant flow rate of 240 mL/h. The breakthrough for non-acid, low-acid, and high-acid systems is 0.13 PV, 0.13 PV, and 0.20 PV, respectively. The field of view vertically extends from the initial injection point to 90 mm.

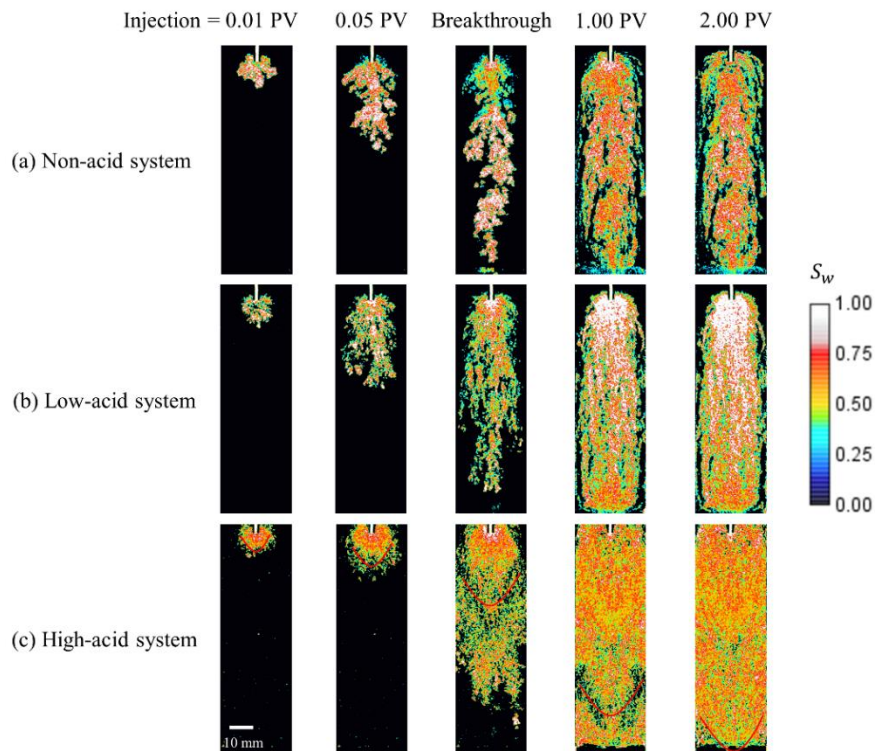


Fig. 3-6. Evolution of oil displacement patterns from a view of cross-sectional area with respect to Fig. 3-5 in

### 3. Effect of oil-acid concentration on performance of alkaline flooding application

3D porous media. The red bold line denotes the propagating stable interface in the high-acid system. The calibration bar shows the aqueous saturation ( $S_w$ ).

The VF evolution with relevance to nonlinear finger–finger interactions, such as tip-splitting, shielding, and coalescence, were also confirmed in the 3D porous media experiments (Fig. 3-6). During the vertical finger extension, one finger broke into two or three fine fingers at the tip of some fingers. This process could further aggravate with finger propagation. The shielding process also happened, which retarded the growth of the short finger by the most advanced neighboring fingers. After the breakthrough, the volume coverage was continuously enlarged because a large quantity of the adjacent fine fingers merged with each other in a process called coalescence. Nonlinear finger–finger interactions were also reported in our previous research [22].

Fig. 3-7 and Fig. 3-8 show the evolution of oil displacement patterns for different oil acid systems as a function of the flow rate in 3D porous media. In Fig. 3-7, the areal coverage of fingering was expanded as the flow rate increased in all acid systems. This enlarged area was related to the increased flow resistance with increasing flow rates. In addition, the breakthrough time was delayed as the flow resistance increased. As show in Fig. 3-7, it can be observed that the distance between the farthest fingertip and outlet for a low flow rate became shorter than that of higher flow rate, indicating that a lower flow rate gives rise to an earlier breakthrough. Fig. 3-8 also shows many fine fingers were produced in the acid systems, whereas that in non-acid system presented larger. The small fingers were possibly the intensive oil emulsions that produced by the combination of chemical reaction and shearing forces.

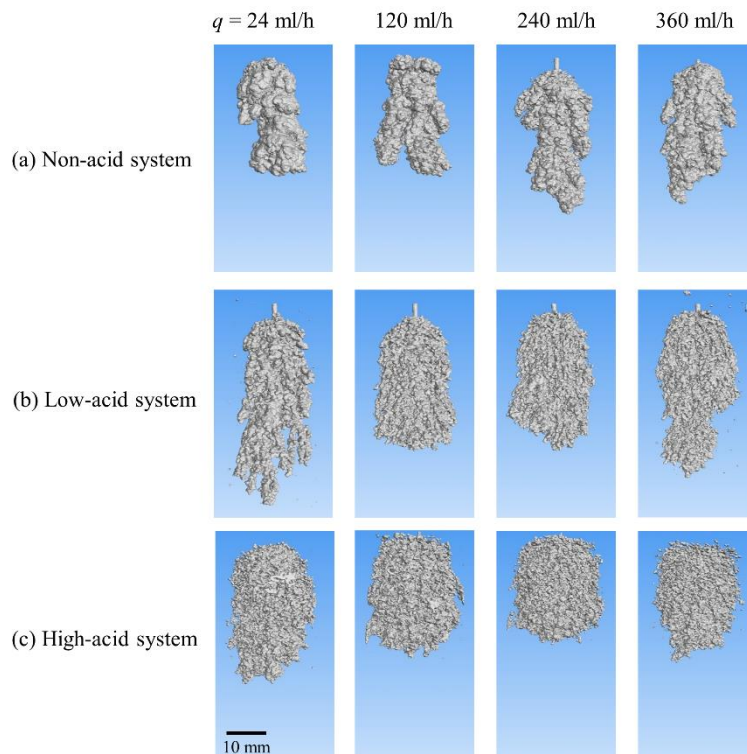


Fig. 3-7. Evolution of oil displacement patterns of different acid systems (a-c) for different flow rates. The injection was fixed at 0.05 PV. The field of view vertically extends from the initial injection point to 65 mm.

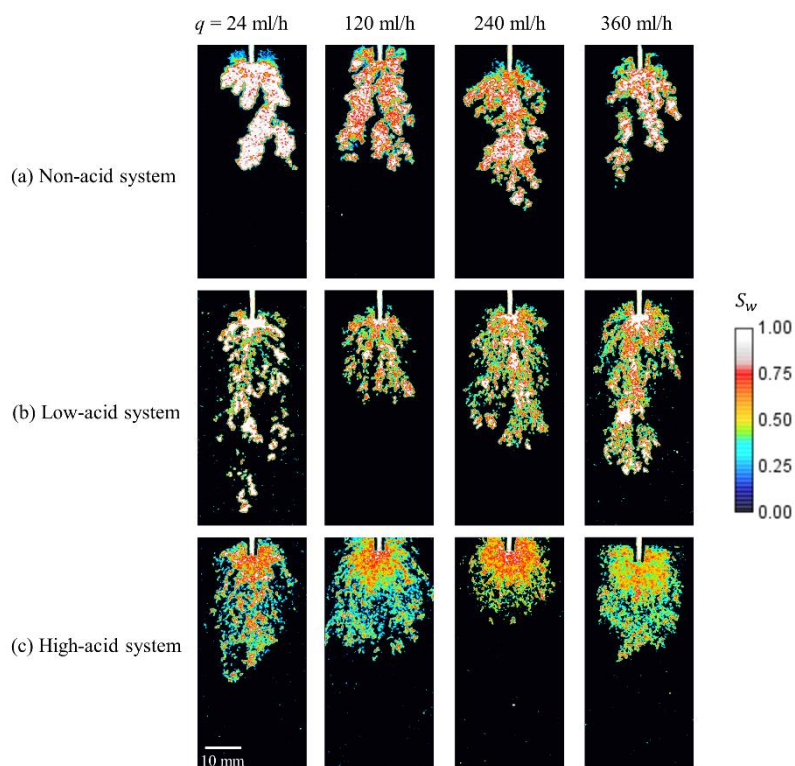


Fig. 3-8. The oil displacement patterns under different flow rates from a view of cross-sectional area with respect to Fig. 3-7. The calibration bar shows aqueous saturation ( $S_w$ ).

## 2) Oil recovery factor

Oil recovery factor is defined as the ratio of the cumulative oil production to the total volume of the OOIP. As aforementioned, the in-situ surfactant was produced in the porous media after alkaline flooding. Therefore, three different layers (i.e., water phase at the bottom, a thin layer of surfactant at the middle, and oil phase at the top) were observed when the effluents of the system were collected in a volumetric cylinder. The oil production was calculated based on the top layer (oil phase). The result of oil recovery factor is shown in Fig. 3-9.

The cumulative oil recovery first rapidly increased and then reached a stable value with the increasing injection. This variation trend was consistent with the oil displacement patterns of the X-ray CT images (Fig. 3-5). At the end of injection, the HAS produced the highest oil recovery, whereas the NAS produced the lowest oil recovery. To be more specific, the final oil recovery in HAS from the flow rate of  $q = 120$  mL/h to 360 mL/h reached 46.45% to 49.31% OOIP; that of the LAS varied from 33.16 to 40.16% OOIP; and that of the NAS was from 28.69% to 36.54% OOIP. The oil recovery suggested that a full emulsification in HAS exhibited the best performance in the oil displacement behavior. This can be attribute to that tiny oil droplets (smaller than pores and throats) were formed and

could easily pass through the pores and throats. This behavior is also called entrained flow by which oil droplets are entrained in water phase and flow to the outlet. In contrast, a fraction of oil phase was not emulsified in LAS. The oil droplet size was mostly larger than the pores and the throats, leaving many bigger oil clusters or ganglia unable to get through the tortuous pore structure. Nevertheless, the oil in emulsified region improved the oil recovery because of the entrained flow. However, there is no emulsification in the NAS, therefore, the oil recovery presented the lowest factor.

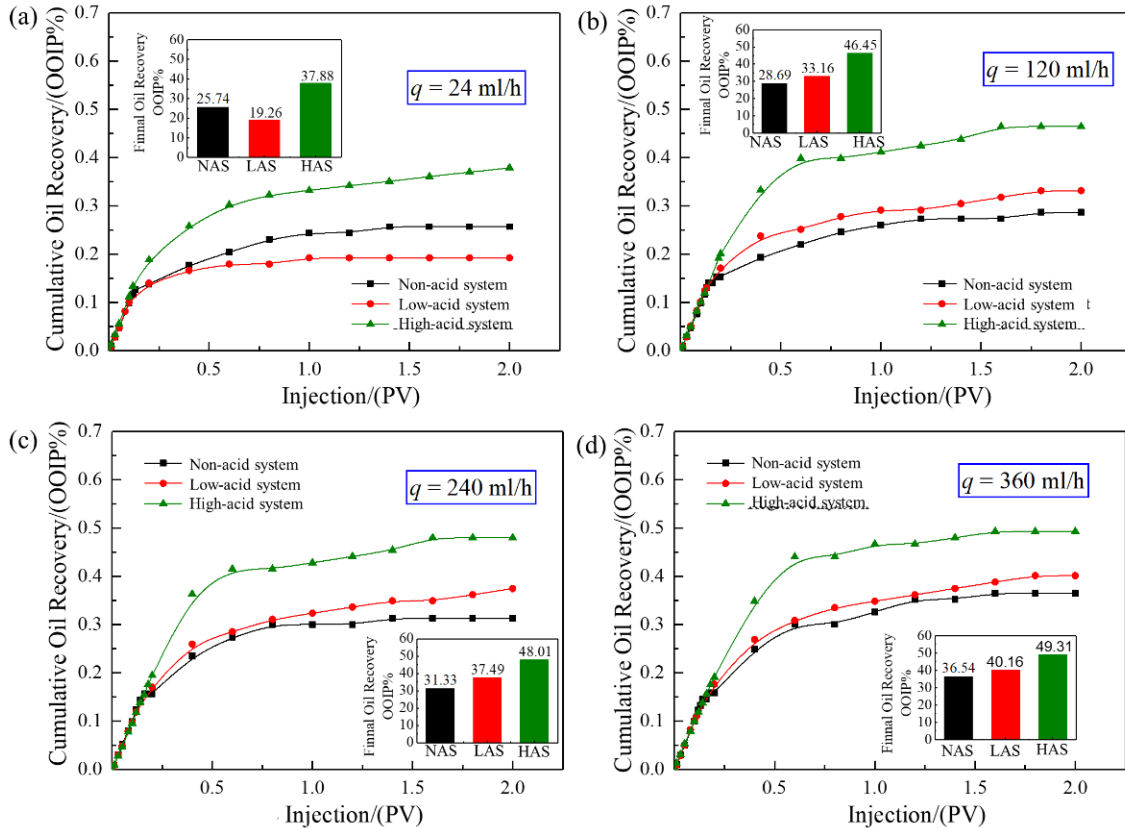


Fig. 3-9. Cumulative oil recovery as a function of the injection PV for the non-acid, low-acid, and high-acid systems. The flow rate of 24, 120, 240, and 360 mL/h are presented in (a-d), respectively. Inset: histogram of the final oil recovery in the three systems. The black, red, and green colors denote the non-acid, low-acid, and high-acid systems, respectively.

### 3.2.3 Micromodel tests (2D)

Last section provided the direct evidence that oil recovery is higher during the alkaline flooding process. However, the underlying mechanism cannot be observed in the large-scale porous media. To solve this, the pore-scale flow behavior was conducted in a 2D transparent micromodel to reveal the mechanism of oil displacement for 3D porous media experiments.

Fig. 3-10 shows oil displacement patterns at the flow rates of 1  $\mu\text{L}/\text{min}$ , 10  $\mu\text{L}/\text{min}$ , and 50  $\mu\text{L}/\text{min}$  for the non-acid, low-acid, and high-acid systems, respectively. This figure shows consistent observations in agreement with 3D oil displacement patterns (see Fig. 3-6). For example, The VF shows intensive pattern when there is no chemical reaction in NAS. In

contrast, that was suppressed by the chemical reaction in LAS and HAS. In the other words, the swept area in NAS was smaller than that in LAS at each flow rate, suggesting that the produced surfactants positively affected the remobilization of more residual oil. With increasing acid concentration in HAS, the swept area was significantly enlarged, indicating a high-level stable displacement and oil recovery efficiency. The results of Petri dish test (Fig. 3-3) implies that the oil recovery performance was associated with the emulsification ability as the acid concentration increased. In addition, the swept area was enlarged with the increasing flow rate. Pioneering research showed that more residual oil was mobilized and removed as the  $Ca$  number increased, consequently increasing the oil sweep efficiency [133].

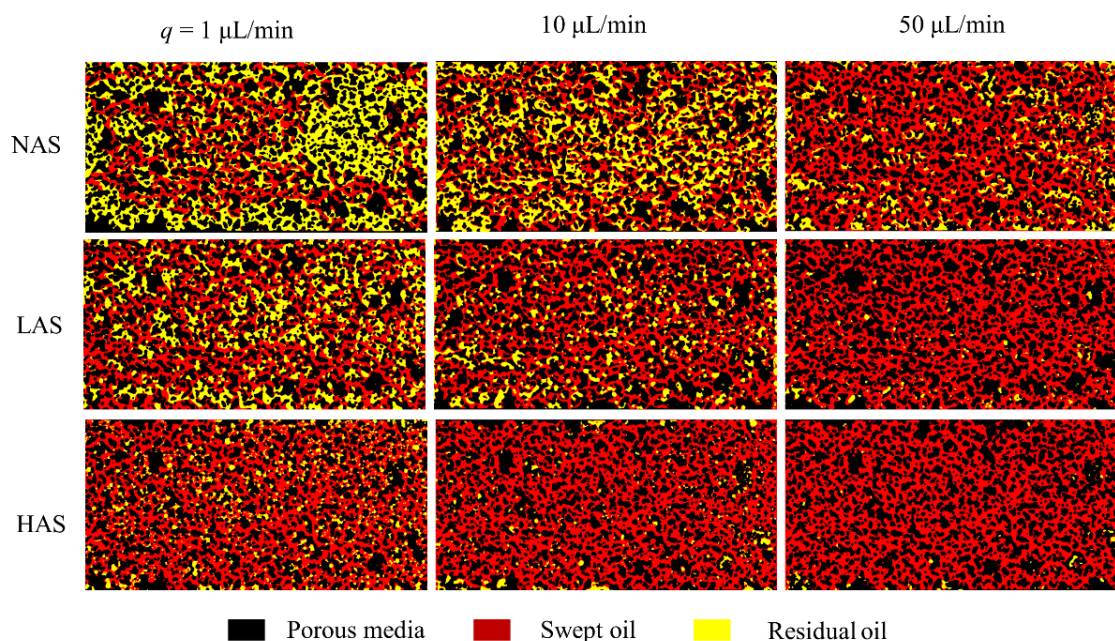


Fig. 3-10. Images of the oil displacement patterns in the microfluidic chip (length  $\times$  width = 20  $\times$  10 mm) at the flow rates of 1  $\mu\text{L}/\text{min}$ , 10  $\mu\text{L}/\text{min}$ , and 50  $\mu\text{L}/\text{min}$  for different acid oil systems (NAS, LAS and HAS). The black, red, and yellow colors denote the porous media, swept oil, and residual oil, respectively. All images are the flow patterns at the end stage of injection.

The oil droplet size played a key role in the oil displacement performance when the O/W emulsification occurred in the porous media. The ideal oil droplet size should be smaller than the diameter of pores and throats. As such, the emulsion droplets that entrained in the aqueous phase can be regarded as a continuous phase [134], and oil recovery is highly enhanced by the entrainment flow [71]. As shown in Fig. 3-11(a), it can be observed that no emulsification, partial emulsification, and full emulsification occurred in the non-acid, low-acid and high-acid oil systems, respectively, which agrees well with the Petri dish tests (Fig. 3-3). After waterflooding in NAS, many large-sized oil clusters/ganglia were entrapped by capillary pressure in the pores and the throat, leading to a very low oil sweeping efficiency. After alkaline flooding, the oil cluster size decreased because of partial emulsification in LAS. However, many oil globule sizes were still not very effective in passing through the pore–throat structure, leaving many bigger oil clusters trapped.

Therefore, the oil recovery factor is still limited. The partial emulsification can attribute to the insufficient surfactants that produced by low acid concentration. In the other words, the high acid concentration could produce sufficient surfactants. Consequently, a full emulsification will dominate in the oil displacement patterns. Fig. 3-11(a) indicates the effective emulsified ability in HAS. We can observe that even the residual oil clusters/ganglia in the dead pores from LAS were also emulsified into many small oil droplets, allowing the oil droplets to possibly be entrained in the water phase and pass through the pore-throat channels. The results were very aligned with those in the previous works [135].

We quantified the oil droplet size distribution to further describe the non-emulsification, partial emulsification, and full emulsification phenomena as shown in Fig. 3-11(b)-(c). Fig. 3-11(b) depicts an obvious reduction in the oil droplet sizes, indicating that the emulsified ability increased as the oil acidity increased in heavy oil. Note that all size of the oil individuals were normalized as diameter of standard circle. As shown in this figure, the average size oil droplet significantly decreased with the increasing acid concentration, corresponding to the values of 278.5  $\mu\text{m}$ , 156.1  $\mu\text{m}$ , and 78.8  $\mu\text{m}$  for NAS, LAS and HAS, respectively. As aforementioned, the pore diameter of 3D porous media was less than 130  $\mu\text{m}$ , which means 78  $\mu\text{m}$  of droplets could easily pass through the pore spaces in HAS.

Fig. 3-11(c) shows the frequency distributions of the oil droplets in the non-acid, low acid and high-acid oil systems. As illustrated, the sizes of 27.3% oil clusters in NAS were distributed in 50–128  $\mu\text{m}$ ; 54.5% oil clusters were distributed in 128–600  $\mu\text{m}$ ; and 14.3% oil clusters ranged from 600 to 1100  $\mu\text{m}$ . Smaller oil droplets started to form in LAS in which a partial emulsification produced. The bigger oil droplets in NAS ranging from 600 to 1100  $\mu\text{m}$  disappeared. The oil droplet sizes of 50–128  $\mu\text{m}$  increased to 44%, while the sizes of 128–600  $\mu\text{m}$  decreased to 50.2%. By contrast, full emulsification spontaneously occurred when the oil acid concentration was high. The full emulsification characteristic was identified as a complete formation of the oil droplets in the porous media. The oil droplet sizes ranging from 5 to 50  $\mu\text{m}$  largely increased to 28.6%. The size of 50–128  $\mu\text{m}$  increased to 53.6%. The larger size of 128–600  $\mu\text{m}$  tightly decreased to 17.8%. Note that the 2D and 3D porous media shares similar pore-throat structure with average pore diameter of 130  $\mu\text{m}$ . Based on this, the size of the pore-throat structure suggested that much smaller oil droplets in HAS could easily pass through the pores and the throat in both 3D and 2D porous media. Furthermore, the capillary forces were significantly decreased because of a large extent of IFT reduction in the oil-water interface, which is conducive to remobilize oil droplets. Therefore, the full emulsification produced the highest oil sweeping efficiency, followed by the partial emulsification.



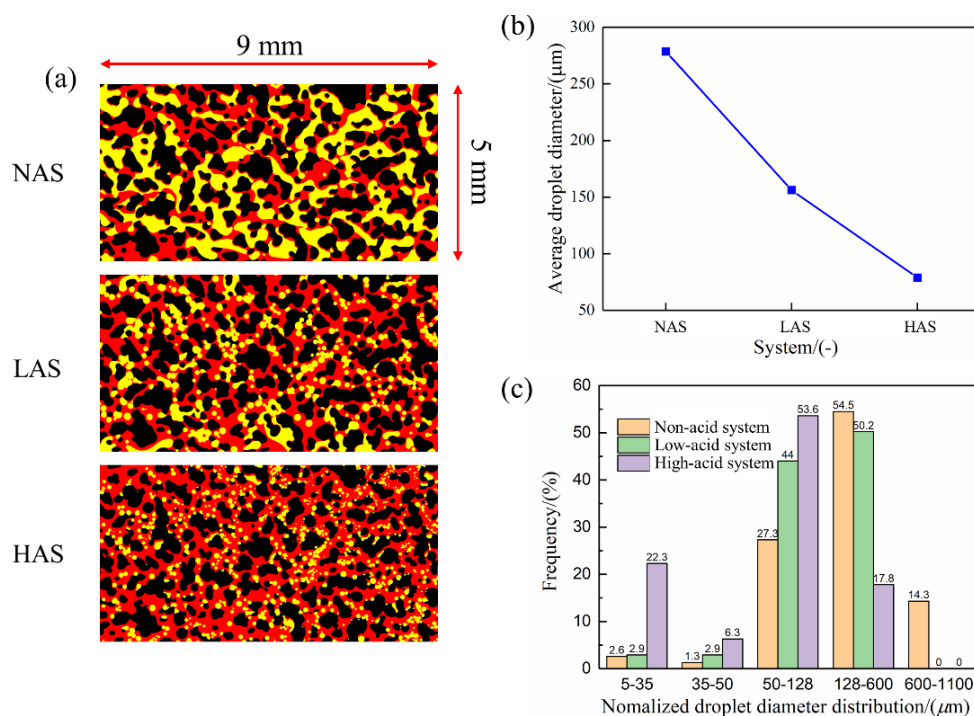


Fig. 3-11. Oil droplet size distribution of different acid oil systems (NAS, LAS and HAS) in porous media at the flow rate of 10  $\mu\text{L}/\text{min}$ : (a) Pore-scale visual observation, (b) Average oil droplet size, and (c) Frequency distribution of oil droplet size.

The emulsion formation is a complicated physical and chemical process in porous media, which is influenced by various factors, such as surfactant concentration, pore structure, pore throat, flow rate, and the like, etc. [75]. Fig. 3-12 and Fig. 3-13 show the different mechanisms of the emulsion formation in porous media for the partial and full emulsifications. As shown in Fig. 3-12, three types of the O/W emulsion formation were confirmed in the experimental observations of LAS: snap-off, splitting, and division. Snap-off was extensively observed in the porous media, as displayed in the image data of (A): (a)  $\rightarrow$  (b) and the schematic illustration of (B): (a)  $\rightarrow$  (b). The oil ganglia or larger oil droplets were lengthened and constricted into oil threads when they passed through a narrower pore throat. Under a sufficient constriction effect, the water film accumulated at the throat until it eventually bridged and snapped off the oil thread [136,137]. Splitting was frequently observed when two or more closely attached oil droplets propagated forward in the pores, as shown in image of (A): (c)  $\rightarrow$  (d) and the schematic illustration of (B): (c)  $\rightarrow$  (d). This behavior usually occurs at the joint of two droplets, where the curvature is very large. Another mechanism, called division, refers to the bended oil ganglia colliding with grains and divided into two oil droplets with the assistance of the injection velocity as the driving force, as clearly shown in (A): (e)  $\rightarrow$  (f) and (B): (e)  $\rightarrow$  (f). The IFT reduction could also weaken the interfacial film strength [138], which assisted for the easy breakup of the oil droplets.

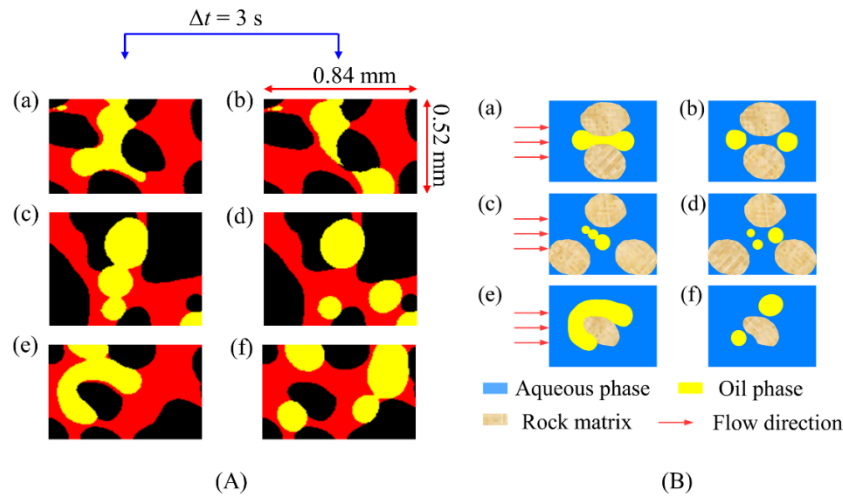


Fig. 3-12. Snap-off, splitting, and division mechanisms of the oil droplet formation in the partial emulsification of LAS: (A) group of images showing the experimental observation and (B) group of images showing a schematic illustration of the oil droplet formation. The time interval of the two consecutive images is 3 s.

We found a spontaneous emulsification occurred during the dynamic displacement in the high-acid oil system (Fig. 3-13). The shearing forces dominated for the full emulsification instead of interaction with the porous media that shows in Fig. 3-12. The trapped oil cluster was gradually carried away in the form of fine oil droplets by the alkaline solution during the shearing forces. This is shown in the sequential process of (A): (a) → (b) → (c) → (d) and (B): (a) → (b). As aforementioned, the tiny oil droplets were entrained in the aqueous phase flow, thereby leading to a emulsion–entrainment flow, which agrees well with the previous research results (Zhou et al., 2017). Under the shearing action effect, even the residual oil in the dead-end pores could be gradually emulsified into many fine oil droplets. Therefore, in the high-acid oil system, a full emulsification could be produced during the shearing action and had the best oil recovery performance than that of the low-acid oil system.

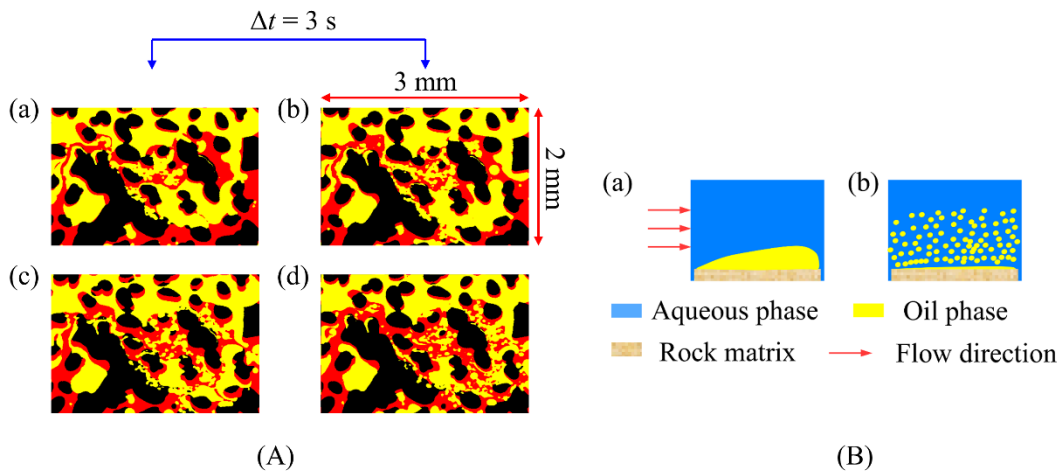


Fig. 3-13. Shearing action mechanism of the oil droplet formation in the full emulsification of HAS: (A)

group of images showing the experimental observation and (B) group of images showing the schematic illustration of the oil droplet formation. The time interval of the two consecutive images is 3 s.

### 3.2.4 Proposal for industrial applications

In nature, the heavy oils contain a certain amount of organic fatty acids. The total acid number can range from 0.02 to 16.2 mg KOH/g depending on different oil reservoirs in regions [49]. Alkaline flooding has received much attention for EOR because of its effective chemical reaction with acid components. As a result, the IFT can be significantly reduced, thereby leading to spontaneous emulsification. In this study, no emulsification, partial emulsification, and full emulsification were confirmed in the pure oil (0 mg KOH/g), low-acidity oil (0.135 mg KOH/g), and very high-acidity oil (13.5 mg KOH/g) reservoirs, respectively. Fig. 3-14 provide the possible patterns of oil displacement by alkaline flooding in actual acid oil reservoirs.

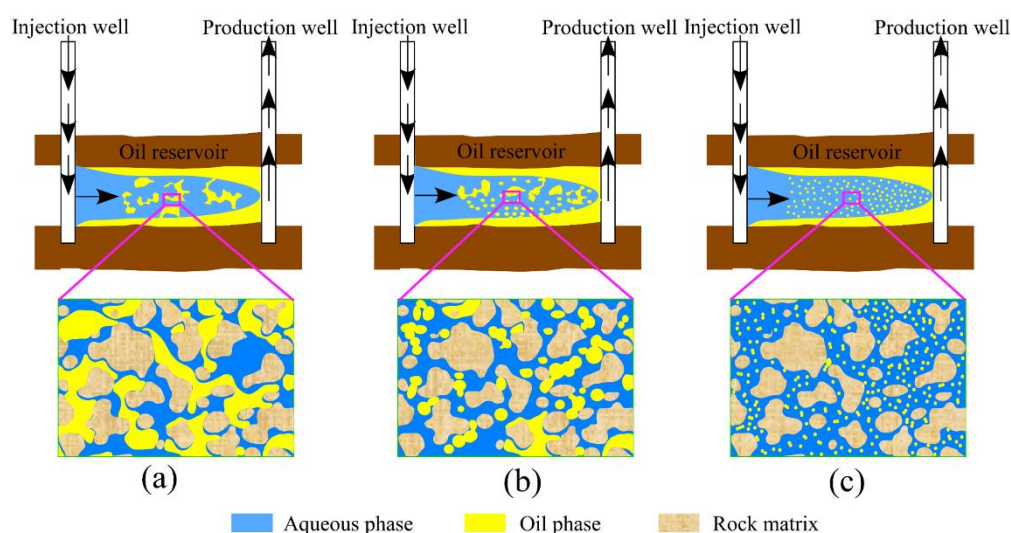


Fig. 3-14. Schematic illustration possible patterns of oil displacement in non-acid, low-acid, and high-acid oil reservoirs in which (a) no emulsification, (b) partial emulsification, and (c) full emulsification may occur during the alkaline flooding. The blue, yellow, and light brown colors denote the aqueous solution, oil phase, and rock matrix, respectively.

In the non-acid oil reservoir, Fig. 3-14(a) shows that many large sizes of the oil cluster/ganglia were entrapped by the capillary forces in the pores and throats, leading to a very low oil recovery efficiency. For the low-acid oil reservoir [Fig. 3-14(b)], the partial emulsification was predominated by three pronounced processes: snap-off, splitting, and division [Fig. 3-12(b)]. The sizes of the oil droplet formation are mostly larger than those of the pores and throats. Furthermore, some residual oil clusters/ganglia are un-emulsified and has a centimeter order of magnitude, leading to the oil entrapments in the pores and throats, especially in dead-end regions. In this case, the oil recovery is limited although that in the emulsified region is effective. A full emulsification is desired in the high-acid oil reservoir to obtain the most favorable oil recovery [Fig. 3-14(c)]. This characterization of a strong emulsification ability suggests the highest oil recovery could be obtained by the effective

entrainment–emulsion flow. In summary, the alkaline flooding for oil recovery may increase if applied for the acid-increasing oil reservoir because of the reinforcement of the emulsification ability transition from partial to full emulsification. Therefore, the alkaline flooding is suggested to applied for the high-acid oil reservoir in which a full emulsification may occur, such as the Aradeiba and Bentiu reservoirs located in Sudan, where the average TAN was over 6 mg KOH/g [49].

### 3.3 Summary

This chapter conducted the oil displacement by alkaline flooding in 3D porous media using an X-ray CT device and analyzed the effect of the acid concentration and flow rate on oil recovery performance. 2D transparent microfluidic experiments were performed to obtain the pore-scale displacement mechanism that may occurred in the 3D porous media. Finally, an application for industrial oil recovery was proposed based on the experimental results. Some of the key conclusions drawn in this chapter are as follows:

(1) The swept area and oil recovery factor were increased with the increasing acid concentration and flow rates during the alkaline flooding process. The surfactant can be produced in situ by the chemical reaction between the NaOH and fatty acid. The viscous fingering can be significantly suppressed, leading to a good control of stable displacement. Therefore, alkaline flooding shows the most potential in an oil reservoir with high acid components. For instance, we found that the optimal flow rate for oil recovery was 360 mL/h at which the oil recovery factor increased from 36.5% to 49.3% OOIP as the acid concentration ranged 0–0.2 mol/L.

(2) The emulsification ability became stronger with the increasing acid concentration, transitioning from partial to full emulsification during the alkaline flooding process. The partial emulsification in low-acid oil system was characterized by the emulsified and un-emulsified regions in the porous media. In the emulsified region, the emulsion formation was predominated by the snap-off, splitting, and division processes, leading to many bigger sizes of oil droplet (~156.1  $\mu\text{m}$ ) than the pore sizes (~130  $\mu\text{m}$ ). In the un-emulsified region, well-connected residual oil clusters were entrapped in the pore spaces, which was similar to that of non-acid oil system. A full emulsification in high-acid oil system was spontaneously produced, leading to the uncountable oil droplet formations with tiny sizes ~78.8  $\mu\text{m}$  which matched well with the pore–throat size. The tiny oil droplets were effectively entrained in the water phase and passed through the pores and throats, namely “entrained flow”, thereby resulting in the most satisfactory oil recovery.

(3) As an optimal scenario for engineering, alkaline flooding is suggested to applied for high-acid oil reservoirs (e.g., Aradeiba and Bentiu reservoirs in Sudan), where the average TAN was over 6 mg KOH/g.

## 4 Solvent-based microemulsion flooding with quasi-miscible behavior regardless of oil-acid concentrations

**Objective:** Chapter 3 found the performance of alkaline flooding for the high-acid oil recovery is the most effective because emulsification has two advantages: good control of stable displacement and entrained flow. However, a large quantity of oils was bypassed because capillary forces still dominated in the low-acid oil reservoirs. How to remove the capillary forces and control the stable displacement is important to produce these low-acid oils. Based on this point, emulsion flooding is good choice to control the stable displacement and miscible flooding can remove the capillary forces. In this chapter, we combine the emulsion flooding and miscible fluid to make a novel miscible emulsion flooding that can improve oil recovery efficiency regardless of the oil-acid concentrations. That is, the novel agent can control the stable displacement (viscous fingering suppression) and eliminate the (positive and/or negative) capillary forces at the same time. The stable displacement and miscible behavior will be visualized from the pore spaces using the X-ray micro-CT. Finally, the scenario for enhanced oil recovery will be proposed in an actual industrial application.

### 4.1 Experimental

#### 4.1.1 Materials

Liquid paraffin oil (Wako 1st grade, FUJIFILM) doped with linoleic acid (Wako 1st grade, assay  $\geq 88\%$ , FUJIFILM) was used to represent acidic crude oil. Sodium chloride (NaCl) (guaranteed reagent, purity  $\geq 99.5\%$ , Kanto Chemical Co.) and sodium iodide (NaI) (guaranteed reagent, purity  $\geq 99.5\%$ , Kanto Chemical Co.) were used to improve the brine salinity and enhance the image contrast during X-ray CT scanning, respectively. The emulsion was prepared using sodium linoleate (anionic surfactant, reagent purity  $\geq 95\%$ , Tokyo Chemical Industry), 2-butanol (guaranteed reagent, purity  $\geq 99\%$ , Kanto Chemical Co.), n-decane (Guaranteed reagent, purity  $\geq 99\%$ , Kanto Chemical Co.), and water from a Milli-Q purification system. Octadecyltrichlorosilane (OTS) (guaranteed reagent, purity  $\geq 94\%$ , Shin-Etsu Chemical Co.), toluene (extra pure, purity  $\geq 99\%$ , Kanto Chemical Co.), and ethanol (extra pure, purity  $\geq 99.5\%$ , Kanto Chemical Co.) were selected for the wettability alteration in porous media to strong oil-wet. All the chemicals were used as received without further filtration or purification.

#### 4.1.2 Test fluids

Paraffin oil was used to represent the heavy oil phase in an oil-bearing reservoir. We added 0.02 mM linoleic acid to the oil phase to control the acidity for a total acid number of 1.35 mg KOH /g. In the water flooding (WF) experiment, the injected fluid is de-ionized (DI) water doped with 4% wt. sodium iodide (NaI) to enhance the image contrast during X-ray CT scanning. In the EF experiment, the microemulsion phase was prepared in a beaker with

#### 4. Solvent-based microemulsion flooding with quasi-miscible behavior regardless of acid concentrations

50% wt. emulsifier solution and 50% wt. n-decane oil (water-oil ratio (WOR) = 1:1) using a magnetic stirrer (RS-4AN, As One, Japan) at a speed of 1000 rpm. The emulsifier solution, containing 5% wt. 2-butanol, 0.5% wt. sodium linoleate (surfactant), and 94.5% wt. DI water, was stirred at 700 rpm. The 2-butanol as a co-solvent increases the solvent power and stabilizes the emulsion phase. Sodium linoleate was selected as the surfactant because of its high performance in oil recovery, which was produced in situ from alkaline flooding [67]. n-decane was doped with 30% wt. iododecane to provide the proper contrast in emulsion for CT scanning. It is noted the prepared emulsion phase is a new kind of solvent-based emulsion in which n-decane was used as a solvent agent. The partition coefficient of surfactant in the emulsion phase was estimated to ~2.3 in an equilibrium condition (see Eq. (2) in Ref. [140] for calculation). In enhanced oil recovery (EOR) experiments, water-alternate-emulsion (WAE) flooding was conducted to simulate a real EOR application.

Prior to the core-flooding experiments, the formation and stability of the new solvent-based microemulsion over time under equilibrium conditions were monitored in a graduated cylinder for one week. The NaCl salt within 0–1.8 wt.% was added into the emulsion to examine the effect of salinity on the emulsion stability. The optimum emulsion (with high stability) was confirmed and used in subsequent emulsion injection experiments. The size distribution of the optimum emulsion droplets was characterized using a microscope (YDU-3S, Yashima Optical Co., Japan). The fluid viscosity was measured using a viscometer (Sine-wave Vibro Viscometer-SV 10, A&D Co., Ltd., Japan). The IFT was examined by pendant-drop analysis (DSA 25, Krüss Scientific, Germany). The properties of the fluids used in six sets of core-flooding experiments are summarized in Table 4-1.

Table 4-1. The properties of injected and displaced fluids in core-flooding experiments under room conditions.

Test	T1: WF	T2: WF	T3: EF	T4: EF	T5: Tertiary EF	T6: Tertiary EF
Injected fluid	Water	Water	Emulsion	Emulsion	WAE	WAE
Displaced fluid	Paraffin oil	Paraffin oil	Paraffin oil	Paraffin oil	Paraffin oil	Paraffin oil
Wettability	Water-wet	Oil-wet	Water-wet	Oil-wet	Water-wet	Oil-wet
$\rho_w$ (kg/m <sup>3</sup> )	1020	1020	—	—	1020	1020
$\rho_e$ (kg/m <sup>3</sup> )	—	—	876	876	877	877
$\rho_o$ (kg/m <sup>3</sup> )	837	837	837	837	837	837
$\mu_w$ (mPa·s)	1.25	—	—	—	1.25	1.25
$\mu_e$ (mPa·s)	—	—	53.2	53.5	52.6	53.7
$\mu_o$ (mPa·s)	89.2	89.8	89.1	90.5	89.8	90.1
$\gamma_{wo}$ (mN/m)	12.6	12.6	—	—	12.6	12.6

$\gamma_{eo}$ (mN/m)	—	—	1.12	1.23	1.21	1.18
----------------------	---	---	------	------	------	------

\*WF and EF are waterflooding and emulsion flooding.

\*WAE is water-alternate-emulsion flooding.

\* $\rho_w$ ,  $\rho_e$ , and  $\rho_o$  are the water, emulsion, and paraffin oil density.

\* $\mu_w$ ,  $\mu_e$ , and  $\mu_o$  are the water, emulsion, and paraffin oil viscosity.

\* $\gamma_{wo}$  and  $\gamma_{eo}$  are the water-oil and emulsion-oil interfacial tension.

### 4.1.3 Sand-pack preparation

Toroura silica sand (TK-416, Toyoura Keiseki Kogyo Co.) is a high-quality silica sand ( $\text{SiO}_2$ ) that was selected to represent natural porous media in oil sands reservoirs. First, the sand particles were rinsed in an ultrasonic water bath (ASU-6M, As One, Japan) for 30 min to remove surface ash. Then, the dried particles were sequentially processed in ethanol and water to remove organic matter. Next, a mini sieve shaker (MVS-1, As One, Japan) was used to control the particle size within 212–250  $\mu\text{m}$  for standby usage.

#### 1) Property determination

The cleaned sand was poured into a transparent acrylic resin container with an inner diameter and height of 8 mm and 15 mm, respectively. The sand was compressed using a plastic rod of equal diameter to the container to produce a dense pack. Then, the sandpack was fixed on the stage between the X-ray source and detector; the CT scanning resolution was set as 4.197  $\mu\text{m}/\text{pixel}$ . The high resolution requires that X-ray CT scanning be performed twice in the whole sample detection process. Fig. 4-1 shows the resulting porous media properties. Fig. 4-1(a) shows the 3D pore structure of the porous media reconstructed from the image stack. Based on this structure, the average porosity (Fig. 4-1(d)) was measured as 35%. An area of  $3 \times 3 \times 3 \text{ mm}^3$  (Fig. 4-1(a)) was selected to extract the coordination number (Fig. 4-1(c)) and pore-throat diameter (Fig. 4-1(e)). The pore-throat network (Fig. 4-1(b)) was constructed using the SNOW algorithm coded in the Python toolkit-PoreSpy module [141,142]. The average coordination number  $\sim 5.37$  was then obtained, which agrees well with that from previous study on the random packing of Ottawa sand with a similar porosity of approximately 5.0–6.0 [143]. The pore-throat size distribution plotted in Fig. 4-1(e) indicates that their average diameters are 36  $\mu\text{m}$  and 33  $\mu\text{m}$ , respectively. The absolute permeability was measured to be 10 Darcy according Darcy's law after WF.

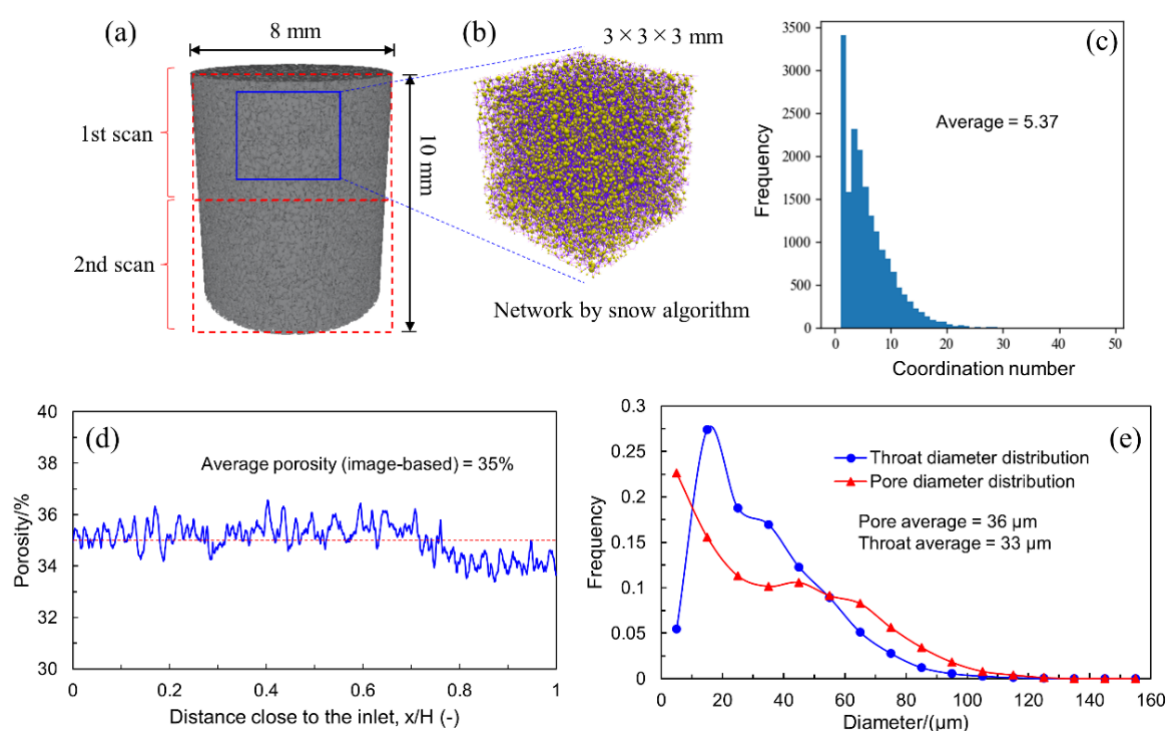


Fig. 4-1. The porous media properties including (a) three-dimensional reconstruction of X-ray CT images; (b) pore-throat network using the SNOW algorithm; (c) distribution of the coordination number; (d) image-based porosity; and (e) pore-throat size distribution.

## 2) Wettability alteration protocol

The performance of EF in strongly water-wet and oil-wet porous media will be examined, corresponding to strong positive and negative capillary forces, respectively. Therefore, the wettability of the sand surface was first altered to water-wet and oil-wet conditions prior to the core-flooding experiments. The altered wettability was evaluated through the contact angle (CA) of a sessile drop (DSA 25, Krüss Scientific, Germany) on a glass slide (same material as sand). Fig. A-B1 shows the CA measurement results after different processing protocols (see Appendix B). For the strong water-wet alteration, the washed sand was exposed to plasma ion irradiation inside a vacuum chamber (PIB-10, Vacuum Device Co., Japan). The average CA was measured as  $\sim 30^\circ$ , indicating a strong affinity to the water phase. The oil-wet alteration was carried out by coating the OTS chemical on the sand surface. Specifically, OTS was added to toluene to adjust the concentration (0.0001–0.1 v/v%) of the OTS solution. Then, the sand was immersed in the OTS solution and vigorously stirred for 30 min. Afterwards, the sand was flushed using ethanol and water to remove residual chemicals, and finally dried off by heating. Fig. A-B1 shows that the sand surface approached the oil-wet condition with increasing OTS concentration. The equilibrium CA was measured as  $140^\circ$ ; thereafter, we selected a 0.01% OTS solution for the oil-wet sand treatment.



#### 4.1.4 Experimental apparatus and procedure

##### 1) Devices and accessories

A schematic of the core-flooding system used in this study is shown in Fig. 4-2, which includes the vertically held sandpack, fluid injection system, and micro-CT scanner (ScanXmate-CF110TSS300, Comscantecno Co. Ltd., Japan) coupled with an image reconstruction software. The sand was packed inside a transparent acrylic resin holder with an inner diameter of 8 mm and a height of 15 mm. A plastic rod was used to compress for a dense pack. Fine glass beads (100  $\mu\text{m}$ ) were attached to the holder wall to avoid the bypass of wall effect. The top of the holder was connected to the side of the water or microemulsion supply, while the bottom was connected to the oil injection by Teflon tubing and fittings. Two flow straighteners were placed at the top and bottom of the sample to distribute the injection fluid uniformly.

##### 2) Procedures

The core-flooding experiments were performed as follows. The core sample was first vacuumed and then fully saturated with brine ( $S_w = 1$ ). Afterwards, the sample was mounted on the stage of the X-ray device and 15 pore volumes (PVs) of paraffin oil were injected to flush the entire sample at a flow rate of 100  $\mu\text{L}/\text{min}$  (Line 1 in Fig. 4-2). This step created a connate water condition ( $S_w \approx 0.3$ ) for all tests. In tests T1–T4, the sample was subjected to direct WF or EF to simulate secondary recovery under both water-wet and oil-wet conditions (Line 2 and Line 3 in Fig. 4-2). The flow rate was controlled to 10  $\mu\text{L}/\text{min}$  by a syringe pump (Model 100, KD Scientific, United States). The injected PVs ranged from 0.5 to 3.0 with an interval of 0.5 PV. It should be mentioned that the 10  $\mu\text{L}/\text{min}$  flow rate corresponds to approximately 1 ft/day, which is the widely accepted fluid velocity in hydrocarbon applications. For tests T5 and T6, 1.5 PV WF was followed by 3.5 PVs of EF to mimic the EOR method under both water-wet and oil-wet conditions. CT scanning was conducted to obtain the pore-scale fluid occupancies after each injected PV. During each CT scan, two scans were required to visualize the entire sample (see Fig. 4-2). All of the experiments were carried out under room conditions.

##### 3) X-ray micro-CT setting

X-ray energies were emitted through the tube sources at a voltage of 70 kV and a current of 120  $\mu\text{A}$ . The CT resolution was set to 4.197  $\mu\text{m}/\text{pixel}$  by changing the core sample position close to the X-ray source. The X-ray detector recorded the spatial distribution of the transmitted X-ray intensities across each projection. During the scanning, the sample rotated 360° within 20 min for image collection. Each scan produced 1300 image slices with an area of  $2304 \times 2304$  pixels<sup>2</sup>; this means that the field of view (FOV) covered a volume of  $8.3 \times 8.3 \times 4.7$  mm<sup>3</sup>. In this study, each fluid injection required two scans, that is, the FOV could reach the approximately 10 mm height of the sample; the total working time required is 40 min.

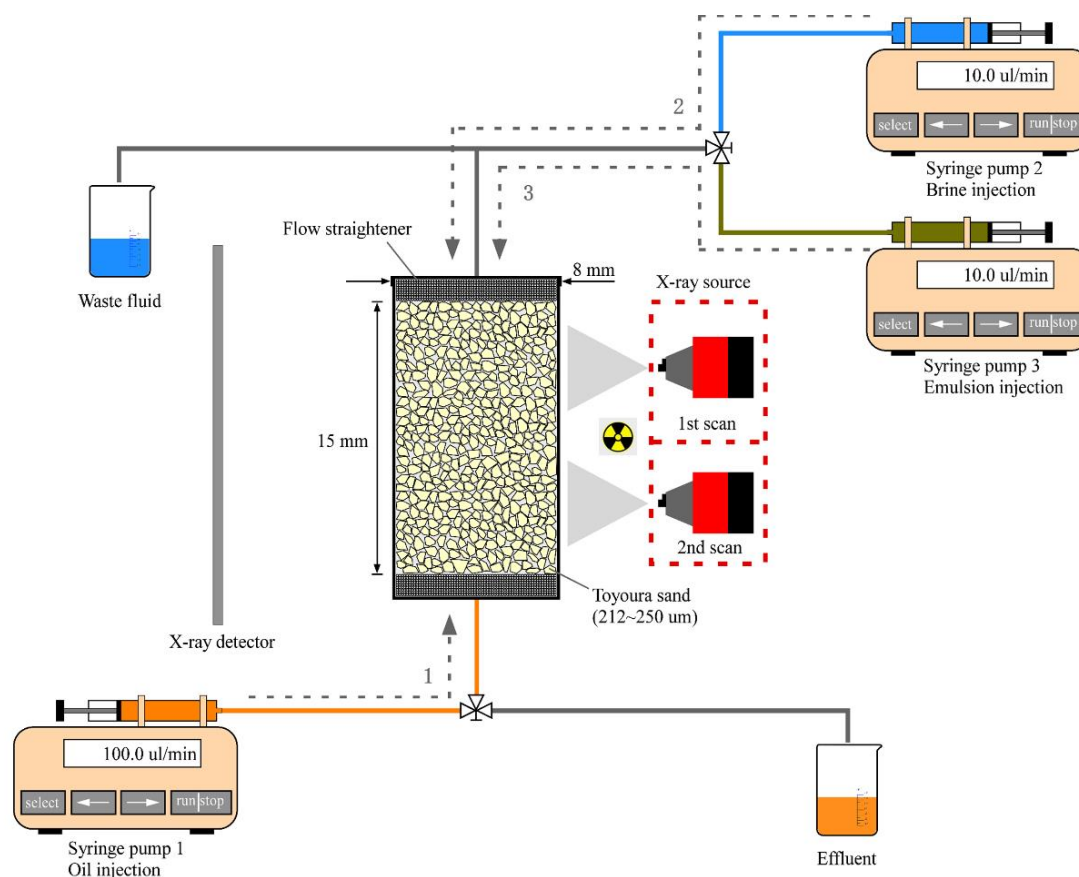


Fig. 4-2. Schematic of waterflooding and emulsion flooding experiments on wettability-altered reservoirs using X-ray microtomography. The arrows with dashed lines indicate the direction of fluid injection. The experimental conditions are room pressure and temperature.

#### 4.1.5 Image processing workflow

All the tomograms were reconstructed using an in-house software, and 16-bit gray image slices were obtained. To extract quantitative information from the images, different image processing methods were adopted for WF and EF. We found that EF exhibited miscible displacement behavior because the water-oil interface was invisible but not the gray gradient. Therefore, an advanced technique for miscible displacement image processing was developed for the first time to capture the fluid behavior at the pore scale. Fig. 4-3 shows the image processing workflow for EF. All the images were obtained using the open-source Fiji ImageJ software. The image processing workflow are as follows:

Step 1 – Remove noise: All raw images were filtered using the “remove dark/bright outliers” with the threshold = 50 and radius = 10 (see Fig. 4-3-(1), (2), (4), and (5)).

Step 2 – Obtain only particles: Only the solid phase was retained by removing the oil phase using the macro code in ImageJ software (Fig. 4-3-(3)).

Step 3 – Subtract particles: After dynamic injection, only the solid phase was subtracted, leaving the emulsion and oil phases in the pore space (Fig. 4-3-(6)).

Step 4 – Remove noise: Some high-level noise from particles appeared owing to the

particle subtraction error after Step 3. Therefore, macro codes were written to remove gray values  $< 12000$ . A Gaussian blur could be applied to remove additional noise and smooth the images (Fig. 4-3-(7) and (8)).

Step 5 – Calibration: Emulsion saturation as a function of the mean gray values exhibited a linear trend. According to this curve, the emulsion saturation with the mean gray values in the images were correlated (see Fig. 4-3-(9) and (10)).

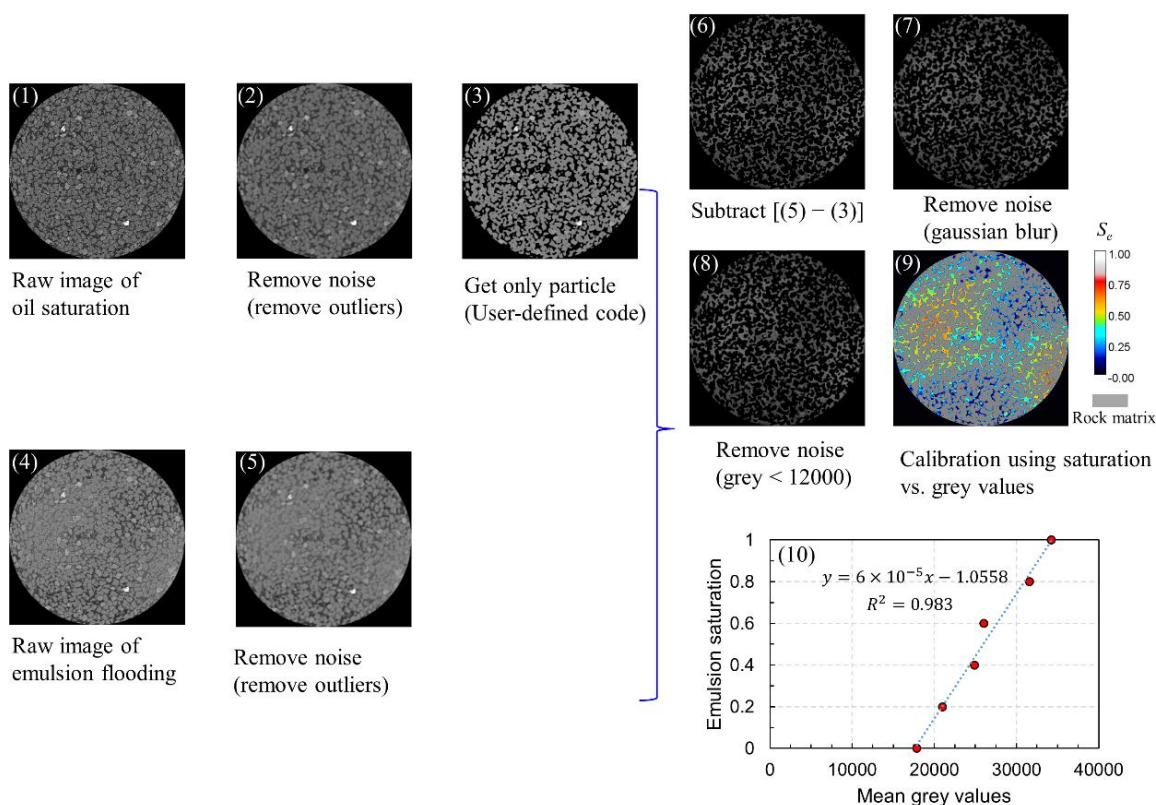


Fig. 4-3. Image processing workflow for emulsion flooding. The raw image of oil saturation (1) was filtered using “remove outliers” (2). Then, only porous media was obtained by a user-defined code (3). Raw image of emulsion flooding (4) was also filtered to “remove outliers” (5). Subtracting the image (5) and (3) yields the oil-emulsion phase in the pore space (6). Removing noise again to smooth the image (7–8). Finally, the saturation profile (9) was calibrated as a function of the gray values (10).

The image processing workflow as mentioned above is an advanced technique for miscible fluid system from a pore-scale view. For the supercritical  $\text{CO}_2$ -water or  $\text{CO}_2$ -oil system, we believe this technique could also be used for the visualization of miscible behavior by X-ray CT scanning. As such, flow behavior under supercritical condition can be discovered in 3D micro-scale pore spaces. However, this technique is very high-resolution which restricts the rock sample to a millimeter size. Nonetheless, it is critical to reveal some novel phenomenon to provide the fundamentals for industrial applications.

In the immiscible WF system, the water-oil-solid interface is clearly visible, indicating the three phases can be segmented through the histogram threshold method [18,24,88,94,144,145]. This is a classical phase segmentation procedure, by which the three

phases (water, oil, and solid) were classified according to their voxel assignment. Fig. A-B2 shows the segmentation procedure of the immiscible fluid system in detail (see Appendix B). The raw images were filtered using the nonlocal means algorithm. Then, we segmented (binarized) the solid and oil phases using Otsu's threshold method. Afterwards, the solid and oil phases can be combined using an image calculator; the water phase is also distinguished at this step. Finally, the three phases were reconstructed by rendering a color image. Readers interested in more details can refer to our previous research on image processing [18]. Once the segmentation was completed, a 3D object counter plugin was used to quantify information such as oil saturation, oil cluster volume, surface area, and Euler characteristics.

## 4.2 Results and discussion

### 4.2.1 Emulsion characteristics

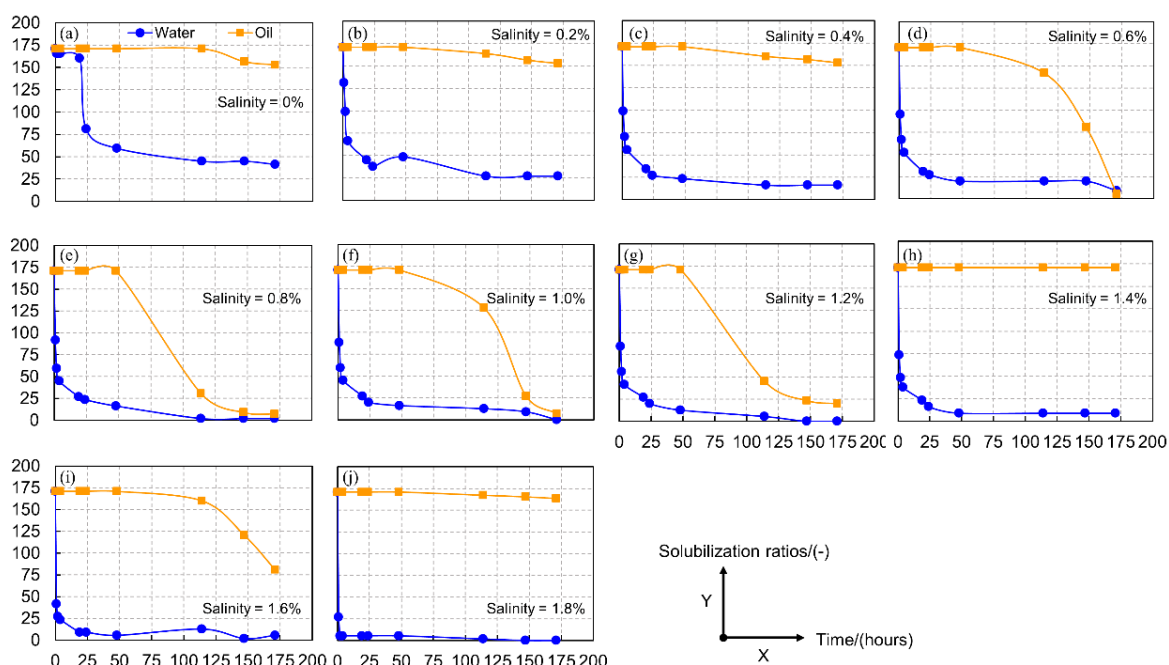
#### 1) Emulsion phase behavior

The emulsion stability is critical for oil recovery application [75]. Therefore, the emulsion stability as a function of NaCl salinity should be first evaluated using the phase behavior screen over time [146]. The photos of phase behavior can be found in Fig. A-B3 in Appendix B. From the color change of emulsion phase, we can roughly know the emulsion stability. If the color of emulsion is turbid, it means that the emulsion was well dispersed in either water or oil phase. In contrast, if the color is transparent, the emulsion is unstable because water or oil phase separates from the emulsion. The water/oil solubilization ratios ( $\sigma_w$  and  $\sigma_o$ ) are the important parameter to characterize the emulsion stability [146–148]. The water or oil solubilization ratio were described as the ratio of volume of water or oil solubilized into the emulsion (middle phase between the water and oil phases) per unit volume of surfactant. The calculated method can be found in previous reports for details [147,149]. As shown in Fig. 4-4(a)–(j), the water/oil solubilization ratios as a function of time for different salinities were calculated based on the screen images in Fig. A-B3. Initially, the fresh emulsion (0 hour) showed similarly high water and oil solubilization ratios (i.e., 171 mL/mL). After standing for few hours, the solubilization ratio of oil decreased slowly, whereas that of water decreased sharply. This indicated emulsion in oil phase was more stable than that in water phase. In Fig. A-B3, the color of emulsion in water changed from turbid to translucent and more transparent supported that water separated. The salinity level has a strong effect on the solubilization ratios. With the increasing salinity, the water solubilization ratio decreased much faster as a function of time and even approached zero as salinity exceeded 0.6%. By contrast, the oil solubilization ratio declined slowly and it presented obvious decreasing trend when the salinity exceeded 0.4%.

Fig. 4-4(k) shows the water/oil solubilization ratios extracted from one week of aging. It was observed that three stages of emulsion (i.e., stable, unstable and irregular status) appeared with increasing salinity. At low salinities of 0–0.4%, the emulsion phase was stable because oil and water solubilization ratios were high. There was no emulsion formation at the intermediate salinity of 0.6–1.2% because both oil and water solubilization ratios reached

zero. At high salinity of 1.4–1.8%, the emulsion status was unpredicted as the oil solubilization ratio presented strong fluctuation. Fig. A-B4 support that emulsion became unstable or irregular because of coalescence, namely the oil droplets merged to be larger (see Appendix B). Therefore, the most stable emulsion was obtained at a low salinity. In this study, we selected the emulsion without salinity for the subsequent core EF experiments because this status of emulsion was the most stable compared with that with salinities of 0.2% and 0.4%. Note that the fresh emulsions are injected since it still maintains stable within five hours (see Fig. 4-4(a)) at which the core-flooding experiments will be completed.

The dilution of chemicals (surfactant/co-surfactant) has a strong effect on the microemulsion phase behavior [150]. In the core-flooding experiments, the emulsions contact the connate brine in porous media which contains 4% NaI salt. Therefore, the emulsion stability may change with different diluted concentration of NaI. We estimated the maximum contact concentration of NaI was 1.0 wt.%. The phase behavior screen within 60 min is reasonable way to predict the emulsion stability in porous media because the connate brine was fully displaced within 60 min. A new phase behavior screen was designed to analyze the dilution emulsion stability as shown in Fig. A-B5 (Appendix B). Table. A-B1 shows the oil solubilization ratios were constant (i.e., 171 mL/mL) over time for different NaI concentration (see Appendix B). However, the water solubilization ratios decreased significantly when the time exceeded 60 min as shown in Fig. 4-4(l). Within 60min, it can be observed the water solubilization ratio changed slightly. Therefore, the emulsions in water phase were considered stable even if it contacted the brine for a short time.



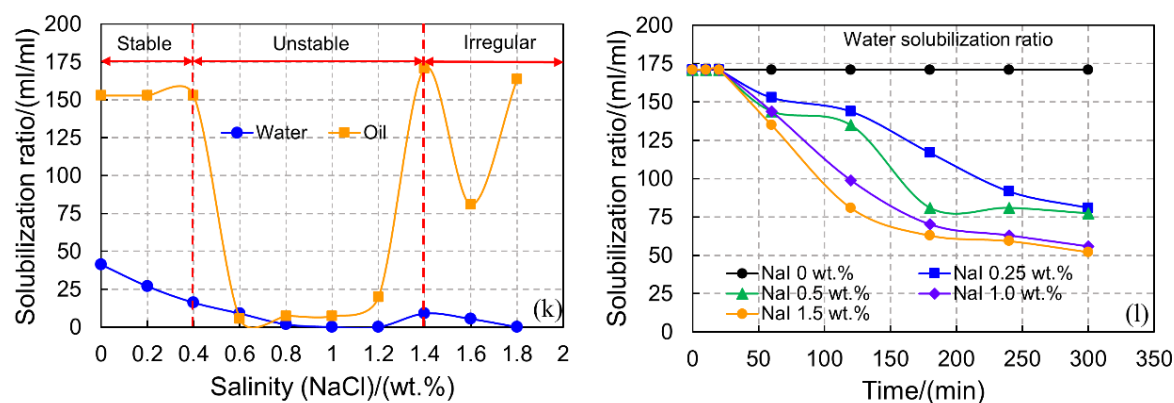


Fig. 4-4. Water/oil solubilization ratios as a function of time for (a)–(j) different salinities; final solubilization ratios at the final time of (a)–(j) are plotted in (k) sub-image; (l) water solubilization ratio as a function of time for different NaI diluted concentration are extracted from Fig. A-B5 in Appendix B. The water or oil solubilization ratios were described as the ratio of volume of water or oil solubilized into the emulsion (middle phase between the water and oil phases) per unit volume of surfactant.

## 2) Emulsion droplet size distribution

The optimum emulsion was transformed in a Petri dish and visualized under a microscope. The droplets were classified using the machine learning-based trainable WEKA. The size distribution of the emulsion droplets was plotted as shown in Fig. 4-5. It can be seen that the distribution curve shows good fit with the Gaussian distribution. The emulsion size ranged from 0 to 37  $\mu\text{m}$ , with one peak of 11  $\mu\text{m}$ , which supports the microscale emulsion. As mentioned, the core-flooding experiments will be finished within five hours at which the solubilization ratios of water and oil maintained 165~171 mL/mL (see Fig. 4-4(a)). Therefore, it is reasonably supposed that the emulsion is stable and oil droplet size may slightly change during this period.

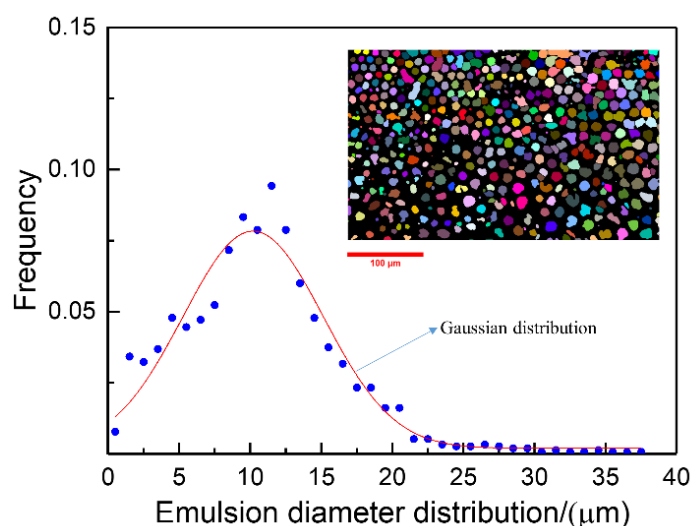


Fig. 4-5. Droplet diameter distribution of the most stable microemulsions. The inset is a visualization of the microemulsion under a microscope post-processing. The droplet segmentation used machine learning-based trainable WEKA. A total of 1550 emulsion droplets were collected for statistical analysis.

## 4.2.2 Wettability characterization

To confirm the success of the altered wettability on the sand surface after the chemical process, we measured the CA in situ using X-ray CT scanning, as shown in Fig. 4-6. In the water-wet porous media (Fig. 4-6(a)), the in situ CA was measured as  $\sim 42.1^\circ$  (Fig. 4-6(a)-(i)), which is slightly larger than the ex situ CA of  $\sim 30^\circ$  (Fig. 4-6(a)-(ii)), indicating strong water-wet wettability. The larger in situ CA may be attributed to the nonuniform exposure to plasma even though the sand surface turned over several times. For oil-wet porous media (Fig. 4-6(b)), the in situ CA was consistent with that in the ex situ measurement, approximately  $140^\circ$ . Therefore, plasma exposure and OTS coating altered the wettability to strong water-wet and oil-wet conditions, respectively, both of which showed good performance. In multiphase flow, the wettability order controls the fluid configurations in the pore space; that is, the most wetting phase tends to preferentially occupy small pores and throats, as well as the wetting films attached to the surface, whereas the most nonwetting phase tends to occupy the center of larger pores [36,41]. Theoretically, the different occupying behavior can attribute to the capillary pressure difference. The capillary pressure is controlled by the Young-Laplace equation as shown in Eq. (4-1). If the wettability is more water-wet, the CA decreases and capillary pressure for water phase increases. From Eq. (4-1), the pore radius of water occupying should be decreased, and oil phase resides in the larger pore center. Reversely, the more oil-wet will make capillary pressure more negative. The negative pressure will push oil to occupy the small size of pores and throats, leaving water phase stay in larger pore center. Fig. 4-6(a)-(iii-v) and (b)-(iii-v) shows 3D examples of oil occupying the pore space. In a water-wet system, oil as the most nonwetting phase preferentially occupies the center of large pores, whereas in an oil-wet system, oil as the most wetting phase tends to occupy small pores and throats. These examples provide visual evidence supporting the success of wettability alteration.

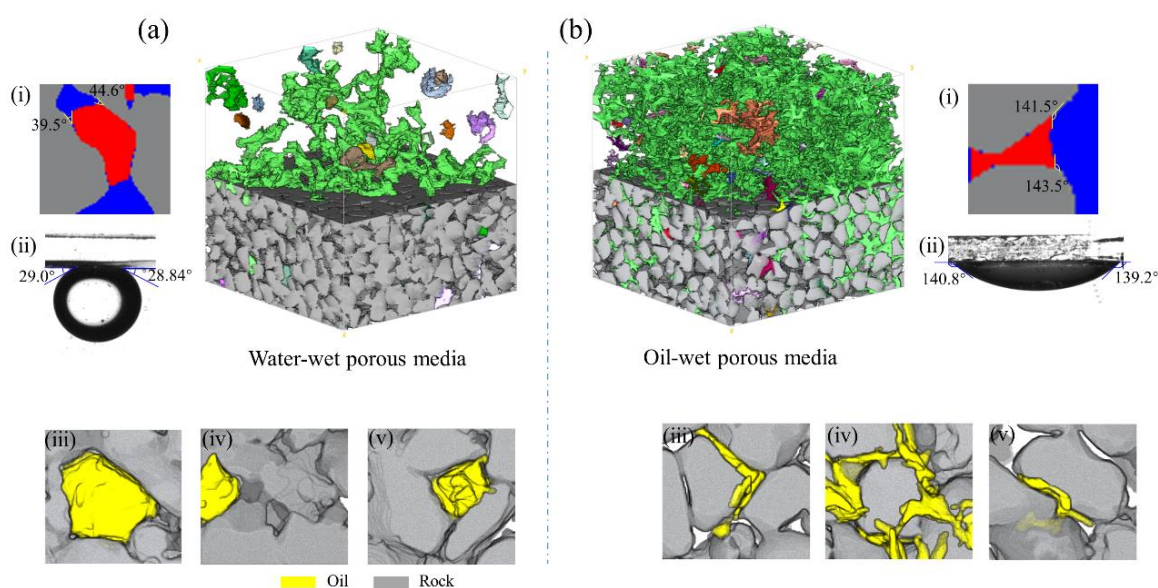


Fig. 4-6. In situ and ex situ measurements of oil-water contact angles on the rock surface after wettability alteration to (a) water-wet and (b) oil-wet. The images were obtained under steady-state flow conditions

with no change in the fluid configuration in the pore space. The sub-image (i) was measured in situ using X-ray CT scan (red, blue, and gray represent the oil, water, and sand surface, respectively); sub-image (ii) was measured ex situ by the sessile drop technique; sub-images (iii)–(v) are exemplary 3D visualizations of the oil phase in the pore space (yellow and gray represent the oil droplets and rocks, respectively).

### 4.2.3 Displacement behavior and performance

In this section, WF, EF, and their combination of WAE (i.e., EOR) were investigated in both water-wet and oil-wet reservoirs. Their performance in oil recovery was analyzed through pore-scale visualizations of dynamic displacement, residual oil saturation profiles, oil cluster morphology, and oil recovery efficiency. Moreover, a new EF mechanism was found to exhibit a similar miscible displacement behavior, which replenishes the conventional blockage mechanism reported in previous studies.

#### 1) Waterflooding in water-wet/oil-wet rocks

Fig. 4-7 shows the visualization of dynamic displacement front by WF in the 3D pore space of water-wet porous media. The center cross-sectional area was selected to better visualize the dynamic displacement front, as shown in Fig. 4-7(a). Initially, the oil phase was saturated and well-connected in the porous media. At 0.5–1.0 PV injection, the displacement front was nonuniform, and several viscous fingers were induced owing to the large viscosity difference between water and oil. After 1.0 PV injection, breakthrough occurred, and the residual oil was continuously flushed under shearing action. At 1.5–3.0 PV, the remaining oil phase stabilized and was bypassed by water, which fits well with the capillary desaturation curve [94]. Closeups of residual oil from the region of interest (ROI) revealed the 3D typical characteristics of displacement (Fig. 4-7(b)). The remaining oil phase was mobilized and gradually broken into many disconnected clusters with increasing injections. The smaller clusters were entrapped by capillary forces and could not be remobilized. The water-oil interface was clearly distinguished, indicating immiscible displacement behavior in WF. Therefore, the capillary forces cannot be ignored. The quantitative oil saturation profiles obtained from the 3D CT image slices (Fig. 4-7(a)) are shown in Fig. 4-9(a). At 0–1.5 PV, the residual oil saturation significantly decreased from the initial 0.67 to 0.08. At 2.0–3.0 PV, the oil saturation decreased by less than 3%, and reached a stable condition. In this wettability case, over 61% of the oil phase was recovered because the rock surface showed strong affinity to water, that is, water was the most wetting phase, thereby leading to imbibition displacement.

The displacement behavior of WF in oil-wet porous media is significantly different from that in water-wet porous media. Owing to the strong wetting to oil on the rock surface, water became most nonwetting phase that displaced the oil, resulting in drainage displacement. The visualization of the dynamic displacement behavior in oil-wet porous media is shown in Fig. 4-8. In Fig. 4-8(a), only one waterflow path was formed, and most of the residual oil in the pore space was bypassed by water. This could be attributed to the strongly negative capillary pressure in the pore space, in which the viscous force is unable to overcome the capillary force. Fig. 4-8(b) presents the 3D morphology of the residual oil from the ROI, which indicates that the oil phase was well-connected and difficult to remobilize. The



quantitative information on oil saturation is shown in Fig. 4-9(b). From the initial to 3 PV, the residual saturation decreased slightly from 0.67 to 0.62, which indicates that over 62% of the residual oil remained in the pore space. The apparent water-oil interface in the CT images supports the immiscible displacement of oil by water; therefore, negative capillary pressure dominated in this process. To eliminate the capillary pressure and improve oil recovery, the most promising method is miscible flooding, during which the water-oil interface is invisible in oil-wet porous media.

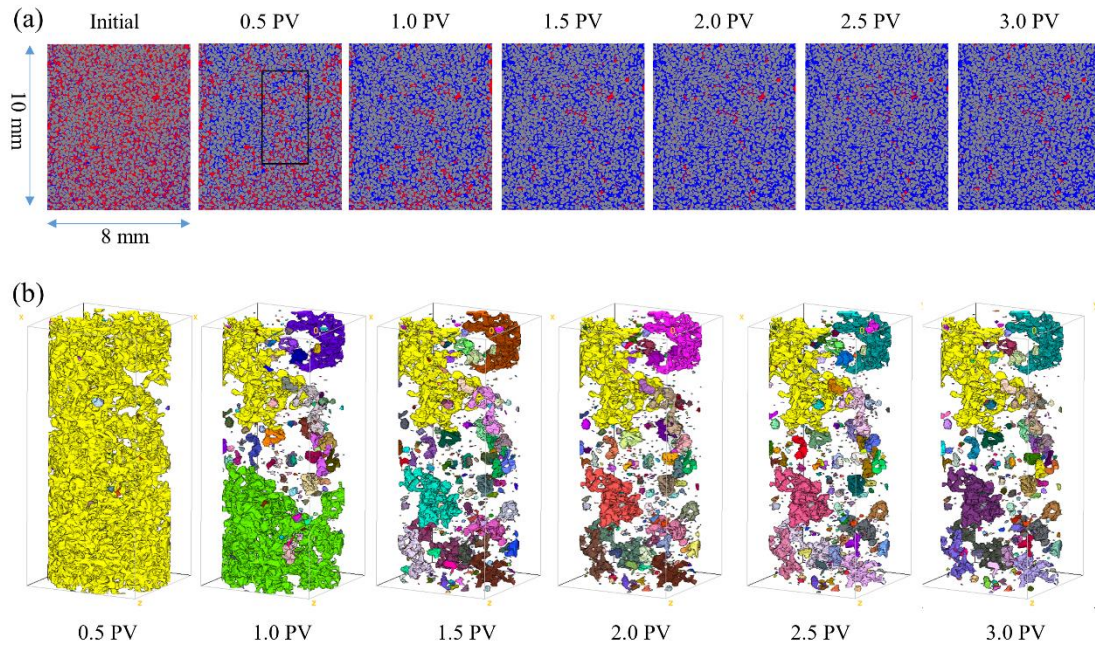


Fig. 4-7. 3D visualization of waterflooding in water-wet porous media. (a) Dynamic displacement front from the center cross-sectional area (red is oil, blue is water, and gray is solid). (b) Morphology of residual oil from the region of interest marked by the black rectangle in (a) (size:  $2.5 \times 2.5 \times 5.5$  mm, different colors represent disconnected clusters).

The capillary pressure in water-wet and oil-wet porous media can be estimated by the Young–Laplace equation (Eq. (4-1)). According to a previous test, the IFT is 12.6 mN/m; the average pore radius is 36  $\mu\text{m}$ , and the average CAs for water-wet and oil-wet porous media are  $30^\circ$  and  $140^\circ$ , respectively. Therefore, the capillary pressure for water-wet and oil-wet porous media is 1212 Pa (positive value) and -1072 Pa (negative value), respectively. A positive capillary pressure means that water will almost always have sufficient pressure to mobilize oil out of the pore space. In contrast, if the capillary pressure is negative, a higher water pressure is required to achieve the same oil saturation [151]. The relationship between the capillary pressure and saturation is shown by Eq. (4-2). The oil displacement behavior by WF in the water-wet and oil-wet porous media in this study agreed well with this relationship.

$$p_c = \frac{2\gamma\cos\theta}{r} \quad (4-1)$$

Where  $p_c$  is the capillary pressure,  $\gamma$  is the IFT between water and oil,  $r$  is the pore or throat

radius, and  $\theta$  is the CA.

$$p_o(S_w) = p_o(S_w) - p_w(S_w) \quad (4-2)$$

Where  $p_o$  and  $p_w$  represent the oil and water pressure, respectively; and  $S_w$  is the water saturation.

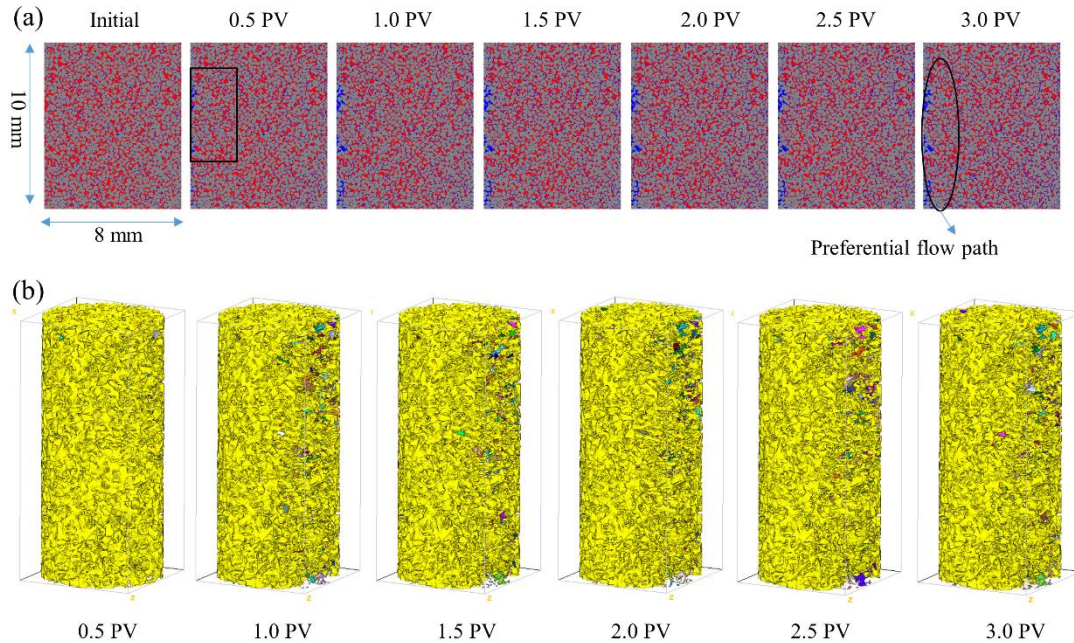


Fig. 4-8. 3D visualization of waterflooding in oil-wet porous media. (a) Dynamic displacement front from the center cross-section area (red is oil, blue is water, gray is solid). (b) Residual oil from region of interest marked by the black rectangle in (a) (size:  $2.5 \times 2.5 \times 5.5$  mm, different colors represent disconnected clusters).

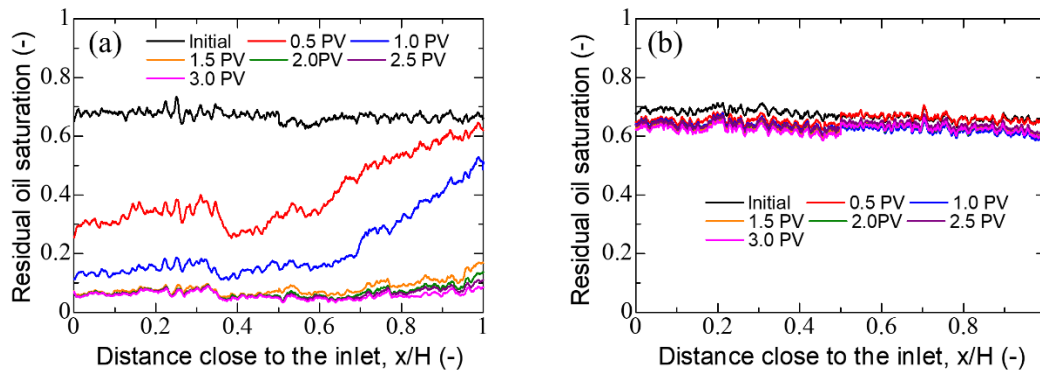


Fig. 4-9. Residual oil saturation profiles as a function of distance to the inlet in both (a) water-wet and (b) oil-wet (porous media after different injected PVs of waterflooding).

## 2) Emulsion flooding in water-wet/oil-wet rocks

Fig. 4-10 illustrates the pore-scale dynamic displacement of oil by direct microemulsion flooding in water-wet porous media. The center cross-sectional images show the displacement front during the continuous emulsion injection (Fig. 4-10(a)). The quantitative oil saturation was extracted, as shown in Fig. 4-12(a). Initially, the porous media was

saturated with oil, and the emulsion saturation ( $S_e$ ) was 0. When subjected to EF, two stages of displacement were observed in this process. The first stage is a fast invasion period (FIP); the second is a stable invasion period (SIP). Specifically, the FIP occurred at 0.5 PV injection of the microemulsion, during which the emulsion phase rapidly broke through the outlet. The image shows that the color of the oil changed from blue (0 PV) to a uniform green (0.5 PV), indicating that the oil phase in the pore space was uniformly removed by the areal sweeping mechanisms. At this point, the oil recovery reached a sweeping efficiency of 67%. After the FIP stage (i.e., 1.0–3.0 PV), the displacement front became increasingly stable, which marks the beginning of a new stage, i.e., the SIP stage. The images (1.0–3.0 PV) show that the color of oil at the top changed from green to dark red, which indicates that the trapped residual oil gradually solubilized into the emulsion phase. The gradient change in oil color implies that the emulsion dispersed into oil phase via mass transfer with aid of viscous forces which leading to miscible displacement behavior. Furthermore, viscous fingering was suppressed, leading to a stable displacement front. The saturation profile (Fig. 4-12(a)) shows that the residual oil saturation decreased from 0.62 to 0.015 during EF. The 30% original oil in place was recovered in the FIP stage, whereas an additional 30% was produced during the SIP stage. The residual oil saturation was  $\sim 1.5\%$ , much lower than that in WF of  $\sim 10\%$  at the end of 3.0 PV injection. In other words, the previously trapped oil that could not be invaded alone by WF was solubilized and removed by EF. The mechanism is the capillary forces were eliminated, resulting in a miscible displacement front at which the interface between the emulsion and oil became compositional gradient. The 3D remaining oil distribution was extracted from the ROI, as shown in Fig. 4-10(b). During the FIP stage, the residual oil phase remained well-connected. After entering the SIP stage, the oil clusters were segmented into many disconnected clusters and droplets behind the stable front. With continuous emulsion injection, most of the small oil clusters gradually dissolved and disappeared, resulting in higher oil recovery.

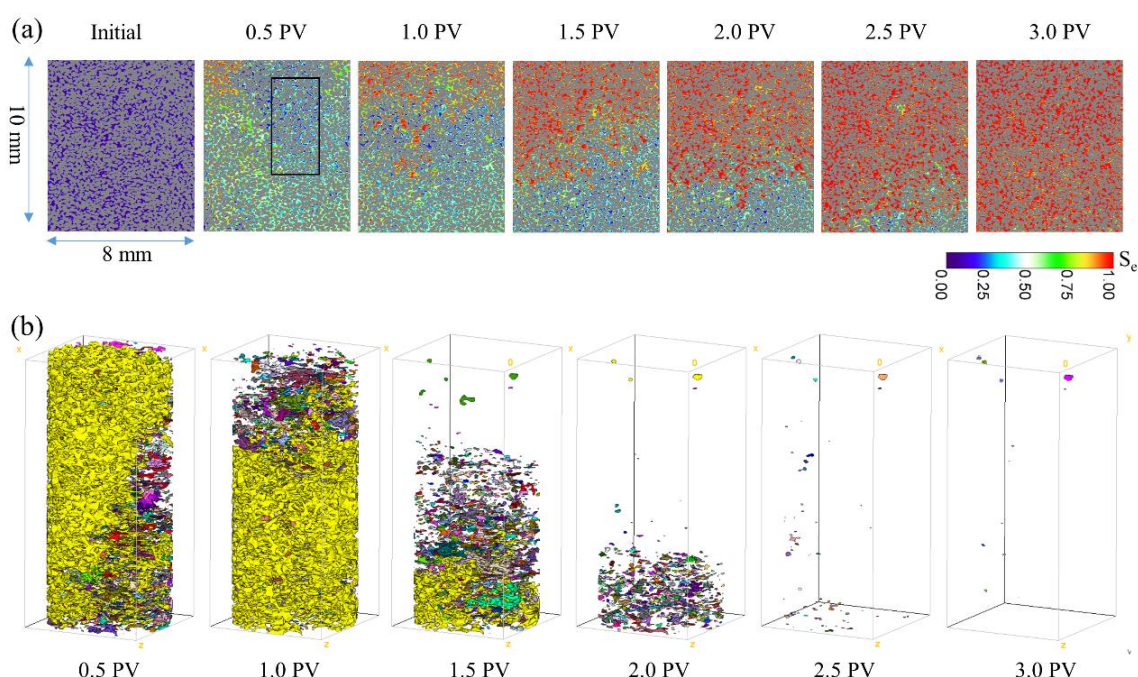


Fig. 4-10. 3D visualization of microemulsion flooding in water-wet porous media. (a) Dynamic displacement front from center cross-section area ( $S_e$  represents emulsion saturation). (b) Residual oil from the region of interest marked by the black rectangle in (a) (size:  $2.5 \times 2.5 \times 5.5$  mm, different colors represent disconnected clusters).

The 3D visualization of microemulsion flooding for oil recovery in strong oil-wet porous media is shown in Fig. 4-11. The residual oil saturation profile is shown in Fig. 4-12(b). Similar to EF in water-wet porous media, two stages, i.e., FIP and SIP, were also found in oil-wet porous media (see Fig. 4-11(a)). The FIP stage occurred at the 0.5 PV injection, and breakthrough rapidly developed. During this period, the oil saturation decreased from 0.62 to 0.34, and 28% of oil was recovered by uniform areal sweeping from the pore space. In the SIP stage, the uniform displacement front to the outlet rapidly developed, that is, the second breakthrough occurred between 1.5 and 2.0 PV. Behind the stable front, the gradient color indicates that the oil phase was gradually solubilized through emulsion dispersion into oil via mass transfer. After the second breakthrough (2.5–3.0 PV), the residual oil saturation tended to be stable ( $S_o = 0.1$ ), which means that additional oil was recovered at 22% in the SIP stage. The 3D visualization of oil clusters (Fig. 4-11(b)) shows that the remaining oil was in the form of disconnected clusters and droplets, in contrast to the oil-wet case of WF in which the oil phase was well-connected at the end of injection.

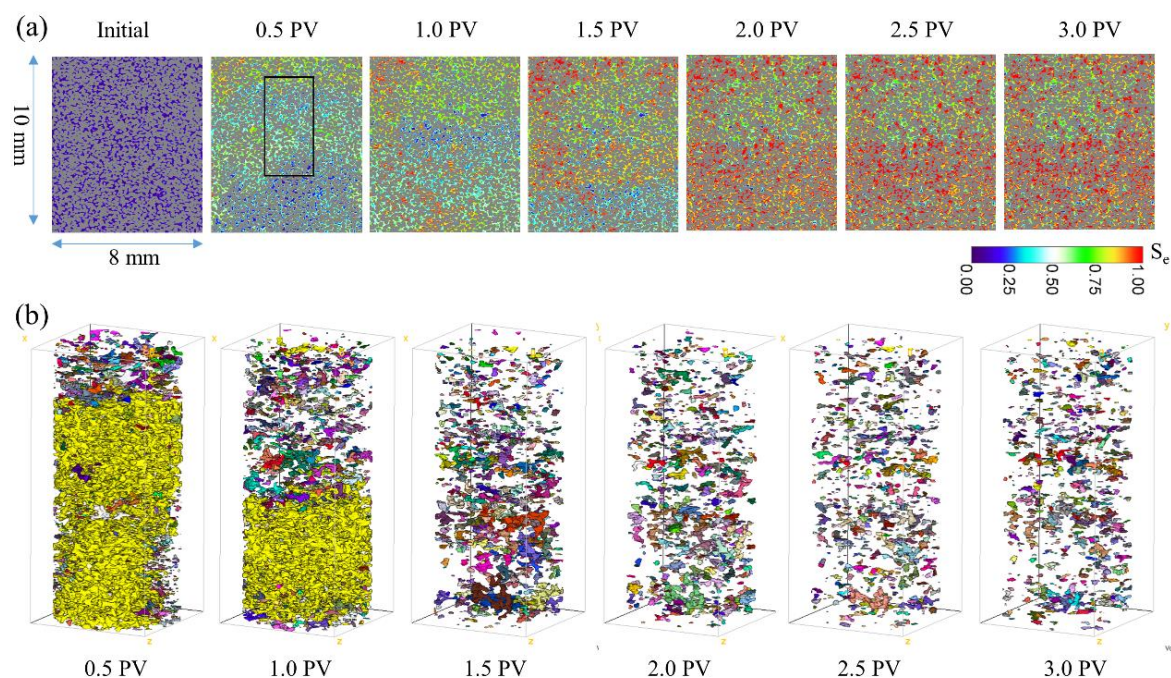


Fig. 4-11. 3D visualization of emulsion flooding of oil-wet porous media. (a) Dynamic displacement front from the center cross-section area ( $S_e$  represents emulsion saturation). (b) Residual oil from the region of interest marked by the black rectangle (size:  $2.5 \times 2.5 \times 5.5$  mm, different colors represent disconnected clusters).

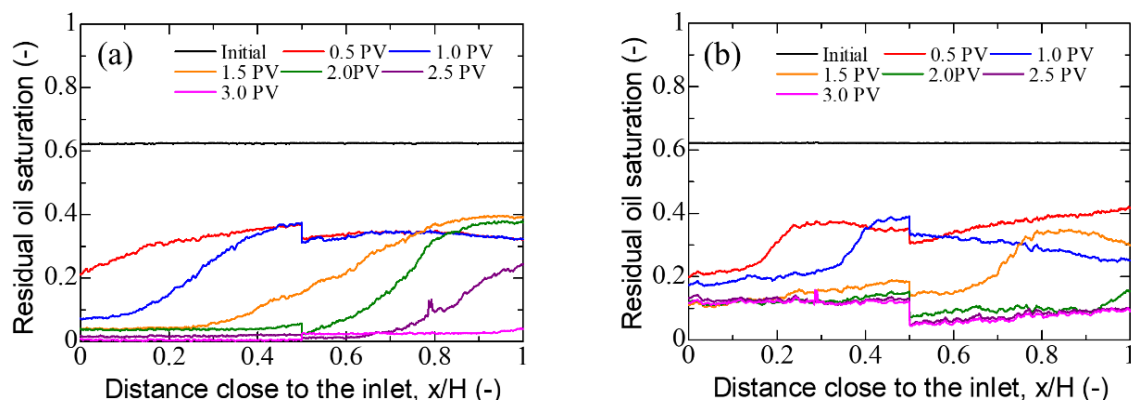


Fig. 4-12. Residual oil saturation profiles as a function of the distance to the inlet in both (a) water-wet and (b) oil-wet porous media after different injected PVs of microemulsion.

### 3) Quasi-miscible displacement mechanisms

As discussed above, EF can significantly improve oil recovery because it behaves as a miscible displacement behavior. The miscible behavior by EF is a novel discovery in the current 3D pore-scale experiments, which challenges the traditional blockage mechanism [72]. Fig. 4-13(b) presents visual evidence that there was no apparent interface between emulsion and oil phases, but it presents compositional gradients in the 3D pore space. Therefore, capillary forces can be eliminated during the flooding process. The compositional gradient indicates that oil removal was controlled by mass transfer between emulsion and oil phases. Namely, solvent-based emulsion dispersed into oil and oil was gradually dissolved into solvent emulsions at the same time. Note that only solvent droplets in the microemulsion flooding shows good miscibility (no interface) with crude oils, which can be captured by X-ray CT as shown in Fig. 4-13(b). However, the water phase inside the emulsion phase has a poor miscibility with crude oils that implies us the emulsion flooding in this study presents a quasi-miscible behavior, instead of a real miscible case at which there is not interface between any fluid at all. Fig. 4-13(c) illustrated this point from a molecular aspect. The interface between the solvent and oil is invisible whereas that between the water and oil still exists. In this figure, we can see that solvent emulsions changed from yellow to gray color, indicating the crude oils are dissolved into the solvent. Then, the dissolved oils and emulsions together flow out of the reservoirs under the shearing forces. Furthermore, the viscosity of crude oil was reduced significantly when the solvent emulsions dispersed into the crude oils. The viscous fingering may be restricted. WF was considered as the immiscible displacement behavior because the interface can be clearly distinguished in the pore space (Fig. 4-13(a)). Hence, capillary forces contribute negatively to oil removal. In general, the large viscosity contrast between miscible displacing and displaced fluids often causes viscous fingering [22]. However, in our study of the miscible system, viscous fingering was suppressed, resulting in a uniform and stable displacement front, as shown in Fig. 4-13(d). In other words, EF can improve the mobility ratio and provides good conformance control, which is consistent with the results reported in the literature [152]. These can be attributed mainly to the fact that the emulsion phase and oil phase share a

similar viscosity.

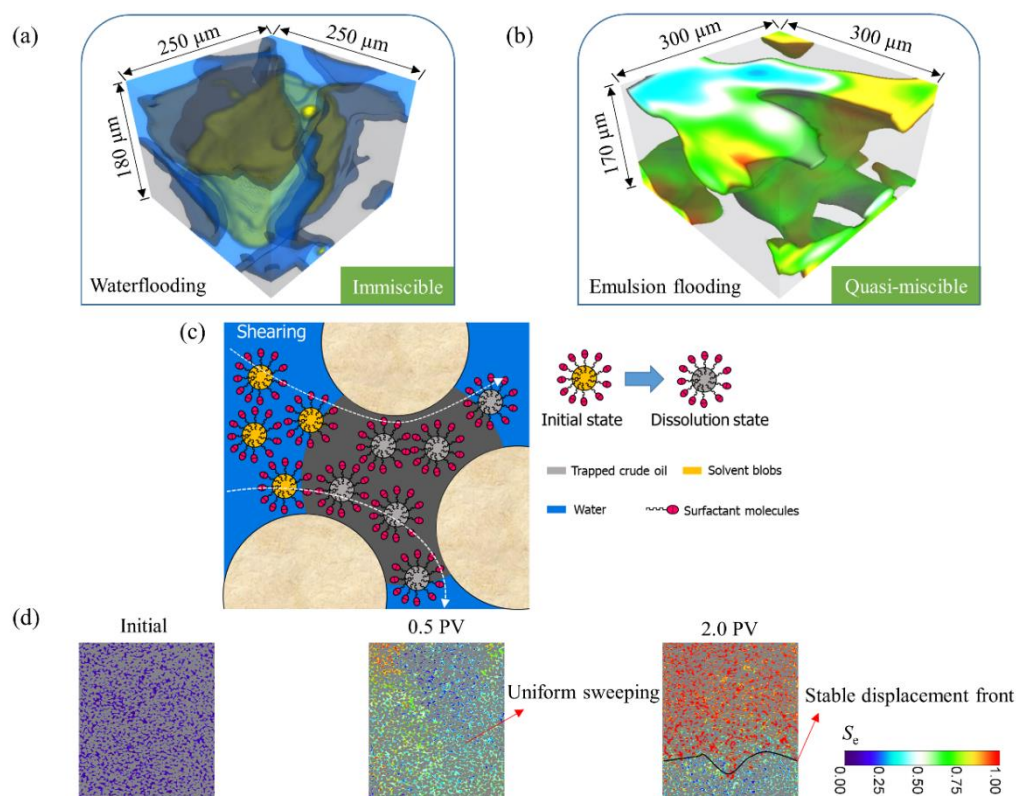


Fig. 4-13. Different mechanisms between waterflooding (WF, immiscible) and emulsion flooding (EF, quasi-miscible). (a) The water-oil interface was observed during WF. (b) There was no interface, but it presents compositional gradients in the 3D pore space during EF. (c) The oil was gradually solubilized into solvent emulsions during EF from a molecular view of aspect. (d) The viscous fingering in the miscible displacement process was suppressed owing to the similar viscosity between the microemulsion and oil phase.

#### 4) Oil cluster morphology and topology

In the previous sections, we found that EF is capable of displacing the oil phase through the miscible displacement front where oil is gradually solubilized, thereby improving oil recovery. The 3D visualization of the ROI shows that the size distribution of oil clusters varies between WF and EF. The wettability conditions also have a significant effect on the size distribution of oil clusters. In this section, we present a graphical and statistical analysis of the trapped-oil distribution after WF and EF under both water-wet and oil-wet conditions. Fig. 4-14 shows the oil cluster size distribution in the cumulative volume fraction (Fig. 4-14(a)) and the 3D visualization of exemplary oil clusters of different size level (Fig. 4-14(b)). After WF in water-wet porous media, the oil trapped in the pore space formed into disconnected clusters. The largest oil cluster volume was  $3 \times 10^8 \mu\text{m}^3$ , which accounted for 30% of the entire oil cluster volume. This result is consistent with the oil size level in Berea sandstone reported by Kuang et al. [101], in which strong water-wet conditions could create small oil clusters. However, the oil phase showed a strong connectivity in oil-wet porous media. The largest oil cluster volume reached  $5.60 \times 10^9 \mu\text{m}^3$ , accounting for 99% of the

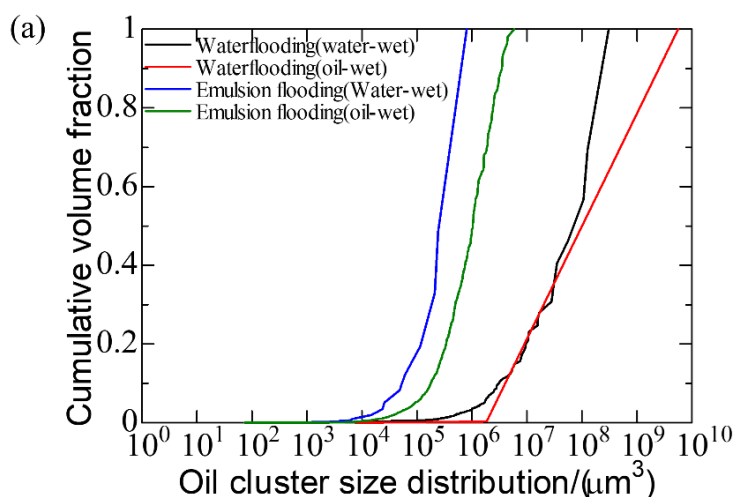
entire oil cluster volume and was an order of magnitude larger than that of the water-wet case. Fig. 4-14(a) shows that the distribution curve shifted to the right, indicating the significant increase in the size of the oil clusters. This behavior was attributed to the fact that the oil phase as the most wetting phase formed wetting layers on the rock surface, and preferentially occupied the smaller pores and throats. After the injection of the emulsion, the oil cluster volume became much smaller than that of WF in both water-wet and oil-wet porous media. For example, the distribution curves shifted to the left by approximately 2–3 orders of magnitude compared with that of WF. As shown in Fig. 4-14(b), the largest oil cluster volume in water-wet rock was  $8.02 \times 10^5 \mu\text{m}^3$ , while that in the oil-wet case was  $5.84 \times 10^6 \mu\text{m}^3$ , accounting for 50% and 2% of the total volume of oil clusters, respectively.

The topology of the oil clusters also showed great contrast during WF and EF in both water-wet and oil-wet porous media. In general, oil clusters can be classified into different patterns (e.g., network, branch, ganglia, and singlet) according to the two key parameters of sphericity ( $G$ ) and Euler characteristics ( $Eu$ ). The equations are expressed as Eqs. (4-3) and (4-4) [144]. Readers interested in the details of the specific classification range of the two parameters can refer to our previous study [18]. The 3D visualization of the ROI (Fig. 4-7(b), Fig. 4-8(b), Fig. 4-10(b), and Fig. 4-11(b)) shows that oil branches with loop-like structures dominate the WF in water-wet porous media, whereas in oil-wet porous media, the oil phase exhibited a well-connected network. In contrast, there was no loop-like structure in the trapped-oil configurations, but ganglia and/or singlets were observed after EF. Only singlets appeared in water-wet porous media, while both ganglia and singlets dominated in oil-wet porous media. This difference in topology indicates that the oil removal performance of EF is better in water-wet than in oil-wet porous media.

$$G = \frac{\pi^{1/3}(6V)^{2/3}}{A} \quad (4-3)$$

$$Eu = N - L + O \quad (4-4)$$

Where  $V$  is the single oil cluster volume,  $A$  is the surface area; and  $N$ ,  $L$ , and  $O$  are the number of isolated objects, redundant loops, and cavities, respectively.



(b)

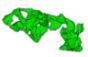

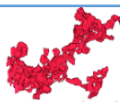
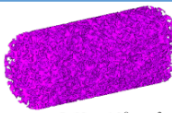




Size level (volume fraction)	2%	10%	30%	50%	99%
WF (water-wet)	 $2.80 \times 10^7 \mu\text{m}^3$	 $1.07 \times 10^8 \mu\text{m}^3$	 $3.06 \times 10^8 \mu\text{m}^3$	—	—
WF (oil-wet)	—	—	—	—	 $5.60 \times 10^9 \mu\text{m}^3$
EF (water-wet)	 $6.00 \times 10^4 \mu\text{m}^3$	 $2.43 \times 10^5 \mu\text{m}^3$	—	 $8.02 \times 10^5 \mu\text{m}^3$	—
EF (oil-wet)	 $5.84 \times 10^6 \mu\text{m}^3$	—	—	—	—

Fig. 4-14. (a) Oil cluster size distribution and (b) 3D visualization of exemplary oil clusters. All trapped-oil clusters were extracted at the end of 3.0 PV injection (stable condition).

#### 5) EOR scenarios in water-wet/oil-wet reservoirs

The previous section discussed the displacement performance of direct WF and EF to imitate the secondary oil recovery technique. The results showed that EF, as a similarly miscible displacement process, has the most potential for applications in oil recovery, and is even independent of the rock wettability (from water-wet to oil-wet). This section evaluates its application in EOR and its effectiveness in oil recovery using WAE flooding scenarios.

Fig. 4-15 presents the pore-scale visualization of the displacement behavior in EOR scenarios and quantitative residual oil saturation profiles of water-wet and oil-wet reservoirs. Initially, the porous media was saturated with oil ( $S_o \approx 0.7$ , connate water condition). After immiscible WF of 1.5 PV, the water-oil fluid configurations stabilized in the 3D pore space in both water-wet (Fig. 4-15(a)) and oil-wet (Fig. 4-15(b)) porous media. However, the oil cluster morphology showed significant differences such that residual oil was well-connected in the oil-wet case but existed in the form of separate small oil branches and singlets in the water-wet case. In addition, the residual oil saturation was 6% in the water-wet case (Fig. 4-15(c)), whereas in oil-wet porous media, it reached 64% (Fig. 4-15(d)). This result is consistent with the previous oil displacement performance by direct WF. After miscible EF, it was observed that EF was more effective in solubilizing well-connected large oil clusters instead of small oil ganglia and singlets. Specifically, most of the small oil ganglia and singlets were bypassed by the emulsion phase in water-wet porous media (areas marked as 1, 2, and 3 in Fig. 4-15(a) to show the examples). Even the larger oil branches were slightly solubilized, as shown in the closeups of area 1. Therefore, only 3% additional oil was recovered compared with WF. This may be attributed to the small contact area between the oil and emulsion phases that restricted the emulsion ability to solubilize the trapped oil. In contrast to the oil-wet reservoir, an advanced solubilization front was clearly observed,



indicating that the mass transfer was very strong in this front where oil phase was gradually solubilized during EF. It is noteworthy that the emulsion phase preferentially flowed along the previous water path in WF and expanded its sweeping area after the water phase was removed. At the final emulsion injection of 3.5 PV, over 50% additional oil was produced, which shows high oil recovery performance. Therefore, we concluded that EF can be applied in cases where the residual oil phase is a well-connected network. That means EF is the best choice for EOR in weakly or strongly oil-wet reservoirs or as a direct secondary oil recovery method.

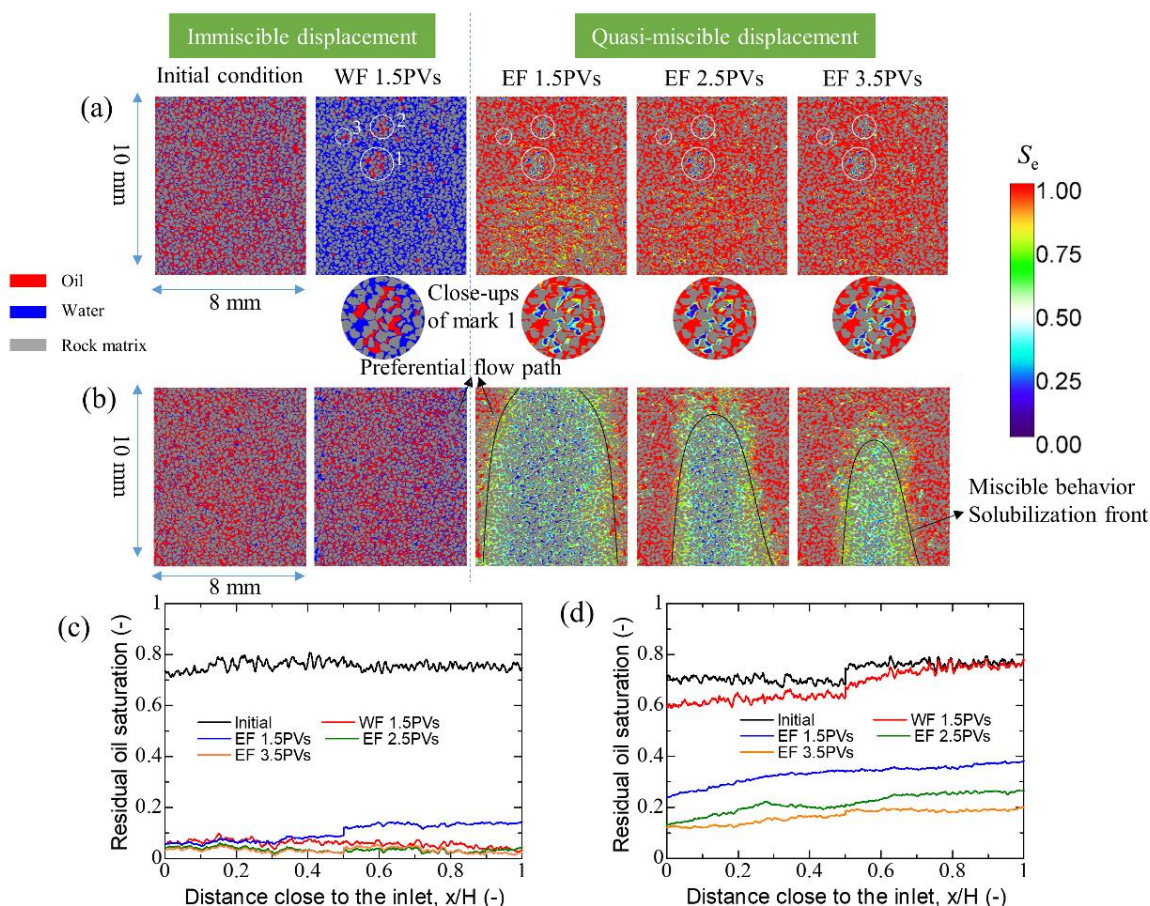


Fig. 4-15. Pore-scale visualization of displacement behavior in enhanced oil recovery scenarios in water-wet (a) and oil-wet (b) reservoirs. The quantitative residual oil saturation profiles are plotted in (c) and (d), respectively. For the immiscible cases (oil saturation and WF 1.5 PVs), the three phases of oil, water, and rock surface were well segmented and represented as red, blue and gray, respectively. For the miscible cases (EF 1.5–3.5 PVs), the CT gray images were calibrated, where dark blue indicates oil saturation of 1, while dark red indicates emulsion saturation of 1. The inset images in (a) are the closeups of the area marked as 1 in the dynamic displacement. The black line in (b) exhibits the evolution of the solubilization front during miscible EF.

#### 6) Oil recovery efficiency

Fig. 4-16 compares the amount of oil recovered under different wettability conditions by WF, EF, and the combination of both in EOR scenarios. The ultimate oil recovery for WF under the water-wet condition reached 91%, which is 82% higher than that under the oil-wet

condition. We repeated the same WF experiments until 1.5 PVs and applied EF to simulate the EOR method. The results showed that the final oil recovery only improved by 4% under the water-wet condition compared with direct WF. However, under the oil-wet condition, this performance was significantly higher, approaching 70%. Therefore, the EOR performance is poorer when applied in strong water-wet porous media. The EF has the greatest potential solubilization ability in well-connected oil clusters. In this case, direct EF could significantly improve oil recovery because oil clusters are an initially well-connected network. As expected, the plot indicated that the ultimate oil recovery with direct EF was very high, reaching 97% and 84% under water-wet and oil-wet conditions, respectively.

In summary, because of its miscible behavior, EF can be applied in secondary oil recovery technique regardless of the wettability of reservoirs, or in tertiary oil recovery technique in weakly/strongly oil-wet reservoirs, in which the oil phase is well-connected after WF.

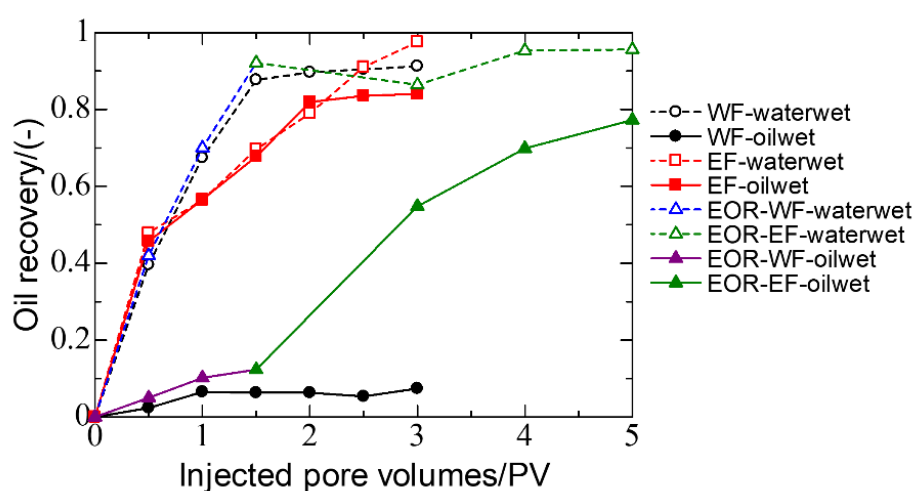


Fig. 4-16. Oil recovery efficiency of secondary (T1–T4) and tertiary (T5–T6) techniques as shown in Table 4-1.

### 4.3 Summary and suggestions

In this chapter, we first prepared a new type of solvent-based microemulsion and then the oil displacement performance of direct WF, EF, and the combination of both for EOR was investigated in both strongly water-wet (e.g., Berea sandstone) and oil-wet (e.g., carbonate rock) porous media. X-ray micro-CT was used to visualize the fluid-fluid configurations in 3D pore spaces. An advanced workflow for image processing was developed for the first time, which is applicable to any type of pore-scale miscible displacement behavior (e.g., solvent flooding,  $s\text{CO}_2$  injection, and microemulsion flooding in this study). After imaging and statistical analysis, our main conclusions are as follows:

(1) Solvent-based microemulsion flooding exhibited quasi-miscible displacement behavior/front in which mass transfer between oil phase and emulsion phase occurred which challenges the previous blockage mechanism. The emulsions dispersed into oil phase and oil was gradually solubilized by emulsion flushes via viscous forces in this front. An interface

between the emulsion and oil was not observed but it presents compositional gradient, hence, eliminating the capillary forces. In addition, the viscous fingering was significantly suppressed, indicating this new agent has a good control of stable displacement.

(2) Immiscible WF had very low oil recovery efficiency ~9% in strong oil-wet porous media. The residual oil was in the form of a well-connected network owing to the negative capillary forces. Compared with that in water-wet porous media, the oil recovery reached ~91%. Small oil branches and singlets dominated in the 3D pore space because of positive capillary forces. The size of residual oil clusters in oil-wet case shows one order of magnitude larger than that of the water-wet case. In contrast, miscible EF indicated that main oil topology consisted of smaller size of oil ganglia and/or singlets in either strong water-wet or oil-wet porous media, that is, the size of residual oil clusters in EF is reduced to approximately 2–3 orders of magnitude compared with that of WF. The oil recoveries both present highly efficient under water-wet and oil-wet conditions, reaching 97% and 84%. Therefore, direct EF showed high performance in oil removal regardless of the oil-acid concentrations and wettability of reservoirs because of eliminating capillary forces.

(3) Based on EOR scenarios, we found that EF could effectively solubilize large well-connected oil clusters in strongly oil-wet reservoir instead of small separate ones in strongly water-wet reservoir. For smaller separate oil clusters, only 4% oil recovery is enhanced, however, this performance could be improved to 70% for large well-connected oil clusters. Therefore, considering the solubilization ability, EF can be applied to secondary oil recovery regardless of the wettability of reservoirs, or to tertiary/enhanced oil recovery in weakly/strongly oil-wet reservoirs with a well-connected oil phase after WF. In addition, the solvent-based EF could reduce the half percent cost because only half percentage of solvent is used to prepare the flooding agent.

The main task of this chapter is to reveal the miscible behavior by a novel solvent-based microemulsion flooding. Unfortunately, the stability of microemulsion with high salinity was ignored. In the future, the emulsion stability in the high-salinity system will be optimized by considering various factors, such as surfactant types and amounts, temperature control, PH value adjusting, and nanoparticles assisted, etc. The emulsion size distribution over long periods (days to months) will be also observed to aid for the determination of emulsion stability. In addition, the surfactant retention and adsorption may have a negative effect on the emulsion content and stability. In this study, we assumed that there is no chromatographic separation of linoleic acid, surfactant and solvent in the dynamic flow in porous media. However, the emulsion may separate into its constituents as it flows through the porous media, which may be different from that in the tubing tests. The effluent analysis is a possible way to confirm the retention, adsorption and separation of chemicals [150,153]. Furthermore, the injection pressure may increase a lot due to the high viscosity of emulsion phase. The future works also need to confirm the pressure drop during this new agent.

## 5 Conclusions and suggestions

### 5.1 Conclusions

Throughout this work, various C-EOR methods were optimized step by step for improving the acidic oil recovery. The interfacial properties, microscopic displacement mechanisms and oil recovery efficiency were used to evaluate the performances of these methods using X-ray micro-CT scanning. First, the performances of traditional surfactant and alkaline flooding were compared, and their underlying mechanisms were obtained. Afterwards, one method with weaker performance was optimized by improving its mechanism. After that, the other method with higher performance was applied for different acid oil reservoirs to examine the effect of acid concentrations on its performance. The optimal acid concentration was obtained with respect to the best performance. Finally, a novel C-EOR method was created to apply for the other concentrations of oil reservoirs. It has been proved that the new method introduced some extraordinary advantages and could be applied for any type of oil reservoirs regardless of oil-acid concentration. The key conclusions are summarized as follows:

In [Chapter 2](#), the comparative performances and mechanisms of traditional surfactant and alkaline flooding were investigated. We found that the emulsification ability of alkaline flooding is much stronger than that of surfactant flooding, leading to the significant improvement of oil recovery. The effectiveness of surfactant transport to the water–oil interface is responsible for the performance differences. For surfactant flooding, the surfactant molecules are transported to the interface by convection, which is a time-dependent and slow process. By contrast, the alkaline flooding relies on the quick process of chemical-produced surfactant at the interface. In addition, the strong emulsification could increase the chemical contact area and strengthen the convection flow, which again promotes the effective transport of surfactant to the interface. To optimize the surfactant flooding, we introduced a novel cationic surfactant (i.e., STAC) that could physically adsorb the acid components of oil to form a dual-surfactant system. Consequently, the surfactant transport to the interface became more quicker because the fast accumulation of surfactant aggregates.

In [Chapter 3](#), the effect of oil acid concentrations on the performance of alkaline flooding was investigated. As suggested in the results, the oil recovery efficiency increases with increasing oil acid concentrations because of stronger emulsification ability. As the emulsification becomes stronger, the viscous fingering is gradually suppressed, and oil displacement front became more stable. The complete emulsification occurs in the high acid concentration at which large oil clusters are completely emulsified into tiny-size oil droplets. As a result, an entrained flow happens because these tiny droplets could entrain in the aqueous phase and easily pass through the pore spaces. Therefore, the strong emulsification has a good control of stable displacement and characteristic of entrained flow. As an optimal

scenario for engineering, the alkaline flooding was suggested to be applied for the high-acid oil reservoirs. For these low-acid oil reservoirs, the emulsification is not strong enough, and capillary forces still dominate, which hinders the improvement of oil recovery. Hence, it is needed to consider a novel method that maintains the stable displacement control and eliminates the capillary forces at the same time.

In [Chapter 4](#), we created a novel solvent-based microemulsion flooding for low-acid oil recovery. The emulsion flooding was selected because of its good control for stable displacement. The solvent was used to prepare the emulsions due to its miscible behavior, which has an ability to eliminate the capillary forces. In addition, the solvent-based emulsion could reduce half percentage of solvent use, thereby significantly decreasing the cost. The performance of this new chemical agent was examined through the pore-scale detection using a micro-CT scanning. As shown in the results, the oil recovery was significantly improved (approaching 100%) regardless of oil acid concentrations. For one reason, the oil displacement by the emulsion flooding is uniform, namely viscous fingering is avoided, thereby leading to the increasing areal sweeping efficiency. For another reason, the solvent-based microemulsion flooding exhibits a quasi-miscible displacement behavior. The capillary forces can be eliminated because the interface is not visible, but it presents a compositional gradient. Therefore, the oil recovery mechanism is controlled by the mass transfer that the solvent disperses into oils and oils are gradually dissolved into the solvent at the same time. The dissolved oil could entrain in the emulsion solution and flow out of oil reservoirs. We concluded the solvent-based emulsion flooding has the best performance and can be applied for any type of acid oil reservoirs.

For petroleum-engineering suggestions, the solvent-based microemulsion flooding is more expensive than that of traditional surfactant and alkaline flooding. Considering the cost, the alkaline flooding is suggested to apply for a high-acid oil reservoir. For a low-acid oil reservoir, the novel cationic surfactant is recommended since it could adsorb the acid components to formulate a dual-surfactant system and work more effectively than a single surfactant alone. For a non-acid oil reservoir, the solvent-based microemulsion flooding shows the best performance because of eliminating the capillary forces. If we care more about the oil production instead of the cost, the solvent-based microemulsion is highly recommended because it can produce the oil recovery efficiency approaching 100%. In the future, if an energy crisis occurs, we have to increase the oil production to meet the world energy supply regardless of the cost.

## 5.2 Suggestions for future works

Throughout this work, we optimize the traditional C-EOR methods and create a novel method to improving the acidic oil recovery. Their oil recovery mechanisms were analyzed well based on the pore-scale visualization using the micro-CT scanning. However, there are some gaps identified in these new findings and can be extended as the potential future works.

In [Chapter 2](#), we introduced a novel cationic surfactant (i.e., STAC surfactant) to promote

the fast surfactant transport to the water–oil interface through the mechanism of physical adsorption. However, its application for acid oil recovery was not investigated to examine its superior performance over that of old surfactant. In the future, it is needed to continue this work.

In [Chapter 2](#) and [Chapter 3](#), we found the STAC surfactant and alkaline flooding are both strongly dependent on the oil-acid concentration. The effect of acid concentration on the performance of STAC surfactant needs more investigation. In addition, the comparative performances of surfactant produced by physical adsorption (i.e., STAC flooding) and chemical reaction (i.e., AF) also need to be continued in the future, which will provide a strong aid for the optimal selection of C-EOR scenarios.

In [Chapter 4](#), the stability of microemulsion with high salinity was ignored. However, some oil reservoirs contain high salinity in nature. Therefore, the emulsion stability is critical for these oil recovery applications. In the future, the emulsion stability in the high-salinity system will be optimized by considering various factors, such as surfactant types and amounts, temperature control, PH value adjusting, and nanoparticles assisted, etc. The emulsion size distribution over long periods (days to months) will be also observed to aid for the determination of emulsion stability. In addition, the surfactant retention and adsorption may have a negative effect on the emulsion content and stability. Furthermore, the emulsion may separate into its constituents as it flows through the porous media, which may be different from that in the tubing tests. The effluent analysis is a possible way to confirm the retention, adsorption and separation of chemicals. The injection pressure may increase a lot due to the high viscosity of emulsion phase. The future works also need to confirm the pressure drop during this new type of solvent-based microemulsion flooding. To continuously reduce the cost for the emulsion preparation, the solvent ratio can be reduced from 50% to 10% and at the same time, the water ratio is increased to 50% to 90%. However, whether the performance of miscible behavior and high oil recovery efficiency changes or not is still not clear and need to be confirmed in the future work.

## Appendix (supplementary material)

### Appendix A

#### A.1 Image processing

This study collected all image-based data by means of camera snapshotting and X-ray CT scanning. Therefore, all quantitative information (including area, perimeter, volume, saturation, etc.) was extracted from images based on the ImageJ software platform (National Institutes of Health). For each experimental test, the image processing methods are listed as follows:

##### 1) Microchannel test (2D)

It is observed that the oil shape frequently changed due to the interfacial instability in the microchannel. Therefore, the deformation number ( $D$ ) as expressed in Eq. (A-A1) was used to describe the deformed oil shape quantitatively [154]. First, the raw color images were split into three groups of red, green, and blue images. The blue images showed great contrast between the water and oil phase in the microchannel and, therefore, were selected for subsequent data analysis. After that, the image noise was removed using the non-local means algorithm. The oil phase was binarized using the histogram threshold method. In the end, the oil area and perimeter were obtained by executing an Analyze Particle Plugin.

$$D = \frac{P}{\sqrt{\pi \cdot A}} \quad (\text{A-A1})$$

Where  $P$  and  $A$  are the perimeter and area of oil individuals, respectively.

##### 2) Porous media test (3D)

Pore-scale experiment enables us to observe the oil and water occupancies in the 3D pore space. In other words, the oil deformation phenomenon can be monitored through direct visualization of oil shape changes. Fig. A-A1 shows the segmentation workflow of water, oil, and solid phases. The raw images were first filtered to remove noise using the non-local means algorithm. After noise removal, the porous media and oil phase were segmented using Otsu's threshold method [88,113]. Finally, the water, oil, and solid phases were combined and rendered in one image. One can refer to our previous study for details about this segmentation method [18]. We observed that the oil deformation resulted in substantial missing or new-appeared oil parts in the pore space when the time increased. As shown in Fig. A-A2, we successfully separated the disappeared and new-appeared oil parts through the image subtraction function. To be more specific, the residual oil shape was considered as an initial state (0 min) once the sample was flooded by the STAC solution (0 min). The disappeared oil parts were obtained when the residual oil in 0 min subtract that in other time (5–60min). The new-appeared oil parts were obtained using a reverse subtraction. Note that image subtraction was carried out after oil segmentation using Otsu's threshold.

Subsequently, the quantitative information about the volume changes was extracted using 3D Object Counter and MorphoLibJ Plugins [18,113].

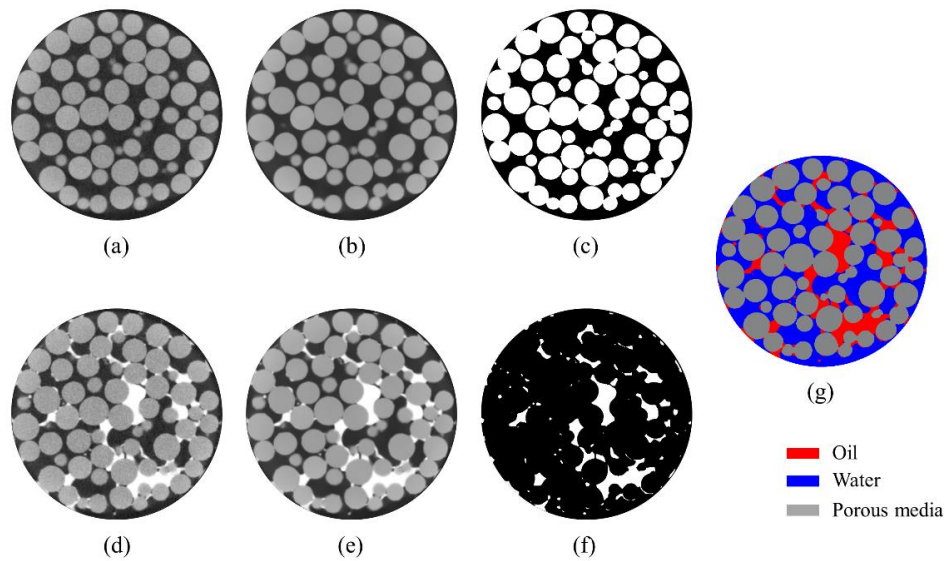


Fig. A-A1. Image processing workflow for three-phase segmentation and rendering of water, oil, and solid. Upper images (a) ~ (c) represent the porous media (reference image), and lower images (d) ~ (f) are the residual oil phase in the pore space after chemical flooding. The raw images [(a) and (d)] were filtered to remove noise using the non-local means algorithm [(b) and (e)]. After noise removal, the binary images of solid (c) and oil phase (f) were obtained using Otsu's threshold method, respectively. Finally, the water, oil, and solid phases were combined and rendered in one image (g).

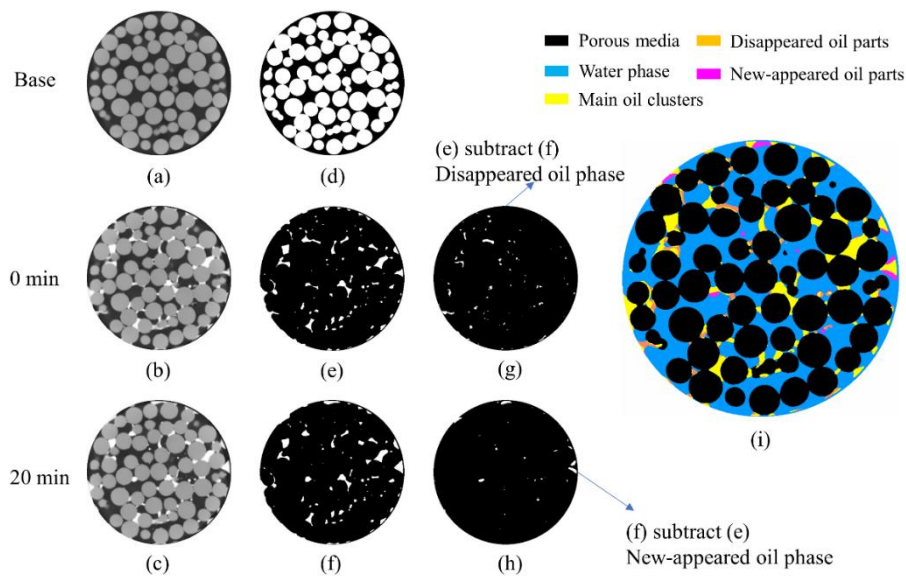


Fig. A-A2. Image processing workflow to obtain the disappeared and new-appeared oil parts. (a) represents the porous media as a base image; (b) and (c) are the residual oil phase in 0 min and 20 min after chemical flooding. All raw images [(a) ~ (c)] are filtered with a non-local means algorithm. After that, solid (d) or residual oil [(e) and (f)] phases are segmented using Otsu's threshold method. The disappeared oil parts (g) were obtained when the residual oil in 0 min subtracts that in 20 min. The new-appeared oil parts (h) were obtained using reverse subtraction. Image (i) illustrated all the solid,



water, and deformed oil phases in the sample.

## A.2 Different flow rates in microchannel

Time-series snapshotting images of the flow patterns under different flow rates of STAC flooding are shown in Fig. A-A3. Based on those images, we discovered that the interface deformed once the STAC solution established contact with the oil phase, which resulted in a meniscus shape different from that in pure water flooding (Fig. A-A4). In other words, the STAC solution always invaded the oil phase along the curved route. Meanwhile, the surfactant aggregates began to accumulate along the curved interface between the aqueous and oil phases. As expected, oil blebs appeared, which agreed well with the blebbing model in the static mode [64]. However, a new relationship was discovered, where surfactant aggregation was associated closely with the invading velocity in the dynamic mode. Consequently, the flow pattern varied with the flow rate. At a flow rate of 1  $\mu\text{L}/\text{min}$  (Fig. A-A3(a)), the oil shape changed frequently, indicating that the invading flow path changed direction simultaneously. In this case, oil blebbing dominated the low-flow-rate region. Additionally, no snap-off oil droplets were observed as the oil clusters passed through the constricted channel. As the flow rate increased to 10  $\mu\text{L}/\text{min}$  (Fig. A-A3(b)), changes in the oil shape and the snap-off phenomenon were both observed. The oil phase was segregated into small droplets by the snap-off action in constricted channel. At a high flow rate of 50  $\mu\text{L}/\text{min}$  (Fig. A-A3(c)), oil splitting was intensive when the droplets passed through the constricted channel, which implies that the shearing forces dominated in this region. The change in the oil shape was restrained by the shearing forces. It is noted that we observed the oil splitting also occurred besides the constricted channel during all flow rates, which means the new surfactant presented similar emulsification ability with that of AF.

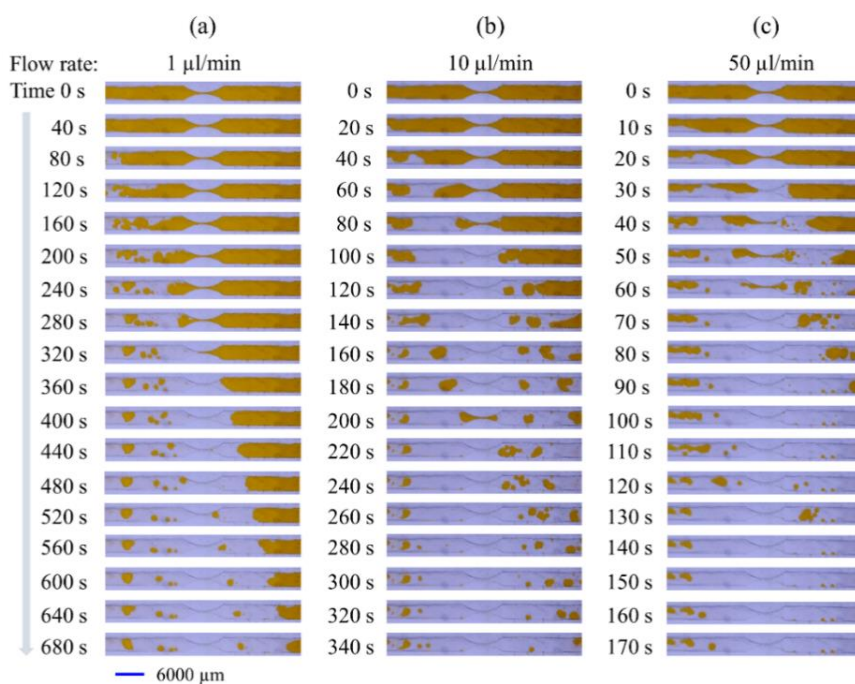


Fig. A-A3. Time-lapse photography of STAC chemical solution displacing acidic oil phase in

microchannel for different flow rates: (a) 1  $\mu\text{L}/\text{min}$ ; (b) 10  $\mu\text{L}/\text{min}$ ; (c) 50  $\mu\text{L}/\text{min}$ .

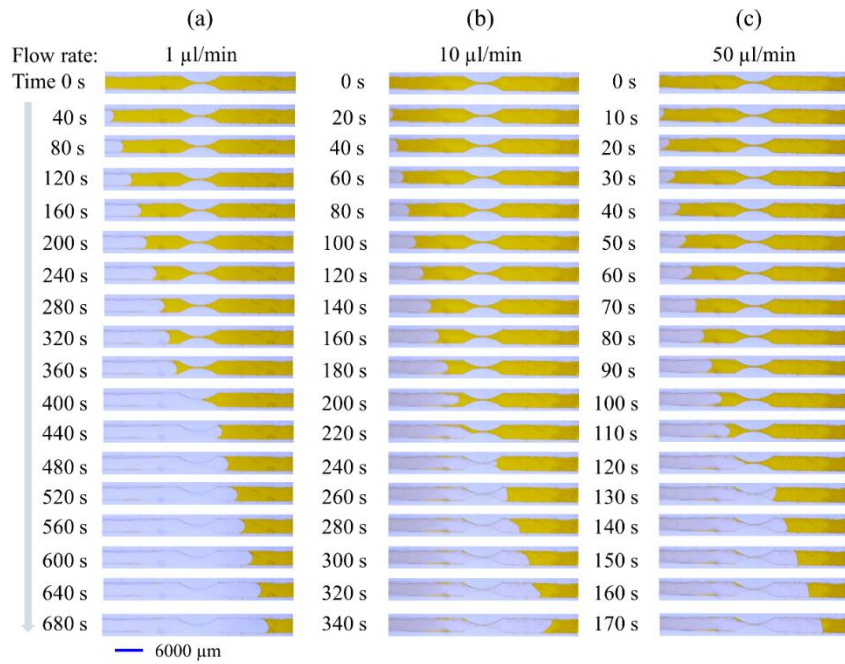


Fig. A-A4. Time-lapse photography of the pure water (STAC0) displacing the acidic oil phase (PA20) in the microchannel for different flow rates of 1  $\mu\text{L}/\text{min}$  (a), 10  $\mu\text{L}/\text{min}$  (b), and 50  $\mu\text{L}/\text{min}$  (c). The pure water injection is a reference to Fig. A-A3 in which the STAC solution was used instead.

## Appendix B

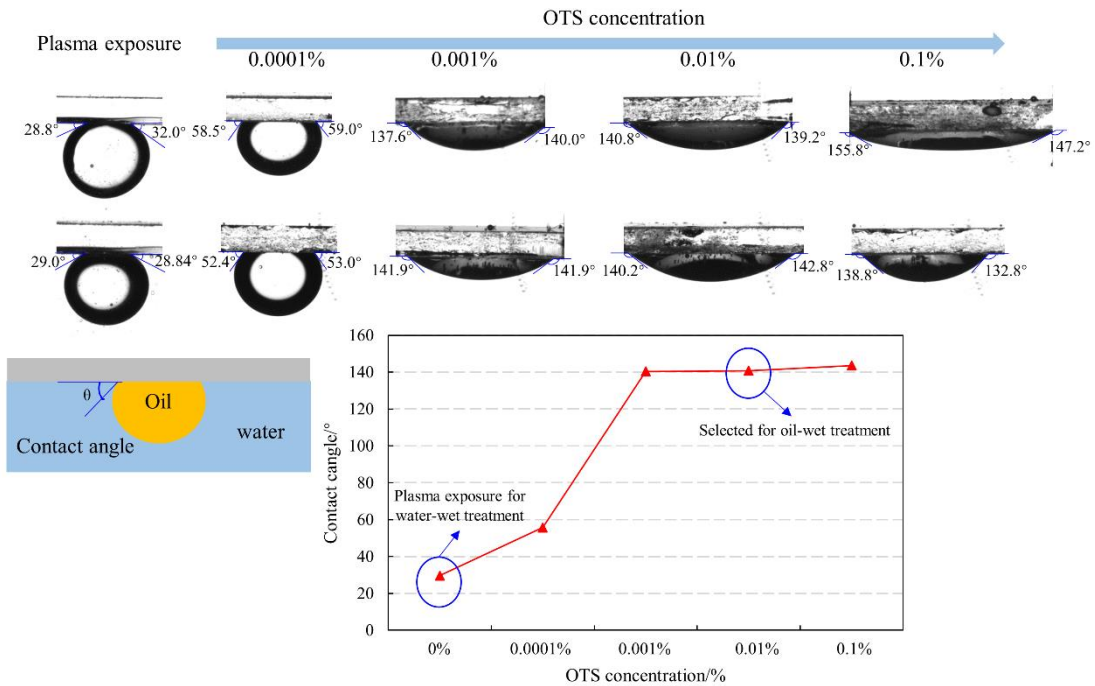


Fig. A-B1. Result of contact angle (CA) measurements after different processing protocols. The CAs were measured by the sessile drop technique in which oil was dropped on the surface of a glass slide ( $\text{SiO}_2$ -based material).

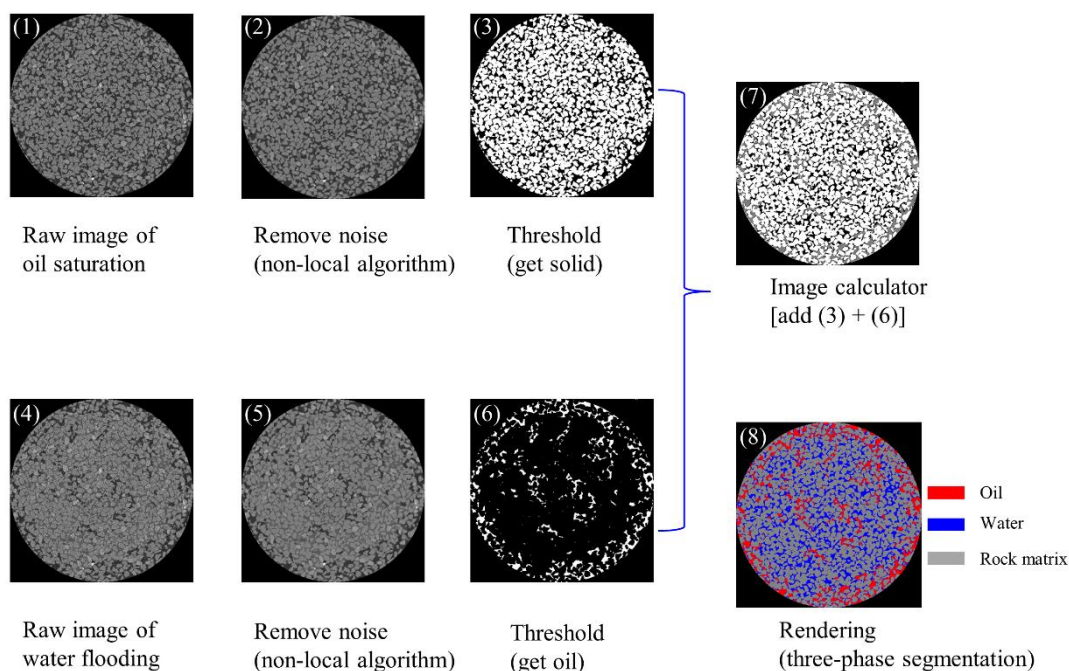


Fig. A-B2. Image processing workflow in immiscible flooding. All raw images [(1) and (4)] were filtered to remove noise using the nonlocal means algorithm [(2) and (5)]. The solid and oil phases were segmented using Otsu's threshold method [(3) and (6)]. The oil and water phases were added to the pore space using the image calculator (7) and colored by rendering (8).

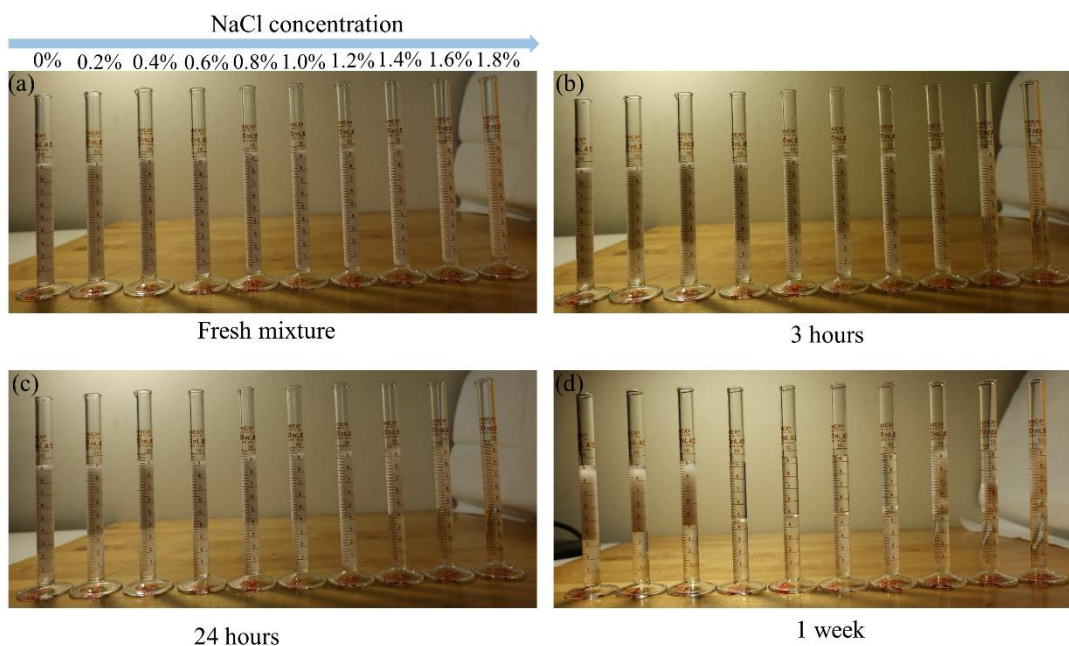


Fig. A-B3. Photos of emulsion phase behavior as a function of salinities at (a) initial time, (b) 3 h, (c) 24 h, and (d) one week. The turbid color indicates the emulsion phase. The transparent color at the top and bottom represents the oil and water phases, respectively.

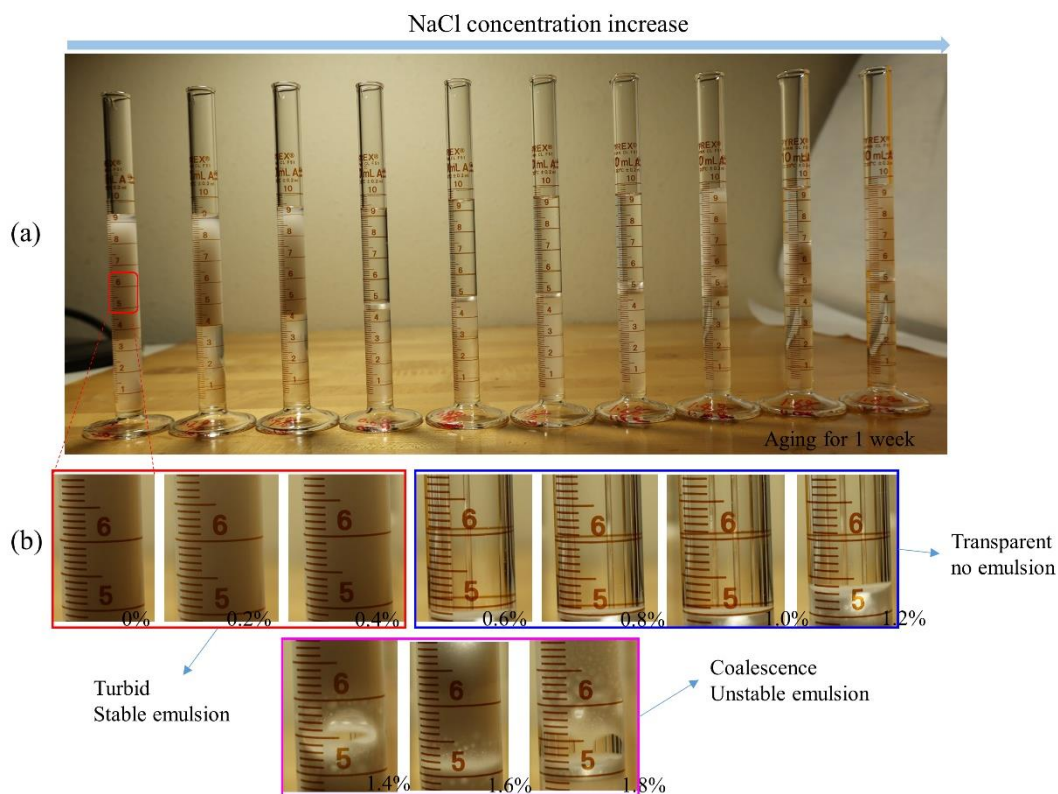


Fig. A-B4. Magnified visualization of emulsion stability behavior after one week (168 h).

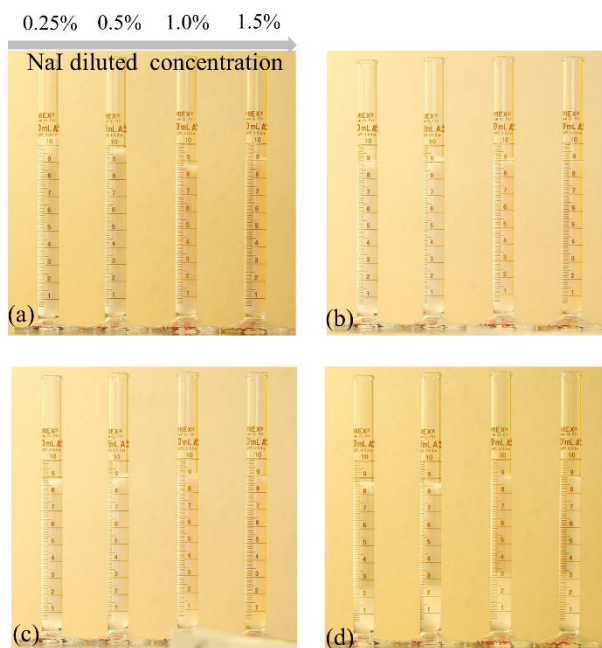


Fig. A-B5. Emulsion phase behavior screen for different NaI diluted concentration at time of (a) 0, (b) 30, (c) 60, and (d) 300 min.

Table. A-B1. Solubilization ratios of water or oil phase as a function of time for different NaI diluted concentrations.

NaI salinity	0%		0.25%		0.5%		1.0%		1.5%	
Time/min	$\sigma_w$	$\sigma_o$	$\sigma_w$	$\sigma_o$	$\sigma_w$	$\sigma_o$	$\sigma_w$	$\sigma_o$	$\sigma_w$	$\sigma_o$
0	171	171	171	171	171	171	171	171	171	171
10	171	171	171	171	171	171	171	171	171	171
20	171	171	171	171	171	171	171	171	171	171
60	171	171	153	171	144	171	144	171	135	171
120	171	171	144	171	135	171	99	171	81	171
180	171	171	117	171	81	171	70	171	63	171
240	171	171	92	171	81	171	63	171	59	171
300	171	171	81	171	77	171	56	171	52	171

Note:  $\sigma_w$  and  $\sigma_o$  represent water and oil solubilization ratios, respectively; Unit: mL/mL

## Reference

- [1] B.P. Tissot, D.H. Welte, Petroleum Formation and Occurrence, Springer-Verlag, Berlin Heidelberg, New York, Tokyo, 1984. <https://doi.org/10.1029/eo066i037p00643>.
- [2] S. Pirani, Burning up: A global history of fossil fuel consumption, Pluto Press, London, 2018.
- [3] N. Abas, A. Kalair, N. Khan, Review of fossil fuels and future energy technologies, *Futures*. 69 (2015) 31–49. <https://doi.org/10.1016/j.futures.2015.03.003>.
- [4] IEA, World Energy Balances: Overview, Paris, 2021. <https://www.iea.org/reports/world-energy-balances-overview>.
- [5] IEA, World Energy Outlook 2021, Paris <https://www.iea.org/reports/world-energy-outlook-2021>, 2021. [www.iea.org/weo](http://www.iea.org/weo).
- [6] IEA, Global Energy Review 2021, Paris, 2021. <https://doi.org/10.1787/90c8c125-en>.
- [7] IEA, Resources to Reserves 2013: Oil, Gas and Coal Technologies for the Energy Markets of the Future, Paris, 2013. <https://doi.org/10.1787/9789264090705-en>.
- [8] G. Maggio, G. Cacciola, When will oil, natural gas, and coal peak?, *Fuel*. 98 (2012) 111–123. <https://doi.org/10.1016/j.fuel.2012.03.021>.
- [9] I. Chapman, The end of Peak Oil? Why this topic is still relevant despite recent denials, *Energy Policy*. 64 (2014) 93–101. <https://doi.org/10.1016/j.enpol.2013.05.010>.
- [10] P. Druetta, P. Raffa, F. Picchioni, Chemical enhanced oil recovery and the role of chemical product design, *Appl. Energy*. 252 (2019). <https://doi.org/10.1016/j.apenergy.2019.113480>.
- [11] D.J. Soeder, S.J. Borglum, The fossil fuel revolution: Shale gas and tight oil, 2019. <https://doi.org/10.1016/C2017-0-03254-8>.
- [12] IEA, The Oil and Gas Industry in Energy Transitions, Paris <https://www.iea.org/reports/the-oil-and-gas-industry-in-energy-transitions>, 2020.
- [13] T. Ahmed, Reservoir engineering handbook, Gulf professional publishing, 2018.
- [14] J.J. Sheng, Modern chemical enhanced oil recovery: theory and practice, Gulf Professional Publishing, 2010.
- [15] L.W. Lake, Enhanced oil recovery, Prentice-Hall, Englewood Cliffs, New Jersey, 1989.
- [16] T. Babadagli, Development of mature oil fields - A review, *J. Pet. Sci. Eng.* 57 (2007) 221–246. <https://doi.org/10.1016/j.petrol.2006.10.006>.

- [17] S. Thomas, Enhanced oil recovery-an overview, *Oil Gas Sci. Technol.* 63 (2008) 9–19. <https://doi.org/10.2516/ogst>.
- [18] Y. She, C. Zhang, M.A. Mahardika, A. Patmonoaji, Y. Hu, S. Matsushita, T. Suekane, Pore-scale study of in-situ surfactant flooding with strong oil emulsification in sandstone based on X-ray microtomography, *J. Ind. Eng. Chem.* 98 (2021) 247–261. <https://doi.org/10.1016/j.jiec.2021.03.046>.
- [19] K.S. Sorbie, D. Phil, *Polymer-Improved Oil Recovery*, Springer Science & Business Media, 2013.
- [20] Y. Hu, A. Patmonoaji, C. Zhang, T. Suekane, Experimental study on the displacement patterns and the phase diagram of immiscible fluid displacement in three-dimensional porous media, *Adv. Water Resour.* 140 (2020) 103584. <https://doi.org/10.1016/j.advwatres.2020.103584>.
- [21] S.A. Farzaneh, M.H. Ghazanfari, R. Kharrat, S. Vossoughi, An experimental and numerical investigation of solvent injection to heavy oil in fractured five-spot micromodels, *Pet. Sci. Technol.* 28 (2010) 1567–1585. <https://doi.org/10.1080/10916460903160784>.
- [22] T. Suekane, J. Ono, A. Hyodo, Y. Nagatsu, Three-dimensional viscous fingering of miscible fluids in porous media, *Phys. Rev. Fluids.* 2 (2017). <https://doi.org/10.1103/PhysRevFluids.2.103902>.
- [23] R. Tsuzuki, T. Ban, M. Fujimura, Y. Nagatsu, Dual role of surfactant-producing reaction in immiscible viscous fingering evolution, *Phys. Fluids.* 31 (2019). <https://doi.org/10.1063/1.5066581>.
- [24] A.M. Alhammadi, Y. Gao, T. Akai, M.J. Blunt, B. Bijeljic, Pore-scale X-ray imaging with measurement of relative permeability, capillary pressure and oil recovery in a mixed-wet micro-porous carbonate reservoir rock, *Fuel.* 268 (2020) 117018. <https://doi.org/10.1016/j.fuel.2020.117018>.
- [25] R.E. Terry, Enhanced oil recovery., *Encycl. Of Physical Sci. Technol.* 18 (2001) 503–518. <https://doi.org/https://doi.org/10.1016/B0-12-227410-5/00868-1>.
- [26] G.M. Homsy, Viscous Fingering in Porous Media, *Annu. Rev. Fluid Mech.* 19 (1987) 271–311.
- [27] J.R. Fanchi, *Principles of Applied Reservoir Simulation*, Gulf Professional Publishing, Texas, USA, 2018. <https://doi.org/10.1016/b978-0-12-815563-9.00009-4>.
- [28] R. Lenormand, E. Touboul, C. Zarcone, Numerical models and experiments on immiscible displacements in porous media, *J. Fluid Mech.* 189 (1988) 165–187. <https://doi.org/10.1017/S0022112088000953>.
- [29] Y. Hu, A. Patmonoaji, C. Zhang, T. Suekane, Experimental study on the displacement patterns and the phase diagram of immiscible fluid displacement in three-dimensional porous media, *Adv. Water Resour.* 140 (2020) 103584. <https://doi.org/10.1016/j.advwatres.2020.103584>.
- [30] C. Zhang, M. Oostrom, T.W. Wietsma, J.W. Grate, M.G. Warner, Influence of viscous and capillary forces on immiscible fluid displacement: Pore-scale

experimental study in a water-wet micromodel demonstrating viscous and capillary fingering, *Energy and Fuels*. 25 (2011) 3493–3505. <https://doi.org/10.1021/ef101732k>.

[31] S. An, H. Erfani, O.E. Godínez-Brizuela, V. Niasar, Transition From Viscous Fingering to Capillary Fingering: Application of GPU-Based Fully Implicit Dynamic Pore Network Modeling, *Water Resour. Res.* 56 (2020) 1–18. <https://doi.org/10.1029/2020WR028149>.

[32] H. Liu, Y. Zhang, A.J. Valocchi, Lattice boltzmann simulation of immiscible fluid displacement in porous media: Homogeneous versus heterogeneous pore network, *Phys. Fluids*. 27 (2015). <https://doi.org/10.1063/1.4921611>.

[33] Y.F. Chen, S. Fang, D.S. Wu, R. Hu, Visualizing and quantifying the crossover from capillary fingering to viscous fingering in a rough fracture, *Water Resour. Res.* 53 (2017) 7756–7772. <https://doi.org/10.1002/2017WR021051>.

[34] T. Tsuji, F. Jiang, K.T. Christensen, Characterization of immiscible fluid displacement processes with various capillary numbers and viscosity ratios in 3D natural sandstone, *Adv. Water Resour.* 95 (2016) 3–15. <https://doi.org/10.1016/j.advwatres.2016.03.005>.

[35] H.S. Rabbani, D. Or, Y. Liu, C.Y. Lai, N.B. Lu, S.S. Datta, H.A. Stone, N. Shokri, Suppressing viscous fingering in structured porous media, *Proc. Natl. Acad. Sci. U. S. A.* 115 (2018) 4833–4838. <https://doi.org/10.1073/pnas.1800729115>.

[36] M.J. Blunt, *Multiphase Flow in Permeable Media*, *Multiph. Flow Permeable Media*. (2017). <https://doi.org/10.1017/9781316145098>.

[37] J.D. Berry, M.J. Neeson, R.R. Dagastine, D.Y.C. Chan, R.F. Tabor, Measurement of surface and interfacial tension using pendant drop tensiometry, *J. Colloid Interface Sci.* 454 (2015) 226–237. <https://doi.org/10.1016/j.jcis.2015.05.012>.

[38] S. Zeppieri, J. Rodríguez, A.L. López De Ramos, Interfacial tension of alkane + water systems, *J. Chem. Eng. Data*. 46 (2001) 1086–1088. <https://doi.org/10.1021/je000245r>.

[39] A. Kumar, M.R. Gunjan, K. Jakhar, A. Thakur, R. Raj, Unified framework for mapping shape and stability of pendant drops including the effect of contact angle hysteresis, *Colloids Surfaces A Physicochem. Eng. Asp.* 597 (2020) 124619. <https://doi.org/10.1016/j.colsurfa.2020.124619>.

[40] R. Tadmor, P.S. Yadav, As-placed contact angles for sessile drops, *J. Colloid Interface Sci.* 317 (2008) 241–246. <https://doi.org/10.1016/j.jcis.2007.09.029>.

[41] A. Alhosani, B. Bijeljic, M.J. Blunt, Pore-Scale Imaging and Analysis of Wettability Order, Trapping and Displacement in Three-Phase Flow in Porous Media with Various Wettabilities, *Transp. Porous Media*. 140 (2021) 59–84. <https://doi.org/10.1007/s11242-021-01595-1>.

[42] G. Boccardo, T. Tosco, A. Fujisaki, F. Messina, A. Raoof, D.R. Aguilera, E. Crevacore, D.L. Marchisio, R. Sethi, A review of transport of nanoparticles in porous media: From pore- to macroscale using computational methods, Elsevier Inc., 2020. <https://doi.org/10.1016/B978-0-12-818489-9.00013-X>.



- [43] R. Oughanem, S. Youssef, D. Bauer, Y. Peysson, E. Maire, O. Vizika, A Multi-Scale Investigation of Pore Structure Impact on the Mobilization of Trapped Oil by Surfactant Injection, *Transp. Porous Media.* 109 (2015) 673–692. <https://doi.org/10.1007/s11242-015-0542-5>.
- [44] H. Liu, C. Ma, C. Zhu, X-ray Micro CT Based Characterization of Pore-Throat Network for Marine Carbonates from South China Sea, *Appl. Sci.* 12 (2022). <https://doi.org/10.3390/app12052611>.
- [45] J.J. Sheng, *Modern chemical enhanced oil recovery: theory and practice*, Elsevier Inc., Burlington, MA 01803, USA, 2011. <https://doi.org/10.1016/B978-1-85617-745-0.00004-8>.
- [46] P.D.I. Fletcher, L.D. Savory, F. Woods, A. Clarke, A.M. Howe, Model Study of Enhanced Oil Recovery by Flooding with Aqueous Surfactant Solution and Comparison with Theory, *Langmuir.* 31 (2015) 3076–3085. <https://doi.org/10.1021/la5049612>.
- [47] M.S. Kamal, I.A. Hussein, A.S. Sultan, Review on Surfactant Flooding: Phase Behavior, Retention, IFT, and Field Applications, *Energy and Fuels.* 31 (2017) 7701–7720. <https://doi.org/10.1021/acs.energyfuels.7b00353>.
- [48] M.M. Ramirez-Corredores, *The science and technology of unconventional oils: Finding refining opportunities*, 2017.
- [49] D. Lirong, C. Dingsheng, L. Zhi, Z. Zhiwei, W. Jingchun, Petroleum geology of the fula sub-basin, Muglad basin, Sudan, *J. Pet. Geol.* 36 (2013) 43–59. <https://doi.org/10.1111/jpg.12541>.
- [50] C. Negin, S. Ali, Q. Xie, Most common surfactants employed in chemical enhanced oil recovery, *Petroleum.* 3 (2017) 197–211. <https://doi.org/10.1016/j.petlm.2016.11.007>.
- [51] W. Chen, D.S. Schechter, Surfactant selection for enhanced oil recovery based on surfactant molecular structure in unconventional liquid reservoirs, *J. Pet. Sci. Eng.* 196 (2021) 107702. <https://doi.org/10.1016/j.petrol.2020.107702>.
- [52] Y. Yao, M. Wei, W. Kang, A review of wettability alteration using surfactants in carbonate reservoirs, *Adv. Colloid Interface Sci.* 294 (2021) 102477. <https://doi.org/10.1016/j.cis.2021.102477>.
- [53] A. Kumar, A. Mandal, Critical investigation of zwitterionic surfactant for enhanced oil recovery from both sandstone and carbonate reservoirs: Adsorption, wettability alteration and imbibition studies, *Chem. Eng. Sci.* 209 (2019) 115222. <https://doi.org/10.1016/j.ces.2019.115222>.
- [54] X. Zhao, Y. Feng, G. Liao, W. Liu, Visualizing in-situ emulsification in porous media during surfactant flooding: A microfluidic study, *J. Colloid Interface Sci.* 578 (2020) 629–640. <https://doi.org/10.1016/j.jcis.2020.06.019>.
- [55] E. Unsal, M. Rücker, S. Berg, W.B. Bartels, A. Bonnin, Imaging of compositional gradients during in situ emulsification using X-ray micro-tomography, *J. Colloid Interface Sci.* 550 (2019) 159–169. <https://doi.org/10.1016/j.jcis.2019.04.068>.

- [56] H. Wang, B. Wei, Z. Sun, Q. Du, J. Hou, Microfluidic study of heavy oil emulsification on solid surface, *Chem. Eng. Sci.* 246 (2021) 117009. <https://doi.org/10.1016/j.ces.2021.117009>.
- [57] J.R. Barnes, J.P. Smit, J.R. Smit, P.G. Shpakoff, K.H. Raney, M.C. Puerto, Development of Surfactants for Chemical Flooding at Difficult Reservoir Conditions, in: *SPE Symp. Improv. Oil Recover.*, Society of Petroleum Engineers: Richardson, TX, USA, 2008. <https://doi.org/10.2118/113313-MS>.
- [58] K. Ma, L. Cui, Y. Dong, T. Wang, C. Da, G.J. Hirasaki, S.L. Biswal, Adsorption of cationic and anionic surfactants on natural and synthetic carbonate materials, *J. Colloid Interface Sci.* 408 (2013) 164–172. <https://doi.org/10.1016/j.jcis.2013.07.006>.
- [59] V. Mirchi, M.J. Sabti, M. Piri, L. Goual, Microscale Investigation of the Impact of Surfactant Structure on the Residual Trapping in Natural Porous Media, *Ind. Eng. Chem. Res.* 58 (2019) 9397–9411. <https://doi.org/10.1021/acs.iecr.9b00748>.
- [60] G. Sharma, K.K. Mohanty, Wettability alteration in high-temperature and high-salinity carbonate reservoirs, *SPE J.* 18 (2013) 646–655. <https://doi.org/10.2118/147306-PA>.
- [61] Y. Nan, W. Li, Z. Jin, Role of Alcohol as a Cosurfactant at the Brine-Oil Interface under a Typical Reservoir Condition, *Langmuir.* 36 (2020) 5198–5207. <https://doi.org/10.1021/acs.langmuir.0c00494>.
- [62] V. Hornof, G.H. Neale, A. Yu, Effect of flooding sequence on the displacement of acidic oil by alkaline solutions, *J. Pet. Sci. Eng.* 10 (1994) 291–297. [https://doi.org/10.1016/0920-4105\(94\)90020-5](https://doi.org/10.1016/0920-4105(94)90020-5).
- [63] Y. Sumino, N.L. Yamada, M. Nagao, T. Honda, H. Kitahata, Y.B. Melnichenko, H. Seto, Mechanism of Spontaneous Blebbing Motion of an Oil-Water Interface: Elastic Stress Generated by a Lamellar-Lamellar Transition, *Langmuir.* 32 (2016) 2891–2899. <https://doi.org/10.1021/acs.langmuir.6b00107>.
- [64] Y. Sumino, H. Kitahata, H. Seto, S. Nakata, K. Yoshikawa, Spontaneous deformation of an oil droplet induced by the cooperative transport of cationic and anionic surfactants through the interface, *J. Phys. Chem. B.* 113 (2009) 15709–15714. <https://doi.org/10.1021/jp9037733>.
- [65] Y. Sumino, H. Kitahata, Y. Shinohara, N.L. Yamada, H. Seto, Formation of a multiscale aggregate structure through spontaneous blebbing of an interface, *Langmuir.* 28 (2012) 3378–3384. <https://doi.org/10.1021/la204323t>.
- [66] S. Zhang, J. Yan, H. Qi, J. Luan, W. Qiao, Z. Li, Interfacial tensions of phenyltetradecane sulfonates for enhanced oil recovery upon the addition of fatty acids, *J. Pet. Sci. Eng.* 47 (2005) 117–122. <https://doi.org/10.1016/j.petrol.2005.03.004>.
- [67] Y. She, M.A. Mahardika, Y. Hu, A. Patmonoaji, S. Matsushita, T. Suekane, Y. Nagatsu, Three-dimensional visualization of the alkaline flooding process with in-situ emulsification for oil recovery in porous media, *J. Pet. Sci. Eng.* 202 (2021) 108519. <https://doi.org/10.1016/j.petrol.2021.108519>.

- [68] H. Pei, G. Zhang, J. Ge, M. Tang, Y. Zheng, Comparative effectiveness of alkaline flooding and alkaline-surfactant flooding for improved heavy-oil recovery, *Energy and Fuels*. 26 (2012) 2911–2919. <https://doi.org/10.1021/ef300206u>.
- [69] H. Pei, G. Zhang, J. Ge, L. Jin, X. Liu, Analysis of microscopic displacement mechanisms of alkaline flooding for enhanced heavy-oil recovery, *Energy and Fuels*. 25 (2011) 4423–4429. <https://doi.org/10.1021/ef200605a>.
- [70] H. Gong, Y. Li, M. Dong, S. Ma, W. Liu, Effect of wettability alteration on enhanced heavy oil recovery by alkaline flooding, *Colloids Surfaces A Physicochem. Eng. Asp.* 488 (2016) 28–35. <https://doi.org/10.1016/j.colsurfa.2015.09.042>.
- [71] X. Shang, Y. Bai, J. Sun, C. Dong, Performance and displacement mechanism of a surfactant/compound alkaline flooding system for enhanced oil recovery, *Colloids Surfaces A Physicochem. Eng. Asp.* 580 (2019) 123679. <https://doi.org/10.1016/j.colsurfa.2019.123679>.
- [72] M. Dong, Q. Liu, A. Li, Displacement mechanisms of enhanced heavy oil recovery by alkaline flooding in a micromodel, *Particuology*. 10 (2012) 298–305. <https://doi.org/10.1016/j.partic.2011.09.008>.
- [73] M.A. Mahardika, Y. She, F. Shori, A. Patmonoaji, S. Matsushita, T. Suekane, Y. Nagatsu, Enhanced Heavy Oil Recovery by Calcium Hydroxide Flooding with the Production of Viscoelastic Materials: Study with 3-D X-Ray Tomography and 2-D Glass Micromodels, *Energy and Fuels*. 35 (2021) 11210–11222. <https://doi.org/10.1021/acs.energyfuels.1c00963>.
- [74] Y. Nagatsu, K. Abe, K. Konmoto, K. Omori, Chemical Flooding for Enhanced Heavy Oil Recovery via Chemical-Reaction-Producing Viscoelastic Material, *Energy and Fuels*. 34 (2020) 10655–10665. <https://doi.org/10.1021/acs.energyfuels.0c01298>.
- [75] Y. Zhou, D. Yin, W. Chen, B. Liu, X. Zhang, A comprehensive review of emulsion and its field application for enhanced oil recovery, *Energy Sci. Eng.* 7 (2019) 1046–1058. <https://doi.org/10.1002/ese3.354>.
- [76] S.F. Wong, J.S. Lim, S.S. Dol, Crude oil emulsion: A review on formation, classification and stability of water-in-oil emulsions, *J. Pet. Sci. Eng.* 135 (2015) 498–504. <https://doi.org/10.1016/j.petrol.2015.10.006>.
- [77] M. Arhuoma, M. Dong, D. Yang, R. Idem, Determination of water-in-oil emulsion viscosity in porous media, *Ind. Eng. Chem. Res.* 48 (2009) 7092–7102. <https://doi.org/10.1021/ie801818n>.
- [78] Z. Liu, Y. Li, H. Luan, W. Gao, Y. Guo, Y. Chen, Pore scale and macroscopic visual displacement of oil-in-water emulsions for enhanced oil recovery, *Chem. Eng. Sci.* 197 (2019) 404–414. <https://doi.org/10.1016/j.ces.2019.01.001>.
- [79] C.E. Johnson, Status of Caustic and Emulsion Methods., *JPT, J. Pet. Technol.* 28 (1976) 85–92. <https://doi.org/10.2118/5561-PA>.
- [80] B. Ding, M. Dong, L. Yu, A model of emulsion plugging ability in sandpacks: Yield pressure drop and consistency parameter, *Chem. Eng. Sci.* 211 (2020)

115248. <https://doi.org/10.1016/j.ces.2019.115248>.

[81] M.I. Romero, M.S. Carvalho, V. Alvarado, Experiments and network model of flow of oil-water emulsion in porous media, *Phys. Rev. E - Stat. Nonlinear, Soft Matter Phys.* 84 (2011) 1–7. <https://doi.org/10.1103/PhysRevE.84.046305>.

[82] L. Zhang, L. Luo, S. Zhao, Z. cheng Xu, J. yi An, J. yong Yu, Effect of different acidic fractions in crude oil on dynamic interfacial tensions in surfactant/alkali/model oil systems, *J. Pet. Sci. Eng.* 41 (2004) 189–198. [https://doi.org/10.1016/S0920-4105\(03\)00153-0](https://doi.org/10.1016/S0920-4105(03)00153-0).

[83] A.M. Al-Bahlani, T. Babadagli, Visual analysis of diffusion process during oil recovery using a Hele-Shaw model with hydrocarbon solvents and thermal methods, *Chem. Eng. J.* 181–182 (2012) 557–569. <https://doi.org/10.1016/j.ces.2011.11.087>.

[84] S. Maaref, A. Kantzas, S.L. Bryant, The effect of water alternating solvent based nanofluid flooding on heavy oil recovery in oil-wet porous media, *Fuel* 282 (2020). <https://doi.org/10.1016/j.fuel.2020.118808>.

[85] E.W. Al Shalabi, K. Sepehrnoori, *Low Salinity and Engineered Water Injection for Sandstone and Carbonate Reservoirs*, 2017.

[86] M.G. Rezk, J. Foroozesh, Determination of mass transfer parameters and swelling factor of CO<sub>2</sub>-oil systems at high pressures, *Int. J. Heat Mass Transf.* 126 (2018) 380–390. <https://doi.org/10.1016/j.ijheatmasstransfer.2018.05.043>.

[87] D. Du, L. Zheng, K. Ma, F. Wang, Z. Sun, Y. Li, Determination of diffusion coefficient of a miscible CO<sub>2</sub>/n-hexadecane system with Dynamic Pendant Drop Volume Analysis (DPDVA) technique, *Int. J. Heat Mass Transf.* 139 (2019) 982–989. <https://doi.org/10.1016/j.ijheatmasstransfer.2019.05.083>.

[88] Y. Hu, C. Zhang, A. Patmonoaji, Y. She, S. Matsushita, T. Suekane, Pore-scale investigation of wettability impact on residual nonaqueous phase liquid dissolution in natural porous media, *Sci. Total Environ.* 787 (2021) 147406. <https://doi.org/10.1016/j.scitotenv.2021.147406>.

[89] Y. Teng, P. Wang, L. Jiang, Y. Liu, Y. Song, Y. Wei, An experimental study of density-driven convection of fluid pairs with viscosity contrast in porous media, *Int. J. Heat Mass Transf.* 152 (2020) 119514. <https://doi.org/10.1016/j.ijheatmasstransfer.2020.119514>.

[90] V. Cnudde, M.N. Boone, High-resolution X-ray computed tomography in geosciences: A review of the current technology and applications, *Earth-Science Rev.* 123 (2013) 1–17. <https://doi.org/10.1016/j.earscirev.2013.04.003>.

[91] S. Youssef, E. Rosenberg, H. Deschamps, R. Oughanem, E. Maire, R. Mokso, Oil ganglia dynamics in natural porous media during surfactant flooding captured by ultra-fast x-ray microtomography, *Int. Symp. Soc. Core Anal.* (2014) 1–12.

[92] G. Javanbakht, M. Arshadi, T. Qin, L. Goual, Micro-scale displacement of NAPL by surfactant and microemulsion in heterogeneous porous media, *Adv. Water Resour.* 105 (2017) 173–187. <https://doi.org/10.1016/j.advwatres.2017.05.006>.

- [93] A. Setiawan, T. Suekane, Y. Deguchi, K. Kusano, Three-Dimensional Imaging of Pore-Scale Water Flooding Phenomena in Water-Wet and Oil-Wet Porous Media, *J. Flow Control. Meas. & Vis.* 02 (2014) 25–31. <https://doi.org/10.4236/jfcmv.2014.22005>.
- [94] A.I.A. Mohamed, M. Khishvand, M. Piri, A pore-scale experimental investigation of process-dependent capillary desaturation, *Adv. Water Resour.* 144 (2020) 103702. <https://doi.org/10.1016/j.advwatres.2020.103702>.
- [95] Y.A. Alzahid, H. Aborshaid, M. Asali, J. McClure, C. Chen, P. Mostaghimi, Y. Da Wang, C. Sun, R.T. Armstrong, Real-time synchrotron-based X-ray computed microtomography during in situ emulsification, *J. Pet. Sci. Eng.* 195 (2020) 107885. <https://doi.org/10.1016/j.petrol.2020.107885>.
- [96] T. Qin, L. Goual, M. Piri, Z. Hu, D. Wen, Pore-scale dynamics of nanofluid-enhanced NAPL displacement in carbonate rock, *J. Contam. Hydrol.* 230 (2020) 103598. <https://doi.org/10.1016/j.jconhyd.2019.103598>.
- [97] H. Long, R. Swennen, A. Foubert, M. Dierick, P. Jacobs, 3D quantification of mineral components and porosity distribution in Westphalian C sandstone by microfocus X-ray computed tomography, *Sediment. Geol.* 220 (2009) 116–125. <https://doi.org/10.1016/j.sedgeo.2009.07.003>.
- [98] Y. Chen, N.K. Jha, D. Al-Bayati, M. Lebedev, M. Sarmadivaleh, S. Iglauer, A. Saedi, Q. Xie, Geochemical controls on wettability alteration at pore-scale during low salinity water flooding in sandstone using X-ray micro computed tomography, *Fuel.* 271 (2020) 117675. <https://doi.org/10.1016/j.fuel.2020.117675>.
- [99] A. Patmonoaji, M. Muharrir, Y. Hu, C. Zhang, T. Suekane, Three-dimensional fingering structures in immiscible flow at the crossover from viscous to capillary fingering, *Int. J. Multiph. Flow.* 122 (2020). <https://doi.org/10.1016/j.ijmultiphaseflow.2019.103147>.
- [100] A. Patmonoaji, K. Tsuji, T. Suekane, Pore-throat characterization of unconsolidated porous media using watershed-segmentation algorithm, *Powder Technol.* 362 (2020) 635–644. <https://doi.org/10.1016/j.powtec.2019.12.026>.
- [101] W. Kuang, S. Saraji, M. Piri, Nanofluid-Induced Wettability Gradient and Imbibition Enhancement in Natural Porous Media: A Pore-scale Experimental Investigation, *Transp. Porous Media.* 134 (2020) 593–619. <https://doi.org/10.1007/s11242-020-01459-0>.
- [102] W. Kuang, S. Saraji, M. Piri, Pore-Scale Sweep Efficiency Enhancement by Silica-Based Nanofluids in Oil-Wet Sandstone, *Energy and Fuels.* 34 (2020) 1297–1308. <https://doi.org/10.1021/acs.energyfuels.9b03081>.
- [103] J.T. Davies, Reprinted from: Gas/Liquid and Liquid/Liquid Interfaces. Proceedings of 2nd International Congress Surface Activity, A quantitative Kinet. Theory Emuls. Type. I Phys. Chem. Emuls. Agent. (1957) 426–438. [http://www.firp.ula.ve/archivos/historicos/57\\_Chap\\_Davies.pdf](http://www.firp.ula.ve/archivos/historicos/57_Chap_Davies.pdf).
- [104] R. Tsuzuki, R. Tanaka, T. Ban, Y. Nagatsu, Deviation from capillary number scaling of nonlinear viscous fingering formed by the injection of Newtonian

surfactant solution, *Phys. Fluids*. 31 (2019). <https://doi.org/10.1063/1.5090827>.

[105] Y. Hong, W. Xu, Y. Hu, G. Li, M. Chen, J. Hao, S. Dong, Multi-responsive emulsion of stearic acid soap aqueous solution, *Colloids Surfaces A Physicochem. Eng. Asp.* 522 (2017) 652–657. <https://doi.org/10.1016/j.colsurfa.2017.03.053>.

[106] X. Guan, Z. Huang, P. Fang, H. Lu, D. Sun, CO<sub>2</sub> responsive emulsions stabilized with fatty acid soaps in NaCl brine, *Colloids Surfaces A Physicochem. Eng. Asp.* 571 (2019) 134–141. <https://doi.org/10.1016/j.colsurfa.2019.03.082>.

[107] N.K. Jha, M. Lebedev, S. Iglauer, M. Ali, H. Roshan, A. Barifcani, J.S. Sangwai, M. Sarmadivaleh, Pore scale investigation of low salinity surfactant nanofluid injection into oil saturated sandstone via X-ray micro-tomography, *J. Colloid Interface Sci.* 562 (2020) 370–380. <https://doi.org/10.1016/j.jcis.2019.12.043>.

[108] R. Saha, R.V.S. Uppaluri, P. Tiwari, Influence of emulsification, interfacial tension, wettability alteration and saponification on residual oil recovery by alkali flooding, *J. Ind. Eng. Chem.* 59 (2018) 286–296. <https://doi.org/10.1016/j.jiec.2017.10.034>.

[109] A. Georgiadis, S. Berg, A. Makurat, G. Maitland, H. Ott, Pore-scale micro-computed-tomography imaging: Nonwetting-phase cluster-size distribution during drainage and imbibition, *Phys. Rev. E - Stat. Nonlinear, Soft Matter Phys.* 88 (2013) 1–9. <https://doi.org/10.1103/PhysRevE.88.033002>.

[110] Buades, Antoni, B. Coll, J.M. Morel, A non-local algorithm for image denoising, *IEEE Comput. Soc. Conf. Comput. Vis. Pattern Recognit.* 2 (2005) 60–65. <https://doi.org/10.1109/ICIP.2006.312698>.

[111] A. Buades, B. Coll, J.M. Morel, Nonlocal image and movie denoising, *Int. J. Comput. Vis.* 76 (2008) 123–139. <https://doi.org/10.1007/s11263-007-0052-1>.

[112] M. Andrew, B. Bijeljic, M.J. Blunt, Pore-scale contact angle measurements at reservoir conditions using X-ray microtomography, *Adv. Water Resour.* 68 (2014) 24–31. <https://doi.org/10.1016/j.advwatres.2014.02.014>.

[113] Y. Hu, Y. She, A. Patmonoaji, C. Zhang, T. Suekane, Effect of capillary number on morphological characterizations of trapped gas bubbles: Study by using micro-tomography, *Int. J. Heat Mass Transf.* 163 (2020) 120508. <https://doi.org/10.1016/j.ijheatmasstransfer.2020.120508>.

[114] H. Zhang, C.A. Miller, P.R. Garrett, K.H. Raney, Mechanism for defoaming by oils and calcium soap in aqueous systems, *J. Colloid Interface Sci.* 263 (2003) 633–644. [https://doi.org/10.1016/S0021-9797\(03\)00367-9](https://doi.org/10.1016/S0021-9797(03)00367-9).

[115] H. Pei, G. Zhang, J. Ge, L. Jin, L. Ding, Study on the variation of dynamic interfacial tension in the process of alkaline flooding for heavy oil, *Fuel*. 104 (2013) 372–378. <https://doi.org/10.1016/j.fuel.2012.10.022>.

[116] A. Samanta, K. Ojha, A. Mandal, Interactions between acidic crude oil and alkali and their effects on enhanced oil recovery, *Energy and Fuels*. 25 (2011) 1642–1649. <https://doi.org/10.1021/ef101729f>.

[117] C. Zhang, T. Suekane, K. Minokawa, Y. Hu, A. Patmonoaji, Solute

transport in porous media studied by lattice Boltzmann simulations at pore scale and x-ray tomography experiments, *Phys. Rev. E.* 100 (2019) 63110. <https://doi.org/10.1103/PhysRevE.100.063110>.

[118] D.C. Standnes, T. Austad, Wettability alteration in chalk: 2. Mechanism for wettability alteration from oil-wet to water-wet using surfactants, *J. Pet. Sci. Eng.* 28 (2000) 123–143. [https://doi.org/10.1016/s0920-4105\(00\)00084-x](https://doi.org/10.1016/s0920-4105(00)00084-x).

[119] Y. Zhou, D. Yin, D. Wang, X. Gao, Emulsion particle size in porous media and its effect on the displacement efficiency, *J. Dispers. Sci. Technol.* 39 (2018) 1532–1536. <https://doi.org/10.1080/01932691.2017.1421082>.

[120] X. Chen, Y. Li, W. Gao, C. Chen, Experimental investigation on transport property and emulsification mechanism of polymeric surfactants in porous media, *J. Pet. Sci. Eng.* 186 (2020) 106687. <https://doi.org/10.1016/j.petrol.2019.106687>.

[121] T. Kawanishi, Y. Hayashi, P. V. Roberts, M.J. Blunt, Fluid-fluid interfacial area during two and three phase fluid displacement in porous media: A network model study, in: *Int. Conf. Spec. Semin. Groundw. Qual. Remediat. Prot.*, Tubingen, Germany, 1998: pp. 89–96.

[122] L.C. Ruspini, R. Farokhpoor, P.E. Øren, Pore-scale modeling of capillary trapping in water-wet porous media: A new cooperative pore-body filling model, *Adv. Water Resour.* 108 (2017) 1–14. <https://doi.org/10.1016/j.advwatres.2017.07.008>.

[123] A.L. Herring, E.J. Harper, L. Andersson, A. Sheppard, B.K. Bay, D. Wildenschild, Effect of fluid topology on residual nonwetting phase trapping: Implications for geologic CO<sub>2</sub> sequestration, *Adv. Water Resour.* 62 (2013) 47–58. <https://doi.org/10.1016/j.advwatres.2013.09.015>.

[124] R.T. Armstrong, J.E. McClure, V. Robins, Z. Liu, C.H. Arns, S. Schlüter, S. Berg, Porous Media Characterization Using Minkowski Functionals: Theories, Applications and Future Directions, *Transp. Porous Media.* 130 (2019) 305–335. <https://doi.org/10.1007/s11242-018-1201-4>.

[125] Y. Sumino, H. Kitahata, H. Seto, K. Yoshikawa, Blebbing dynamics in an oil-water-surfactant system through the generation and destruction of a gel-like structure, *Phys. Rev. E.* 76 (2007) 1–4. <https://doi.org/10.1103/PhysRevE.76.055202>.

[126] M. Sahimi, Flow phenomena in rocks: From continuum models to fractals, percolation, cellular automata, and simulated annealing, *Rev. Mod. Phys.* 65 (1993) 1393–1534. <https://doi.org/10.1103/RevModPhys.65.1393>.

[127] P.S. Hammond, E. Unsal, A Dynamic Pore Network Model for Oil Displacement by Wettability-Altering Surfactant Solution, *Transp. Porous Media.* 92 (2012) 789–817. <https://doi.org/10.1007/s11242-011-9933-4>.

[128] A. Patmonoaji, M.A. Mahardika, M. Nasir, Y. She, W. Wang, M.A. Muflikhun, T. Suekane, Stereolithography 3D Printer for Micromodel Fabrications with Comprehensive Accuracy Evaluation by Using Microtomography, *Geosciences.* 12 (2022) 183. <https://doi.org/https://doi.org/10.3390/geosciences12050183>.

[129] S. Uemoto, T. Toyota, L. Chiari, T. Nomoto, M. Fujinami, Assemblies of

molecular aggregates in the blebbing motion of an oil droplet on an aqueous solution containing surfactant, *Colloids Surfaces A Physicochem. Eng. Asp.* 529 (2017) 373–379. <https://doi.org/10.1016/j.colsurfa.2017.06.016>.

[130] A. Patmonoaji, T. Suekane, Investigation of CO<sub>2</sub> dissolution via mass transfer inside a porous medium, *Adv. Water Resour.* 110 (2017) 97–106. <https://doi.org/10.1016/j.advwatres.2017.10.008>.

[131] L. Wang, S. Cai, T. Suekane, Gravitational Fingering Due to Density Increase by Mixing at a Vertical Displacing Front in Porous Media, *Energy and Fuels.* 32 (2018) 658–669. <https://doi.org/10.1021/acs.energyfuels.7b02819>.

[132] L. Thibodeau, M. Sakanoko, G.H. Neale, Alkaline flooding processes in porous media in the presence of connate water, *Powder Technol.* 132 (2003) 101–111. [https://doi.org/10.1016/S0032-5910\(03\)00055-X](https://doi.org/10.1016/S0032-5910(03)00055-X).

[133] H. Guo, K. Song, R. Hilfer, A critical review of capillary number and its application in enhanced oil recovery, *Proc. - SPE Symp. Improv. Oil Recover.* 2020-Augus (2020). <https://doi.org/10.2118/200419-ms>.

[134] J.H. Abou-Kassem, S.M. Farouq Ali, Modelling of emulsion flow in porous media, *J. Can. Pet. Technol.* 34 (1995) 30–38. <https://doi.org/10.2118/95-06-02>.

[135] M. Broens, E. Unsal, Emulsification kinetics during quasi-miscible flow in dead-end pores, *Adv. Water Resour.* 113 (2018) 13–22. <https://doi.org/10.1016/j.advwatres.2018.01.001>.

[136] S. Roman, M.O. Abu-Al-Saud, T. Tokunaga, J. Wan, A.R. Kavscek, H.A. Tchelepi, Measurements and simulation of liquid films during drainage displacements and snap-off in constricted capillary tubes, *J. Colloid Interface Sci.* 507 (2017) 279–289. <https://doi.org/10.1016/j.jcis.2017.07.092>.

[137] M.M. Almajid, A.R. Kavscek, Pore Network Investigation of Trapped Gas and Foam Generation Mechanisms, *Transp. Porous Media.* 131 (2020) 289–313. <https://doi.org/10.1007/s11242-018-01224-4>.

[138] B. Wang, T. Wu, Y. Li, D. Sun, M. Yang, Y. Gao, F. Lu, X. Li, The effects of oil displacement agents on the stability of water produced from ASP (alkaline/surfactant/polymer) flooding, *Colloids Surfaces A Physicochem. Eng. Asp.* 379 (2011) 121–126. <https://doi.org/10.1016/j.colsurfa.2010.11.064>.

[139] Y. ZHOU, D. WANG, Z. WANG, R. CAO, The formation and viscoelasticity of pore-throat scale emulsion in porous media, *Pet. Explor. Dev.* 44 (2017) 111–118. [https://doi.org/10.1016/S1876-3804\(17\)30014-9](https://doi.org/10.1016/S1876-3804(17)30014-9).

[140] G. Catanoiu, E. Carey, S.R. Patil, S. Engelskirchen, C. Stubenrauch, Partition coefficients of nonionic surfactants in water/n-alkane systems, *J. Colloid Interface Sci.* 355 (2011) 150–156. <https://doi.org/10.1016/j.jcis.2010.12.002>.

[141] J.T. Gostick, Versatile and efficient pore network extraction method using marker-based watershed segmentation, *Phys. Rev. E.* 96 (2017) 1–15. <https://doi.org/10.1103/PhysRevE.96.023307>.

[142] J. Gostick, Z. Khan, T. Tranter, M. Kok, M. Agnaou, M. Sadeghi, R.



Jervis, PoreSpy: A Python Toolkit for Quantitative Analysis of Porous Media Images, *J. Open Source Softw.* 4 (2019) 1296. <https://doi.org/10.21105/joss.01296>.

[143] T.S. Yun, T.M. Evans, Three-dimensional random network model for thermal conductivity in particulate materials, *Comput. Geotech.* 37 (2010) 991–998. <https://doi.org/10.1016/j.compgeo.2010.08.007>.

[144] Y. Hu, Y. She, A. Patmonoaji, C. Zhang, T. Suekane, Effect of capillary number on morphological characterizations of trapped gas bubbles: Study by using micro-tomography, *Int. J. Heat Mass Transf.* 163 (2020). <https://doi.org/10.1016/j.ijheatmasstransfer.2020.120508>.

[145] A. Patmonoaji, K. Tsuji, M. Muharrik, T. Suekane, Micro-tomographic analyses of specific interfacial area inside unconsolidated porous media with differing particle characteristics from microscopic to macroscopic scale, *J. Colloid Interface Sci.* 532 (2018) 614–621. <https://doi.org/10.1016/j.jcis.2018.08.023>.

[146] D.B. Levitt, A.C. Jackson, C. Heinson, L.N. Britton, T. Malik, V. Dwarakanath, G.A. Pope, Identification and evaluation of high-performance EOR surfactants, *Proc. - SPE Symp. Improv. Oil Recover.* 2 (2006) 1154–1164. <https://doi.org/10.2118/100089-ms>.

[147] P. Zhao, A.C. Jackson, C. Britton, D.H. Kim, L.N. Britton, D.B. Levitt, G.A. Pope, Development of high-performance surfactants for difficult oils, *SPE - DOE Improv. Oil Recover. Symp. Proc.* 2 (2008) 828–838. <https://doi.org/10.2118/113432-ms>.

[148] D.B. Levitt, M. Chamerois, M. Bourrel, P. Gauer, D. Morel, The effect of a non-negative salinity gradient on ASP flood performance, *Soc. Pet. Eng. - SPE Enhanc. Oil Recover. Conf. 2011, EORC 2011.* 2 (2011) 1266–1278. <https://doi.org/10.2118/144938-ms>.

[149] E. Unsal, M. Broens, R.T. Armstrong, Pore Scale Dynamics of Microemulsion Formation, *Langmuir.* 32 (2016) 7096–7108. <https://doi.org/10.1021/acs.langmuir.6b00821>.

[150] E. Trine, P. Suniga, R. Fortenberry, Chemical EOR for offshore platforms using a novel chemical gradient design, *Proc. - SPE Annu. Tech. Conf. Exhib. 2015-Janua* (2015) 5969–5984. <https://doi.org/10.2118/175130-ms>.

[151] A. Alhosani, Q. Lin, A. Scanziani, E. Andrews, K. Zhang, B. Bijeljic, M.J. Blunt, Pore-scale characterization of carbon dioxide storage at immiscible and near-miscible conditions in altered-wettability reservoir rocks, *Int. J. Greenh. Gas Control.* 105 (2021) 103232. <https://doi.org/10.1016/j.ijggc.2020.103232>.

[152] B. Ding, L. Yu, M. Dong, I. Gates, Study of conformance control in oil sands by oil-in-water emulsion injection using heterogeneous parallel-sandpack models, *Fuel.* 244 (2019) 335–351. <https://doi.org/10.1016/j.fuel.2019.02.021>.

[153] K.A. Nadeeka Upamali, P. Jith Liyanage, S. Hyun Jang, E. Shook, U.P. Weerasooriya, G.A. Pope, New surfactants and cosolvents increase oil recovery and reduce cost, *SPE J.* 23 (2018) 2202–2217. <https://doi.org/10.2118/179702-PA>.

[154] P. Lele, A.H. Syed, J. Riordon, N. Mosavat, A. Guerrero, H. Fadaei, D.

Sinton, Deformation of microdroplets in crude oil for rapid screening of enhanced oil recovery additives, *J. Pet. Sci. Eng.* 165 (2018) 298–304. <https://doi.org/10.1016/j.petrol.2018.02.009>.

## Acknowledgements

As the time be fleeting, my three-year PhD career is now coming to an end. I can still remember the first day that I just reached Haneda airport in Japan. I was fulfilled with strong curiosity about the high-level Japanese education and famous anime culture. Throughout the whole experience of PhD in Japan, it is never forgettable since I have obtained valuable oversea research and living experiences. I am very proud that I could complete my doctoral degree in Tokyo Institute of Technology, one of the most prestigious universities in Japan.

First and foremost, I would like to express great gratitude to my supervisor, Professor Tetsuya SUEKANE. Without his guidance and help, I cannot obtain fruitful academical achievements and complete this work in time. Sensei is very kind-hearted and teach me step by step to guide me toward the correct direction. Thanks to his frequent and patient discussion, I am able to establish a strong foundation and understand my research topics deeper and deeper, including originalities, experimental design and analysis. Thanks to his encouragement, I can release my frustration and pressure and go bravely onward. I believe it is forever unforgettable experiences here and could accompany me for all my life. I hope I can deliver the knowledge and skills that I learned from Professor Suekane to the other students and contribute to the development of society.

I would like to acknowledge fundings Japan Society for the Promotion of Science (JSPS) and China Scholarship Council (CSC). All my research works were sponsored by the JSPS, including the fees of experiment materials and international conference. A special thanks to my country, I could have a chance to study oversea because of continuous living supporting. Without their funding, I cannot complete my doctoral research.

I would like to express sincere appreciation to my colleagues in my laboratory. Assistant Professor Shintaro Matsushita provided a good administration and help on my experiments. Dr. Anindityo Patmonoaji, Dr. Yingxue Hu and Dr. Chunwei Zhang provided a tremendous help and supporting for my research works. Thanks for their all-time discussions and suggestions. As my close classmate, I want to appreciate Dr. Mahardika Mohammad Azis for his help of doing my experiments when I am busy with my thesis writing. In the future, I wish I can travel to Indonesia and meet him there. A special thanks to Mr. Hirotaka Aoki, we always discussed about oil blebbing experiment and analyzed the results together. I published additional two papers because of his tremendous contribution. Thanks to Mr. Weicen Wang, Mr. Muhammad Nasir, Mr. Ryuhei Yamaguchi and Ms. Zijing Li and Mr. Kailin Wang for their patient discussions about my research works. All of my colleagues help me a lot and promote my research smoothly. Furthermore, I enjoyed talking with them about different cultures, travel and delicious food, which made my extracurricular life colorful.

Finally, I would like to thank my parents and younger sister for their understanding, encouragement and unwavering support. I can be light-hearted to focus on my research.

## Acknowledgements

---

Without their love and support, none of thing is possible.

## Academic achievements

### 1. Publication list

- [1] **Y. She**, C. Zhang, M. A. Mahardika, A. Patmonoaji, Y. Hu\*, S. Matsushita, T. Suekane. "Pore-scale study of in-situ surfactant flooding with strong oil emulsification in sandstone based on X-ray microtomography." *Journal of Industrial and Engineering Chemistry* 98(2021): 247-261. (SCI journal, IF=6.760, JCR Q1) (Fully included in Chapter 2) <https://doi.org/10.1016/j.jiec.2021.03.046>
- [2] **Y. She**, H. Aoki, W. Wang, Z. Li, M. Nashir, M. A. Mahardika\*, A. Patmonoaji, S. Matsushita, T. Suekane. "Spontaneous deformation of oil clusters induced by dual surfactants for oil recovery: Dynamic study from Hele-Shaw cell to wettability-altered micromodel." *Energy & Fuels* 36(2022): 5762-5774. (SCI journal, IF=4.654, JCR Q1) (Partially included in Chapter 2) <https://doi.org/10.1021/acs.energyfuels.2c00772>
- [3] **Y. She**, H. Aoki, Y. Hu, M. A. Mahardika, C. Zhang, M. Nashir, W. Wang\*, A. Patmonoaji, S. Matsushita, T. Suekane. "Effect of in-situ dual surfactant formulation on spontaneous oil deformation: A comprehensive study from mechanism discovery to oil recovery application." *Industrial & Engineering Chemistry Research* 61(2022): 11568-11578. (SCI journal, IF=4.326, JCR Q1) (Partially included in Chapter 2) <https://doi.org/10.1021/acs.iecr.2c01735>
- [4] **Y. She\***, M. A. Mahardika, Y. Hu, A. Patmonoaji, S. Matsushita, T. Suekane, Y. Nagatsu. "Three-dimensional visualization of the alkaline flooding process with in-situ emulsification for oil recovery in porous media." *Journal of Petroleum Science and Engineering* 202(2021): 108519. (SCI journal, IF=5.168, JCR Q1) (Fully included in Chapter 3) <https://doi.org/10.1016/j.petrol.2021.108519>
- [5] **Y. She**, W. Wang, Y. Hu, M. A. Mahardika, M. Nashir, C. Zhang\*, A. Patmonoaji, S. Matsushita, T. Suekane. "Pore-scale investigation on microemulsion-based quasi-miscible flooding for EOR in water-wet/oil-wet reservoirs: A study by X-ray microtomography." *Journal of Petroleum Science and Engineering* 216(2022): 110788. (SCI journal, IF=5.168, JCR Q1) (Fully included in Chapter 4) <https://doi.org/10.1016/j.petrol.2022.110788>
- [6] Y. Hu\*, **Y. She**, A. Patmonoaji, C. Zhang, T. Suekane. "Effect of capillary number on morphological characterizations of trapped gas bubbles: Study by using micro-tomography." *International Journal of Heat and Mass Transfer* 163(2020): 120508. (SCI journal, IF=5.431, JCR Q1) <https://doi.org/10.1016/j.ijheatmasstransfer.2020.120508>

- [7] M. A. Mahardika\*, **Y. She**, F. Shori, A. Patmonoaji, S. Matsushita, T. Suekane, Y. Nagatsu. "Enhanced heavy oil recovery by calcium hydroxide flooding with the production of viscoelastic materials: study with 3D X-ray tomography and 2D glass micromodels." *Energy & Fuels* 35(2021): 11210–11222. (**SCI journal**, IF=4.654, JCR Q1) <https://doi.org/10.1021/acs.energyfuels.1c00963>
- [8] C. Zhang\*, **Y. She**, Y. Hu, Z. Li, W. Wang, A. Patmonoaji, T. Suekane. "Experimental investigation of solute transport in variably saturated porous media using X-ray Computed Tomography." *Physics of Fluids* 33(2021): 076610. (**SCI journal**, IF=4.980, JCR Q1) <https://doi.org/10.1063/5.0056221>
- [9] M. A. Mahardika\*, **Y. She**, T. Koue, A. Patmonoaji, M. Nasir, S. Matsushita, T. Suekane. "Competition of gravity and viscous forces in vertical displacement in three-dimensional porous media." *Physics of fluids* 34(2022): 073102. (**SCI journal**, IF=4.980, JCR Q1) <https://doi.org/10.1063/5.0090387>
- [10] M. Nasir, R. Yamaguchi, **Y. She**, A.\* Patmonoaji, M. A. Mahardika, W Wang, Z. Li, S. Matsushita, T. Suekane. "Yogurt instability: Hydrodynamic fingering induced by gel film formation in miscible fluid system." *Applied sciences* 12(2022): 5043. (**SCI journal**, IF=2.838, JCR Q2) <https://doi.org/10.3390/app12105043>
- [11] Y. Hu, C. Zhang, A. Patmonoaji\*, **Y. She**, S. Matsushita, T. Suekane. "Pore-scale investigation of wettability impact on residual nonaqueous phase liquid dissolution in natural porous media." *Science of The Total Environment* 787(2021): 147406. (**SCI journal**, IF=10.753, JCR Q1) <https://doi.org/10.1016/j.scitotenv.2021.147406>
- [12] A.\* Patmonoaji, M. Nasir, M. A. Mahardika, **Y. She**, T. Suekane. "A unique dissolution behavior of trapped CO<sub>2</sub> into flowing water inside a porous medium compared with other gases." *Journal of the Mining and Materials Processing Institute of Japan* 137(2021): 9. <https://doi.org/10.2473/journalofmmij.137.91>
- [13] A. Patmonoaji\*, M. A. Mahardika, M. Nasir, **Y. She**, W Wang, M. A. Muflikhun, T. Suekane. "Stereolithography 3D printer for micromodel fabrications with comprehensive accuracy evaluation by using microtomography." *Geosciences* 12(2022): 183. (**SCI journal**, IF=2.076, JCR Q2) <https://doi.org/10.3390/geosciences12050183>
- [14] M. Nasir, K. Kaito, A.\* Patmonoaji, M. A. Mahardika, **Y. She**, S. Matsushita, T. Suekane. "Three-dimensional pore-scale observation of drying process of porous media." *International Journal of Heat and Mass Transfer* 196(2022): 123299. (**SCI journal**, IF=5.431, JCR Q1) <https://doi.org/10.1016/j.ijheatmasstransfer.2022.123299>

## 2. International conferences

- [1] **Y. She**, M. A. Mahardika, W. Wang, T. Suekane. "Pore-scale investigation of microemulsion flooding strategies on enhanced oil recovery in oil-wet reservoir by X-ray microtomography." The 32nd International Symposium on Transport Phenomena, Tianjin, China, March-2022. (**English oral**)